CHALMERS

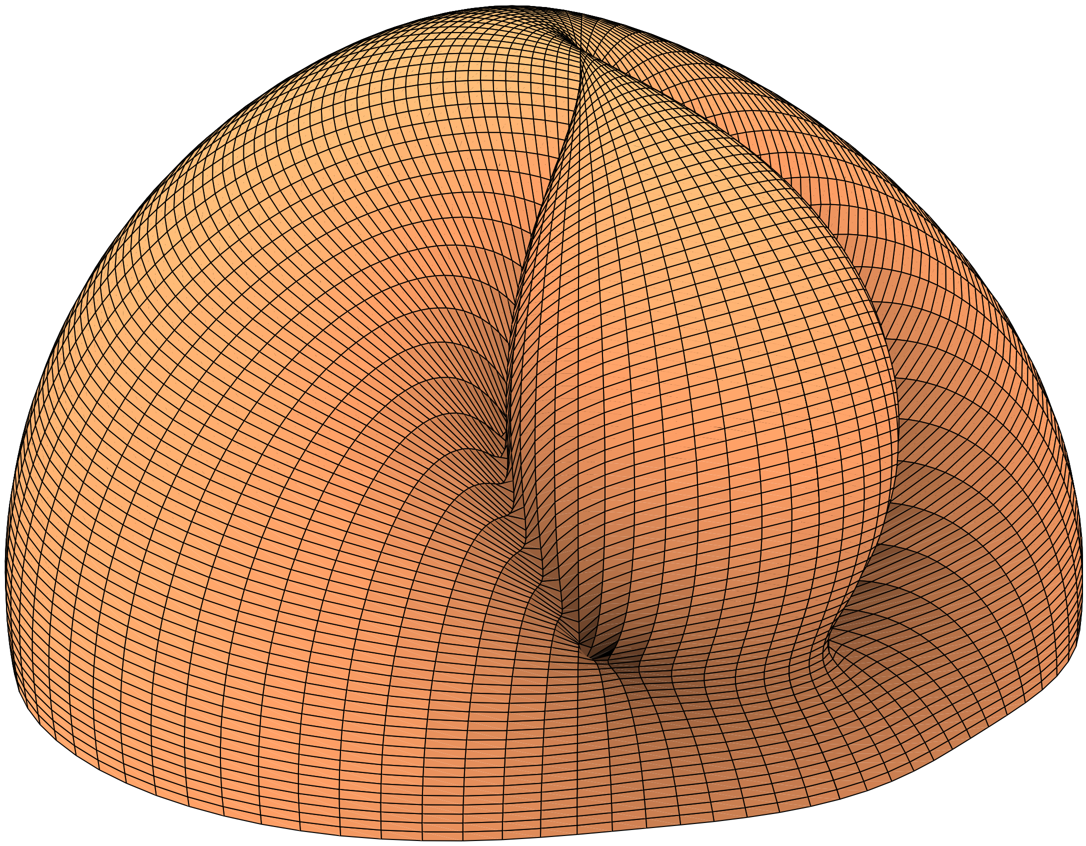

Electromagnetic Models of Bistatic Radar Scattering from Rough Surfaces with Gaussian Correlation Function

MACIEJ J. SOJA

Department of Radio and Space Science
Radar Remote Sensing Group
CHALMERS UNIVERSITY OF TECHNOLOGY
Göteborg, Sweden 2009

The figure on the first page shows angular scattering distribution simulated with Advanced Integral Equation Model for HH polarization mode. The incident angle is $\theta_i = 65^\circ$, the dielectric permittivity is $\epsilon_r = 16$, and the roughness parameters are $k\sigma = 0.1$ and $kL = 1.5$. Correlation function is Gaussian. Viewing azimuth angle is 53.5° measured counterclockwise from the negative y-axis. Viewing elevation angle is 22° measured from the x-y-plane and above it.

MASTER OF SCIENCE THESIS

Electromagnetic Models of Bistatic Radar Scattering from Rough Surfaces with Gaussian Correlation Function

MACIEJ J. SOJA

Supervisors:
Prof. Lars M. H. Ulander
Gustaf Sandberg
Dr. Leif Eriksson

November 2009

Department of Radio and Space Science
Radar Remote Sensing Group
CHALMERS UNIVERSITY OF TECHNOLOGY
Gothenburg, Sweden 2009

Electromagnetic Models of Bistatic Radar Scattering from
Rough Surfaces with Gaussian Correlation Function
MACIEJ J. SOJA

Department of Radio and Space Science
Radar Remote Sensing Group
Chalmers University of Technology
SE-412 96 Gothenburg
Sweden
Telephone + 46 (0) 31 772 10 00

Abstract

The main scope of this Master Thesis project was to simulate incoherent bistatic radar scattering from random rough surfaces using electromagnetic models. Three well-established models were implemented: Physical Optics (PO), Geometrical Optics (GO), and Small Perturbation Model (SPM). These models are asymptotic in frequency, and thus only valid in the extreme cases of either very high frequencies, as for GO/PO, or very low frequencies, as for SPM. The main focus of this thesis is on the Integral Equation Model (IEM), which is a more recently developed model and partially bridges the validity gap between GO/PO and SPM. The Integral Equation Model is built on the same basis as GO/PO, namely the tangential plane approximation, but it also includes a complementary term, which accounts for multiple scattering. In order to solve the underlying integral equations, a number of approximations was introduced during the derivation of IEM by the original authors. Some of these simplifications could later be removed, which resulted in the more recent derivatives of IEM (mainly Improved Integral Equation Model, IIEM, and Advanced Integral Equation Model, AIEM), giving much more complicated, but also more accurate expressions.

Five of the mentioned models (GO, PO, SPM, IEM, and AIEM) were implemented by the author and verified against results published in literature. In the low frequency region, studies of scattering coefficient (σ^0) as a function of the elevation angle θ_s were performed for a number of setups, and the agreement of the implemented models with the literature was perfect in all cases. In the high frequency region, σ^0 was studied both as a function of θ_s and the azimuth angle ϕ_s. The general behavior of σ^0 as a function of ϕ_s is such, that a dip (minimum of scattering) can be expected at an azimuth angle around $90°$. The observed positions of these dips were in a disagreement of up to $\pm 20°$ when compared to the literature. In the study of σ^0 as a function of θ_s, the agreement with the literature was good except for the cases that were directly affected by the previously described dip disagreement. However, even in those cases, the maximal difference in σ^0 compared to the literature was at most ± 2 dB. The influence of the dip disagreement on the further studies could be minimized by avoiding angular setups close to the problematic regions.

The models were used to study the angular distribution of the scattering coefficients for two surfaces: a gently undulating surface in the PO region and a rough surface in the SPM region. This study resulted in graphs that visualize scattering in an intuitive way, which improves the understanding of the governing processes. It was confirmed that the roughness parameters greatly affect the angular distribution of scattering, and that in the low-frequency region (SPM-region), scattering is more equally distributed in all directions than in the high-frequency region (GO/PO-region).

In a second study, scattering from surfaces with different roughness parameters for some fixed angular setups was investigated. It was found that the bistatic scattering coefficient for gently undulating surfaces (high kL) was maximized when the vertical variations were moderate in magnitude. In forward scattering, in the region with very gentle horizontal variations and small vertical variations, it was found that a slightly rough surface gives higher scattering coefficients than a perfectly smooth surface, which indicates that the presented versions of the models are not suitable for perfectly smooth surfaces unless the coherent component is added.

The results of the studies also show that the models generally work well when cross-compared with each other. However, AIEM overestimates backscattering from surfaces with very gentle horizontal variations and small vertical variations as compared to IEM and PO. Moreover, it also shows a disagreement with IEM and SPM for backscattering in the low-frequency region. Comparing the scattering coefficients for VV and HH modes, one can observe that they are higher for HH than for VV in all cases except backscattering in the low-frequency region where the result is the opposite.

Index Terms

bistatic radar scattering, random rough surfaces, integral equation model (IEM), advanced integral equation model (AIEM), geometrical optics model (GO), physical optics model (PO), small perturbation model (SPM)

CONTENTS

NOMENCLATURE

Here, the basic nomenclature is presented and it is valid throughout this report unless mentioned otherwise. In cases where $\mathbf{E}$ or $\mathcal{E}$ are involved, they can be replaced by $\mathbf{H}$ or $\mathcal{H}$ in order to get the corresponding symbols for magnetic fields.

α	tangential plane tilt angle
$\hat{\mathbf{d}}$	local coordinate system base vector ($\hat{\mathbf{d}} = \hat{\mathbf{k}}_i \times \hat{\mathbf{t}}$)
$\Delta\phi$	difference in azimuth angles between incident and scattered radiation ($\Delta\phi = \phi_s - \phi_i$)
ϵ_1 (ϵ_2)	dielectric permittivity in medium 1 (medium 2)
ϵ_r	relative dielectric permittivity on the interface ($\epsilon_r = \epsilon_2/\epsilon_1$)
E_0	amplitude of the incident electric field
E^i	amplitude of the incident electric field together with the phase term
ϕ_i (ϕ_s)	incident (scattered) azimuth angle
k_1 (k_2)	wave number in medium 1 (medium 2)
kL	normalized correlation length (unitless)
$k\sigma$	normalized standard deviation of a surface (unitless)
k_{ix}, k_{iy}, k_{iz}	components of $\hat{\mathbf{k}}_i$
k_{sx}, k_{sy}, k_{sz}	components of $\hat{\mathbf{k}}_s$
$\hat{\mathbf{k}}_i$ ($\hat{\mathbf{k}}_s$)	incident (scattered) wavevector
$\hat{\mathbf{h}}_i$ ($\hat{\mathbf{h}}_s$)	incident (scattered) horizontal polarization vector
$\mathcal{E}^i$ ($\mathcal{E}^t$)	incident (transmitted) complementary electric field coefficient
η_1 (η_2)	intrinsic impedance in medium 1 (medium 2)
L	correlation length in meters
μ_1 (μ_2)	magnetic permeability in medium 1 (medium 2)
μ_r	relative magnetic permeability on the interface ($\mu_r = \mu_2/\mu_1$)
$\hat{\mathbf{n}}_1$ or $\hat{\mathbf{n}}$	normal vector to the boundary in medium 1
$\hat{\mathbf{n}}_2$ or $-\hat{\mathbf{n}}$	normal vector to the boundary in medium 2
$\hat{\mathbf{n}} \times \mathbf{E}$	tangential electric surface field
$(\hat{\mathbf{n}} \times \mathbf{E})_k$	Kirchhoff term of a tangential surface field $\hat{\mathbf{n}} \times \mathbf{E}$
$(\hat{\mathbf{n}} \times \mathbf{E})_c$	complementary term of a tangential surface field $\hat{\mathbf{n}} \times \mathbf{E}$
$(\hat{\mathbf{n}} \times \mathbf{E}_h)_k$	Kirchhoff term of a tangential surface field $\hat{\mathbf{n}} \times \mathbf{E}$ (incident polarization horizontal)
$(\hat{\mathbf{n}} \times \mathbf{E}_v)_k$	Kirchhoff term of a tangential surface field $\hat{\mathbf{n}} \times \mathbf{E}$ (incident polarization vertical)
$(\hat{\mathbf{n}} \times \mathbf{E}_h)_c$	complementary term of a tangential surface field $\hat{\mathbf{n}} \times \mathbf{E}$ (incident polarization horizontal)
$(\hat{\mathbf{n}} \times \mathbf{E}_v)_c$	complementary term of a tangential surface field $\hat{\mathbf{n}} \times \mathbf{E}$ (incident polarization vertical)
ν	frequency of the incident wave
$\hat{\mathbf{p}}$	incident polarization vector
$\hat{\mathbf{q}}$	scattered polarization vector
R	Fresnel coefficient for cross-polarization
$R_\parallel$ ($R_\perp$)	Fresnel coefficient for parallel (perpendicular) polarization
$\rho(\xi)$	correlation function
σ	standard deviation of a surface in meters
σ_{RCS}	radar cross section in square meters
σ^0	normalized radar cross section, scattering coefficient
σ^0_{pq}	scattering coefficient for polarization mode pq (can be HH, VV, HV, or VH)
$\hat{\mathbf{t}}$	local coordinate system base vector ($\hat{\mathbf{t}} = \hat{\mathbf{k}}_i \times \hat{\mathbf{n}}/\lvert\hat{\mathbf{k}}_i \times \hat{\mathbf{n}}\rvert$)
θ_i (θ_s)	incident (scattered) altitude angle
ϑ	local incidence angle
$\hat{\mathbf{v}}_i$ ($\hat{\mathbf{v}}_s$)	incident (scattered) vertical polarization vector
$\mathbf{E}$	total electric field in the upper medium
$\mathbf{E}^i$ ($\mathbf{E}^s$, $\mathbf{E}^t$, $\mathbf{E}^r$)	incident (scattered, transmitted, reflected) electric field
$\mathbf{E}_\parallel$ ($\mathbf{E}_\perp$)	parallelly (perpendicularly) polarized part of the electric field
$\mathbf{E}_h$ ($\mathbf{E}_v$)	horizontally (vertically) polarized part of the electric field
χ_i	Green's function in the upper medium
χ_t	Green's function in the lower medium
ψ	grazing angle ($90^\circ - \theta_i$)
$Z(x, y)$	realization of a surface created by a random process
$Z_x(x, y)$	partial derivative of $Z(x, y)$ in the x-direction
$Z_y(x, y)$	partial derivative of $Z(x, y)$ in the y-direction

1 INTRODUCTION

DECADES have passed since the radar technique was invented, and the field of use of radar has expanded greatly. Nowadays, radar monitoring of ice, sea, agricultural soil, and forests is of great importance both for environmental studies and more practical purposes such as sea-state monitoring and wind speed measuring. These kinds of studies have been done at the Remote Radar Sensing group at Chalmers University of Technology in Gothenburg, Sweden for over 20 years giving the group a vast experience in the field of radar data analysis. In order to improve the general knowledge about the mechanisms of scattering, as well as to improve the produced algorithms, theoretical studies of scattering from rough surfaces are very important.

Rough surface scattering can be studied numerically or analytically, depending on the knowledge about a surface and the purpose of the study. If a particular surface is known (deterministic), then numerical studies using Maxwell's equations can be performed with good results. General studies of random rough surfaces can also be done numerically after averaging over a wide set of statistically representative deterministic surfaces. However, this can be a very slow process since numerical simulations often are computationally demanding.

If a surface is relatively homogenous in its structure or consists of cells that are relatively homogenous, then it can be described by a few statistical parameters such as standard deviation of height variations, correlation length, and correlation function. Many natural surfaces, such as ice and agricultural soil, can be described in such a way. In that case, theoretical studies of scattering from these kinds of random rough surfaces can be performed much more efficiently using models based on statistics.

For many years, researchers were restricted to two general models that worked for different types of rough surfaces — Kirchhoff Model (KM) based on the high-frequency approximation for slowly undulating surfaces [1–7], and Small Perturbation Model (SPM) based on the low-frequency approximation for small vertical variations [2–7]. Both models are asymptotic and studies outside the mentioned validity regions are thus highly restricted.

During the eighties, a model valid for surfaces with intermediate roughness was developed for perfectly conducting surfaces [8], but it was first in 1992 that Fung et al. revealed a model that also worked for dielectric surfaces [9]. This model was called Integral Equation Model (IEM) as it was built on integral equations for electric and magnetic fields as described by Poggio and Miller [10]. IEM was later further developed in order to make the simulated scattering more accurate which resulted in models such as Improved IEM [11] and Advanced IEM [12–14].

After the mentioned models were implemented, simulation results were verified against results found in reference articles (mainly Wu et al. [14]) for identical setups of the input parameters. Thereafter, IEM and AIEM were used together with the asymptotic models in a study of scattering from a wide range of different random rough surfaces. Also, some qualitative studies of the models in scenarios that have not been previously examined in literature (at least to the author's current knowledge) have been made. These studies include an examination of the angular behavior of the scattered field in a half-sphere above the surface, as well as a qualitative study of the scattering coefficients as a function of surface roughness parameters. Some of the results can easily be explained using the same arguments as for the asymptotic models while some other results are more difficult to understand intuitively. Even though no empirical data was used in this study, the results showed that the implemented models produce consistent results within their validity regions. No major disagreements were found as compared to references.

This report has the following structure. First, radar theory and some basic concepts crucial for further understanding are presented in Section 2. Next, some physical mechanisms of scattering are briefly explained (Section 3). In Section 4, rough surfaces are described by means of statistics. Section 5 deals with the asymptotic models based on the Kirchhoff approximation and small perturbation theory. Thereafter, the derivation of the Integral Equation Model is presented in detail (Section 6). In Section 7, some major assumptions and approximations used in the derivation of IEM are explained and examined, and the later versions of IEM are presented. Section 8 deals with the verification of the implemented models against some known results and against each other for chosen values of surface parameters, while Section 9 contains a study of the scattering for different surfaces. Finally, in Section 10 the results are summarized, analyzed, and discussed.

All simulations in this report were performed in Matlab®. All figures in this report (except graphs to the left in Figures 8.1-8.2, which have been taken from Fung et al. [11]) have been produced by the author using either XFig or Matlab®. This report was written in LaTeX using a slightly modified version of the IEEE template[1].

1. http://www.ieee.org/web/publications/authors/transjnl/index.html

2 RADAR

2.1 History and Basic Principles

The word *radar* is an abbreviation for *radio detection and ranging* [15–17] and was originally introduced by the US Navy in the early forties. The technology itself has many fathers and can be tracked back to the beginning of the 20th century. The first radar units were only designed for detecting ships on sea, but as the technology developed, its area of use broadened. Nowadays, radar is used in a very wide range of different applications, including such non-military areas as meteorology, oceanology, and traffic control.

Radar is an active remote sensing system based on the principle of *echolocation*. Some animals (like bats, whales, and some birds) spend most of their lives in environments, where optical sensing is impossible (like in darkness). These animals developed echolocation, a system based on measuring the echo of a transmitted signal. When a probing sound is emitted by the animal, it propagates into the environment until it hits an obstacle and is scattered. Some parts of the signal return to the animal, where they are detected, measured, and analyzed. From that, the animal gets an acoustic image of the surroundings, an image it uses for orientation. Humans are generally neither equipped nor trained for the use of echolocation although there are some cases when people can actually make use of if (like people with seeing disorder, who use a stick to generate sounds that help them perceive the environment). Echolocation is reproduced by modern technology in different forms of remote sensing devices. These devices can either use sound waves, like in sonar, optical waves, like in lidar, or microwaves, like in radar.

2.2 Frequencies and Radar Bands

TABLE 2.1: An overview for the most common radar bands according to Skolnik [18] and AIAA [19]. The P-band is an old name for frequencies around 300 MHz (P stands for *previous*).

Band:	Frequency interval:	Wavelength interval:	Usage:
HF	3-30 MHz	10-100 m	Over-the-horizon radars (*High Frequency*)
VHF	30-300 MHz	1-10 m	Very long-range surveillance (*Very High Frequency*)
UHF	300-1000 MHz	30-100 cm	Very long-range surveillance (*Ultra High Frequency*)
L	1-2 GHz	15-30 cm	Long-range surveillance, enroute traffic control (*long* wavelengths)
S	2-4 GHz	7.5-15.0 cm	Moderate-range surveillance, terminal traffic control, long-range weather (*short* wavelengths)
C	4-8 GHz	3.75-7.50 cm	Long-range tracking, airborne weather (a *compromise* between X and S)
X	8-12 GHz	2.50-3.75 cm	Short-range tracking, missile guidance, mapping, marine radar, airborne intercept (called X for historical reasons, secret band during World War II)
K_u	12-18 GHz	1.67-2.50 cm	High resolution mapping, satellite altimetry (subscript u for *under* K)
K	18-27 GHz	1.11-1.67 cm	Meteorology, automotive radar (*kurz*, short in German)
K_a	27-40 GHz	0.75-1.11 cm	Very high resolution mapping, airport surveillance (subscript a for *above* K)
V	40-75 GHz	4.0-7.5 mm	Experimental
W	75-110 GHz	2.7-4.0 mm	
mm	110-300 GHz	1.0-2.7 mm	

Radar uses electromagnetic radiation with frequencies corresponding to radio waves or microwaves, and the choice of frequency is important as various applications demand different kinds of properties. Generally one can say that higher frequencies give smaller antennas, higher bandwidth (thus higher resolution), but also greater sensitivity to atmospherical noise which generally causes a shorter range. Higher frequencies also demand more precise technology. The lower limit at around 3MHz is set by the fact, that big antennas are needed in order to get a narrow bandwidth [18]. The interval has been divided in many frequency bands called by quite randomly chosen letters (mainly in order to confuse the enemies during World War II). Each band usually has special properties that make it suitable for a certain application. For example, in the K-band (18-27GHz), water vapor is almost opaque for electromagnetic waves which makes it suitable for cloud detection, but totally useless for aircraft detection. A overview of the different bands can be seen in Table 2.1.

2.3 Radar Equation

The *radar equation* is a relation which is often considered to be the fundamental equation of radar. Knowing radiation power of an antenna and some variables that can be measured, the power measured at a receiving antenna can be computed. The derivation follows closely the ones that can be found in Kingsley and Quegan [15], Sullivan [16], Woodhouse [17], and Skolnik [18]. An illustration explaining the different symbols used below can be found in Figure 2.1

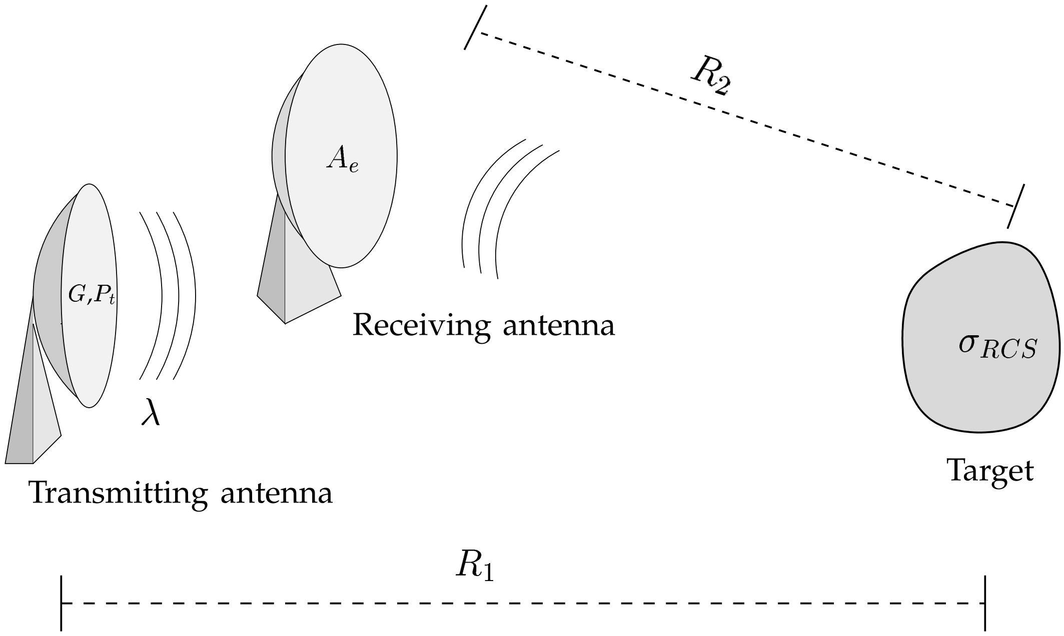

Fig. 2.1: A typical bistatic radar system consists of a transmitting and a receiving antenna. An electromagnetic wave is emitted from the transmitter into the space towards an object. As the wave encounters the target, it is scattered and some of the wave is reflected and then received at the second antenna.

Assuming that a transmitting antenna has a peak power output P_t and that it has a gain G_t in the transmitting direction, the power flux at the distance R_1 in that direction is:

$$I = \frac{P_t G_t}{4\pi R_1^2}.$$

Radar cross section (σ_{RCS}[2] or RCS as it may be referred to) is a parameter that describes the scattering strength sensed by radar. If the target is situated at the distance R_1 from the radar antenna, the scattered flux density at the distance R_2 is:

$$I' = \frac{I\sigma_{RCS}}{4\pi R_2^2} = \frac{P_t G_t \sigma_{RCS}}{(4\pi)^2 R_1^2 R_2^2}.$$

Assuming that the receiving antenna has an effective area of A_e, the received power at the antenna is:

$$P_r = I' A_e = \frac{P_t G_t \sigma_{RCS} A_e}{(4\pi)^2 R_1^2 R_2^2}. \tag{2.1}$$

If a radar uses the same antenna for both transmission and reception then it is called *monostatic system*. Using monostatic radar system, only backward scattering can be measured. If the receiver is situated somewhere else than the transmitter, then the system is called *bistatic system*. In the case of a monostatic radar system, the gain is the same for both transmission and reception ($G = G_t = G_r$) and also, $R_1 = R_2 = R$. The quantity A_e can be re-written as [16]:

$$A_e = \frac{G\lambda^2}{4\pi} \tag{2.2}$$

and (2.1) turns into:

$$P_r = \frac{P_t G^2 \lambda^2 \sigma_{RCS}}{(4\pi)^3 R^4} \tag{2.3}$$

where λ is the wavelength of the used wave. This is one of the most common forms of the radar equation.

In the bistatic case, (2.3) becomes:

$$P_r = \frac{P_t G_t G_r \lambda^2 \sigma_{RCS}}{(4\pi)^3 R_1^2 R_2^2}. \tag{2.4}$$

2. Radar cross section is normally denoted by just σ but in order to avoid confusion with standard deviation σ, RCS will be referred to as σ_{RCS}.

Sullivan [16, Chap. 1] describes another form of the radar equation — namely the one that employs the *signal-to-noise* ratio (SNR) after matched filtering:

$$SNR = \frac{E_r}{E_n}, \tag{2.5}$$

where E_r is the received and processed signal energy and E_n is the noise spectral density. For a pulsed radar with pulse length τ and a loss factor L, the received signal energy is

$$E_r = \frac{P_r \tau}{L C_B}, \tag{2.6}$$

where C_B is a correction factor due to signal processing (equal to 1 for matched filtering), and the noise energy can be expressed as

$$E_n = k_B T_s, \tag{2.7}$$

where k_B is Boltzmann's constant and T_s is the system temperature. Expressions (2.6) and (2.7) can be inserted into (2.5) and together with (2.3) and (2.2) they give:

$$SNR = \frac{P_t A_e^2 \sigma_{RCS} \tau}{4\pi R^4 \lambda^2 k_B T_s C_B L}. \tag{2.8}$$

All the calculations above are carried out for a fixed direction of the incident and reflected waves (fixed positions of both antennas and the object). It should be mentioned that quantities such as $G_{t,r}$ and σ_{RCS} are generally different for different angles (anisotropic). One should thus express them as:

$$\begin{aligned} G_t &= G_t(\hat{\mathbf{k}}_i), \\ G_r &= G_r(\hat{\mathbf{k}}_s), \\ \sigma_{RCS} &= \sigma_{RCS}(\hat{\mathbf{k}}_i, \hat{\mathbf{k}}_s), \end{aligned}$$

where $\hat{\mathbf{k}}_i$ and $\hat{\mathbf{k}}_s$ are unit vectors in the direction of the incident and scattered wave (see Figure 2.2b), respectively. For monostatic radar, $\hat{\mathbf{k}}_s = -\hat{\mathbf{k}}_i$ and thus $\sigma_{RCS} = \sigma_{RCS}(\hat{\mathbf{k}}_i)$.

2.4 Normalized Radar Cross Section and the Scattering Coefficient

An expression for the monostatic radar cross section can be easily derived from (2.3) which gives:

$$\sigma_{RCS} = \frac{P_r (4\pi)^3 R^4}{P_t G^2 \lambda^2}. \tag{2.9}$$

In the bistatic case this should be instead taken from (2.4):

$$\sigma_{RCS} = \frac{P_r (4\pi)^3 R_1^2 R_2^2}{P_t G_t G_r \lambda^2}, \tag{2.10}$$

where the transmitting and receiving antennas have gain G_t and G_r, respectively.

In applications where extended targets are studied (as opposed to point targets), one is generally more interested in the *normalized radar cross section* σ^0, which is the expression for σ_{RCS} divided by the area A over which the measurement is made. This yields:

$$\sigma^0 = \frac{\sigma_{RCS}}{A}.$$

The normalized radar cross section σ^0, or the scattering coefficient as it also can be called, is often measured in decibels:

$$\sigma^0_{dB} = 10 \cdot \log_{10} \sigma^0,$$

which is the main quantity studied in this report.

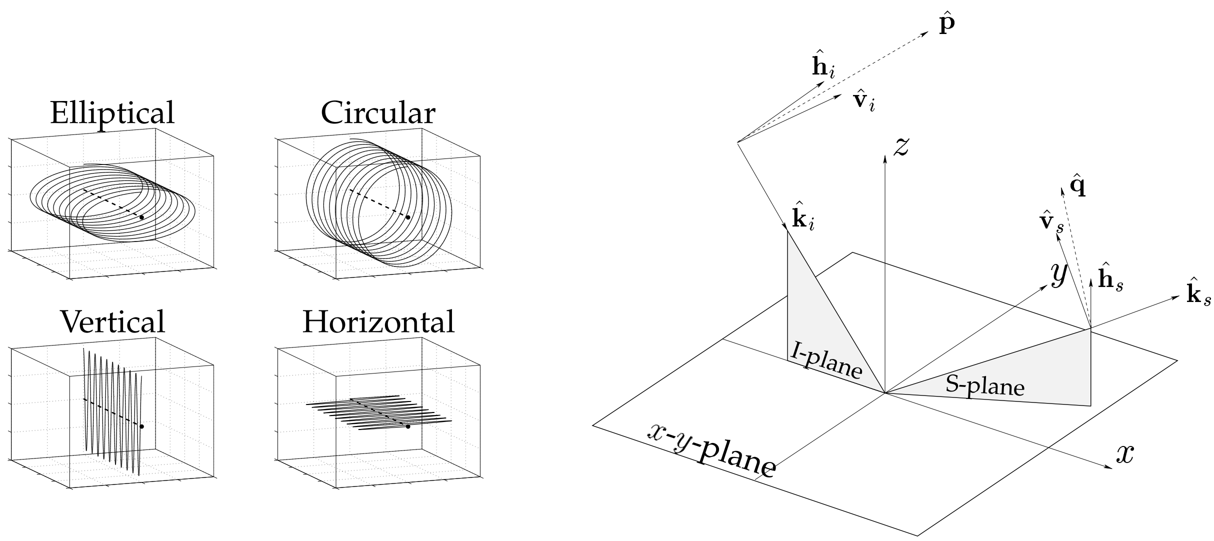

(a) Polarization types (b) 3D geometry

Fig. 2.2: (a) Different types of polarization. The solid line marks the trajectory of the tip of the field vector while the dashed line indicates the direction of propagation of the wave. (b) The incident polarization vector $\hat{\mathbf{p}}$ can always be re-written as a sum of the two base vectors $\hat{\mathbf{v}}_i$ and $\hat{\mathbf{h}}_i$ (similar for the scattered polarization vector $\hat{\mathbf{p}}$ with $\hat{\mathbf{v}}_s$ and $\hat{\mathbf{h}}_s$). Vector $\hat{\mathbf{v}}_i$ is perpendicular to $\hat{\mathbf{k}}_i$ and lies in the incident (I) plane while $\hat{\mathbf{h}}_i$ is parallel to the y-axis. Vector $\hat{\mathbf{v}}_s$ is perpendicular to $\hat{\mathbf{k}}_s$ and lies in the scattered (S) plane while $\hat{\mathbf{h}}_s$ is perpendicular to $\hat{\mathbf{k}}_s$ and parallel to the x-y-plane.

2.5 Plane Waves, Polarization and Coordinate Systems

Incident waves can be assumed plane if the distance between the examined object and the antenna is large. In radar applications, this assumption (called *far field approximation*) is most often valid and widely used. The following paragraphs use the fact, that the incident radiation consists of plane waves.

The property of wave *polarization* describes the direction of wave oscillations. Electromagnetic plane waves propagate in a homogenous and isotropic medium as transverse waves that oscillate in a plane perpendicular to the direction of propagation. Looking at the plane of oscillations and keeping it fixed in space, the tip of the field vector can either move along a straight line (linear polarization), along an ellipse (elliptical polarization), or along a circle (circular polarization), which is a special case of elliptical polarization. Elliptical polarization can be either right- or left-handed depending on the direction of the rotation. In Figure 2.2a, four different types of polarization are shown.

Since circularly and elliptically polarized waves can be resolved into two perpendicular linearly polarized waves with a phase shift of $\pi/2$ radians, it is only necessary to study linear polarizations in two linearly independent directions in order to be able to cover all possible polarizations. The vector that describes polarization of the incident electric field will be called $\hat{\mathbf{p}}$. Since Maxwell's equations are linear, electric and magnetic fields can be split into additive parts that can be manipulated separately. This way, each vector $\hat{\mathbf{p}}$ can be resolved into a linear combination of the two orthonormal vectors $\hat{\mathbf{h}}_i$ and $\hat{\mathbf{v}}_i$ representing horizontal and vertical polarization (see Figure 2.2b). This way, a study of only two polarization directions is sufficient.

In studies of scattering, the transmitter and the receiver work with either horizontal or vertical polarizations. Thus, there is a total of four modes available when studying scattering — vertical-vertical (VV), horizontal-horizontal (HH), horizontal-vertical (HV), and vertical-horizontal (VH), see Table 2.2. Studying different scattering modes is very useful due to the diversity of ways in which waves and surfaces can interact.

TABLE 2.2: Four modes for scattering studies. The incident polarization vectors have subscript i and the scattered polarization vectors have subscript s. VV and HH are co-polarized (like-polarized) modes while HV and VH are cross-polarized modes.

	$\hat{\mathbf{q}} = \hat{\mathbf{v}}_s$	$\hat{\mathbf{q}} = \hat{\mathbf{h}}_s$
$\hat{\mathbf{p}} = \hat{\mathbf{v}}_i$	VV	VH
$\hat{\mathbf{p}} = \hat{\mathbf{h}}_i$	HV	HH

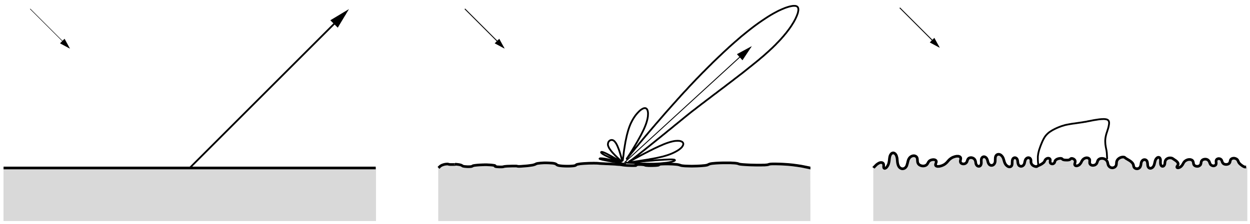

(a) Perfectly smooth surface (b) Slightly rough surface (c) Rough surface

Fig. 3.1: (a) Scattering from a perfectly smooth surface occurs in a coherent way and all radiation is reflected in the specular direction and the reflected field is also coherent. (b) When the surface is slightly rough, the major part of the radiation is still reflected in the coherent way in the specular direction, but some of the incident field is scattered incoherently in other directions. (c) Scattering from a very rough surface occurs mostly in the incoherent way and the coherent component is small (in the special case of a perfect diffuser, a perfect Lambertian surface, the coherent component is non-existent). See also Ogilvy [2] and Ulaby et al. [4, chap. 11].

3 Physics of Scattering

3.1 Surface and Volume Scattering

Scattering occurs on boundaries between two homogenous media with different electric and magnetic properties. If both media are semi-infinite and the boundary is the only discontinuity, then scattering only occurs at the boundary (*surface scattering*). Depending on the roughness of the surface, the angular distribution of the scattered and transmitted wave is different. If the lower medium is inhomogeneous or a mixture of different media, then an incoming wave is scattered on different levels and in different ways which is called *volume scattering*. Volume scattering (described briefly in Ulaby et al. [4, chap. 11]) is not dealt with in this report because it generally does not occur in the relevant surfaces.

3.2 Coherent and Incoherent Scattering

One can study scattering qualitatively by regarding two extreme cases — perfectly smooth surface and perfectly rough surface. Scattering from a perfectly smooth surface occurs in the same way as reflection from a mirror — the incoming wave is reflected in the specular direction. This kind of scattering affects the phase in a well known and predictable way and is called *coherent scattering*. Scattering from a Lambertian surface (a perfect diffuser) occurs in a perfectly *incoherent* way. All phase information is lost and the scattered field is evenly distributed over half-space (it is isotropic). See Figure 3.1, Ulaby et al. [4, chap. 11-2], and Beckmann and Spizzichino [1, chap. 5.3].

Scattering from a natural surface is a combination of coherent and diffuse components. For very rough surfaces, the diffuse component dominates. However, as a surface becomes smoother, the coherent component becomes more prominent. It is important to notice, that the roughness of the surface depends on the microwave frequency used. A surface that appears very rough in optical wavelengths may be smooth to microwaves. That is why roughness of surfaces is most often expressed in wavelength units (more about that in Section 4.3).

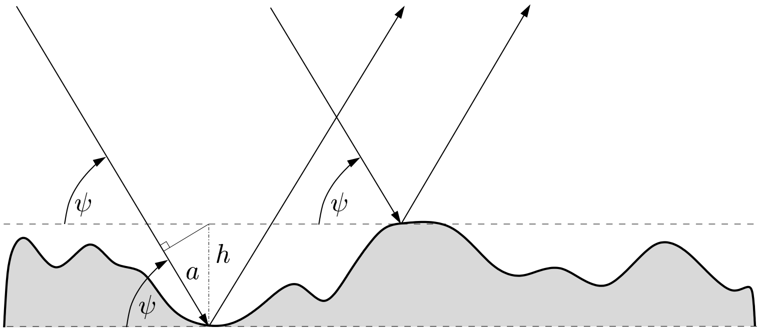

Fig. 4.1: In the derivation of the Rayleigh criterion, the path difference for the two different rays is computed from the grazing angle ψ and height difference h. The corresponding phase difference should be small in order to limit the incoherent component of the reflected field.

4 Randomly Rough Surfaces

In this text, scattering from randomly rough surfaces is studied from a statistical point of view. A surface is described by only a few parameters and no deterministic surfaces are studied. Compared to numerical methods for studies of particular surfaces (such as MM, method of moments, see Wu et al. [20, and references therein] for some comparisons), this approach gives much shorter computational time, more general results, and it can be used in many more fields. In order to use a statistical approach, a surface has to be described by a few parameters that will be described below. First, however, a criterion for a smooth surface is presented. The derivation of the so-called Rayleigh criterion follows closely Beckmann and Spizzichino [1], Ulaby et al. [4], Skolnik [18], Ishimaru [21].

4.1 Smooth Surfaces and the Rayleigh Criterion

In order to be able to talk about rough surfaces, it is needed to find a criterion, which determines whether the examined surface is rough or smooth. If two rays are incident on the surface with height deviation h at a grazing angle ψ (see Figure 4.1), then the ray that is reflected by the lower part of the surface travels an extra distance that can be computed with simple trigonometry:

$$\Delta r = 2a = 2h \sin\psi$$

and the corresponding phase difference is:

$$\Delta\varphi = k\Delta r = \frac{4\pi h \sin\psi}{\lambda}. \tag{4.1}$$

A phase shift of π will make the two rays interfere in such a way that they eliminate each other. By setting an arbitrary limit less than π, for example $\pi/2$, equation (4.1) turns into

$$\Delta\varphi = \frac{4\pi h \sin\psi}{\lambda} < \pi/2 \tag{4.2}$$

and the *Rayleigh criterion* for a smooth surface is:

$$h < \frac{\lambda}{8\sin\psi}. \tag{4.3}$$

Sometimes more strict limits are used instead of $\pi/2$, such as $\pi/4$ and $\pi/8$ and the factor 8 in (4.3) is replaced by 16 or 32. The factor 32 gives the strongest restriction and then the Rayleigh criterion turns into the so called *Fraunhofer criterion*, see Ulaby et al. [4, chap. 11]:

$$h < \frac{\lambda}{32\sin\psi}. \tag{4.4}$$

4.2 Statistical Description of Rough Surfaces

Natural surfaces such as terrain or sea can best be described by means of statistics [1, p. 72]. If a random process that generates a set of random variables $Z(x, y)$ has constant *mean value* equal to μ and constant *standard deviation* equal to σ, the *probability distribution* is constant in space, and its *correlation function*

$$\rho(x', y') \equiv \text{corr}[Z(x, y), Z(x + x', y + y')], \tag{4.5}$$

is independent of the space variables x, y, then it is stationary. The generated surface $Z(x, y)$ is then a representation of the process. In the following text, a random rough surface will be referred to as $Z(x, y)$ which does not mean a particular surface but only a representation of a stationary random process. In this report, only Gaussian stationary random processes are dealt with (Z has Gaussian probability density function).

4.2.1 Correlation Length

The correlation length L is defined for one-dimensional correlation function as [4, chap. 11]:

$$\rho(L) = \frac{1}{\mathrm{e}} \tag{4.6}$$

and it describes the typical minimal distance between two points, which can be assumed uncorrelated. For two-dimensional surfaces that have the same properties in both x- and y-directions, the correlation function can be written as a function of the radial distance:

$$\rho(\xi) = \rho(\sqrt{x'^2 + y'^2}), \tag{4.7}$$

and L is now the radial distance to the closest point where the correlation function is $\frac{1}{\mathrm{e}}$.

In Figure 4.2 three surfaces with constant σ but different L are plotted. Often, one could think that a high value of σ creates a rough surface and vice versa. As it can be seen, neither of the two parameters is on its own sufficient to describe whether a surface is smooth or rough. A surface with very high σ can be locally smooth if the correlation length L is high, as in Figure 4.2a. On the other hand, if a surface has short correlation length, even a small magnitude of σ will create a locally very rough surface. As a conclusion, one can say that L describes the surface variation in x-y-direction while σ describes the variation of the elevation of the surface. See also Beckmann and Spizzichino [1, chap. 5.3] and Ogilvy [2].

4.2.2 Some Common Correlation Functions

Two correlation functions are commonly used: Gaussian and exponential. Using a well defined correlation function, expectation values that show up in the derivations of the models (presented in the following sections) can be computed explicitly, which gives easier expressions. Here follows a short description of these functions as presented in Fung [22, app. 2B] for the one-dimensional case.

The *Gaussian (normal) correlation function* has an expression with only one parameter L:

$$\rho_G(\xi) = \exp\left(-\frac{\xi^2}{L^2}\right) \tag{4.8}$$

and its nth power Fourier transform is:

$$W_G^{(n)}(K) = \int_0^{\infty} \rho^n(\xi) J_0(K\xi)\xi \mathrm{d}\xi = \frac{L^2}{2n} \exp\left[-\left(\frac{KL}{2}\right)^2\right] \tag{4.9}$$

The *exponential correlation function* has the following expression:

$$\rho_{E0}(\xi) = \exp\left(-\frac{|\xi|}{L}\right). \tag{4.10}$$

This function is obviously not differentiable in the origin, which is an undesired property. Most often, the exponential function is replaced with a similar function that is differentiable in the origin. One such function is:

$$\rho_{E1}(\xi) = \exp\left[-\frac{|\xi|}{L} + \frac{|\xi|}{L} \exp\left(-\frac{|\xi|}{d}\right)\right]. \tag{4.11}$$

Close to the origin, $\rho_{E1} \approx \rho_{E0}$ but it is still differentiable. Other well-defined or generalized functions may be used as well. Exponential correlation functions are often used in practice since they in many cases represent the natural behavior of surfaces in a very realistic way. There are some other versions of this function presented in Fung [22, app. 2B] that will be omitted here.

The nth power roughness (Fourier) spectrum of the exponential correlation function (4.10) is:

$$W_E^{(n)}(K) = \left(\frac{L}{n}\right)^2 \left[1 + \left(\frac{KL}{n}\right)^2\right]^{-3/2}. \tag{4.12}$$

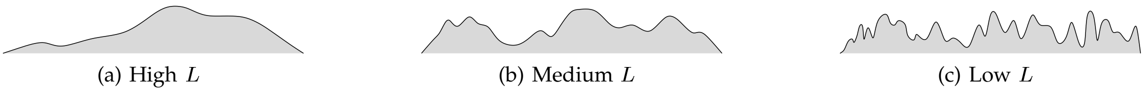

Fig. 4.2: The correlation length L describes how fast the surface changes in the x-y-direction. All three surfaces have the same standard deviation σ.

4.3 Normalized Roughness Parameters

Since surface parameters σ and L need always to be considered in relation to the frequency ν of the used wave, it is common to use their normalized values, which are found by a multiplication with the wave number k:

$$\text{Normalized correlation length:} \quad kL = \frac{2\pi\nu L}{c} = \frac{2\pi L}{\lambda}, \tag{4.13}$$

$$\text{Normalized standard deviation:} \quad k\sigma = \frac{2\pi\nu\sigma}{c} = \frac{2\pi\sigma}{\lambda}. \tag{4.14}$$

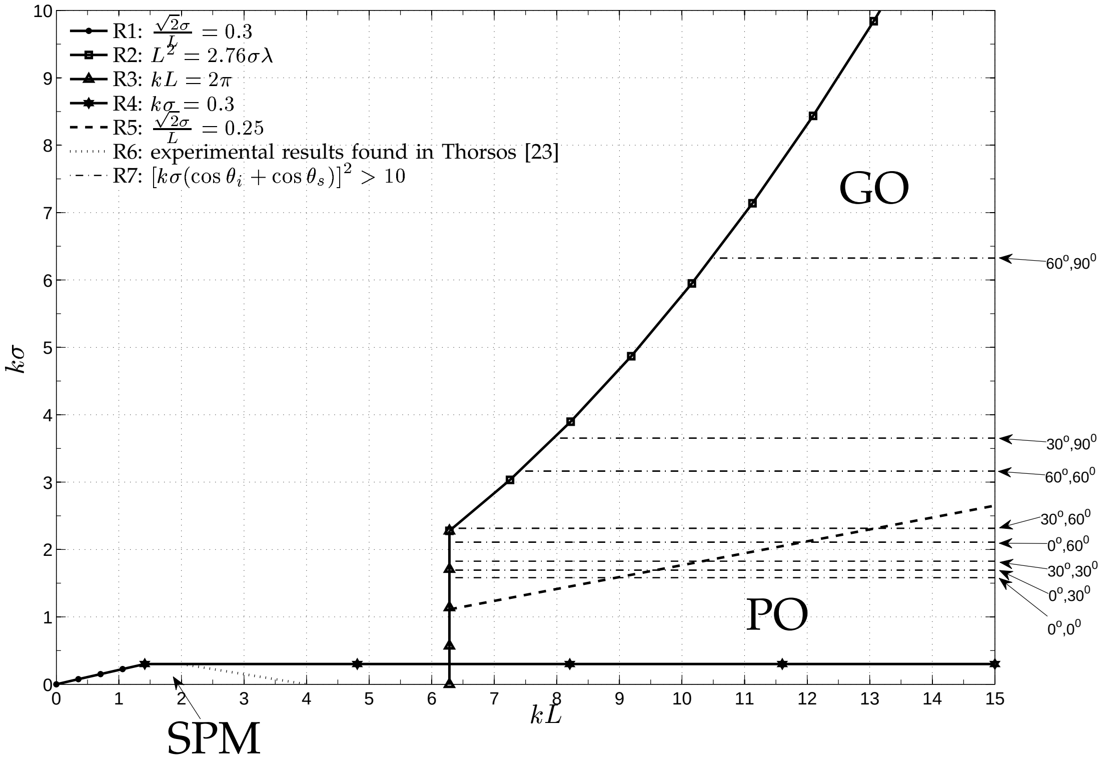

Fig. 5.1: Approximate validity regions for Small Perturbation Model (SPM), Geometrical Optics (GO), and Physical Optics (PO) according to Ulaby et al. [4], Koudogbo et al. [24], and Rees [25]. Validity for GO is limited by rules R2, R3 and/or R7. Rule R7 is a function of the two angles θ_i, θ_s and lines for some combinations of these angles are drawn in the figure. PO is limited by R3 and R5. SPM is limited by R1 and R4. In Thorsos [23] some extra limitations for SPM have been presented. These limitations restrict the use of SPM for $k\sigma > 2$, which is on the right hand side of the dashed line called R6. According to the work described in Thorsos [23], SPM can not be used for those kL-$k\sigma$-combinations due to a disagreement with numerical Monte Carlo simulations presented in that article. It is very important to notice that validity regions presented above are very rough and should be considered as guidelines rather than rules.

5 Basic models for Electromagnetic Simulation of Scattering

There are two well-established methods for electromagnetic simulation of radar scattering from randomly rough surfaces — the Kirchhoff Method (KM) based on the high-frequency assumption and *tangential plane approximation*, and the Small Perturbation Method (SPM) based on Taylor expansion around small values of $k\sigma$ (low frequencies). These two methods have different validity regions that for most cases do not overlap (see Figure 5.1). Roughly, one can say that SPM can be used when surfaces with small height variations and moderate correlation lengths are studied, while KM can be used for surfaces that can be assumed locally smooth.

5.1 Kirchhoff Model

The Kirchhoff Model is based on the assumption that the wavelength of the incident wave is much shorter than the horizontal variations of the surface, and that the so called radius of curvature (the ratio $\frac{l^2}{2.76\sigma}$, see [4, p. 1012-1013]) is sufficiently large so that the surface undulates gently and it can be seen as locally smooth (see Figure 5.1). This makes it possible to consider scattering of the incident wave as if it happened from an infinite tangent plane. This way, the problem can be regarded as a plane-boundary reflection problem, which simplifies both the mathematics and physics of the task.

5.1.1 Tangential Plane Approximation

The derivation of the Kirchhoff Model described in Ulaby et al. [4, chap. 12-4] originates in the so-called Stratton-Chu integral:

$$\mathbf{E}^s = K\hat{\mathbf{k}}_s \times \int \left[\hat{\mathbf{n}}_1 \times \mathbf{E} - \eta_1 \hat{\mathbf{k}}_s \times (\hat{\mathbf{n}}_1 \times \mathbf{H})\right] \mathrm{e}^{j\mathbf{r}\cdot\mathbf{k}_s} \mathrm{d}S, \tag{5.1}$$

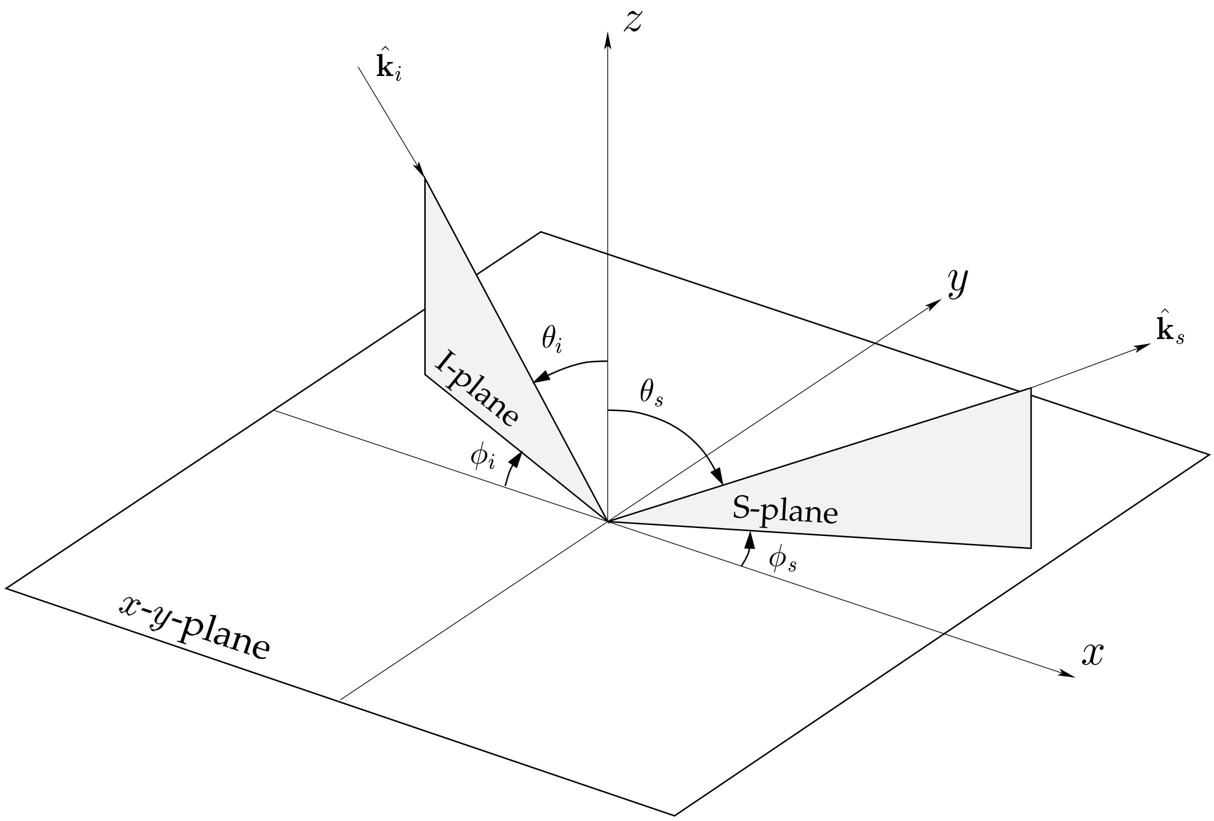

Fig. 5.2: The geometry and nomenclature used in the whole Section 5 are presented above. For IEM derivation, the nomenclature is the same except that ϕ_i is set to zero for simpler expressions.

where

$$K = -\frac{jk_1 \mathrm{e}^{-jk_1 R}}{4\pi R},$$

R is the distance from the center of the illuminated area to the point of observation, $\hat{\mathbf{n}}_1$ is the normal to the surface in medium 1, $\mathbf{E}^s$ is the scattered electric field, $\mathbf{E}$ and $\mathbf{H}$ are the total electric and magnetic fields in medium 1, and $\mathbf{k}_s = k_1 \hat{\mathbf{k}}_s$ is the scattered wave vector in medium 1 (see Figure 5.2). Expression (5.1) states that the scattered field at any point within S and in the upper medium can be expressed in terms of tangential surface fields, provided that S is closed and source free (the derivation of this integral is provided in Appendix B). Using the incident field expression:

$$\mathbf{E}^i = \hat{\mathbf{p}} E_0 \mathrm{e}^{-jk_1 \hat{\mathbf{k}}_i \cdot \mathbf{r}}, \tag{5.2}$$

where $\hat{\mathbf{p}}$ is a unit polarization vector and $k_1 \hat{\mathbf{k}}_i$ is the incident wave vector in medium 1, both incident and reflected fields can be re-written as sums of corresponding horizontally and vertically polarized components in the following way:

$$\mathbf{E}^i = \mathbf{E}^i_{\parallel} + \mathbf{E}^i_{\perp} \tag{5.3}$$

(similar for $\mathbf{E}^r$ and both $\mathbf{H}$-fields). Using the *tangential plane approximation* discussed above, the total field in medium 1 is a sum of the incident and reflected fields just above the boundary ($\mathbf{E}^i$ and $\mathbf{E}^r$, respectively), and the perpendicularly polarized electric tangential surface field can be written as:

$$\hat{\mathbf{n}}_1 \times \mathbf{E}_{\perp} = \hat{\mathbf{n}}_1 \times (\mathbf{E}^i_{\perp} + \mathbf{E}^r_{\perp}) = \hat{\mathbf{n}}_1 \times \mathbf{E}^i_{\perp}(1 + R_{\perp}) \tag{5.4}$$

hence removing $\mathbf{E}^s$ from this expression. $R_{\perp}$ is the Fresnel reflection coefficient (see (C5) and (C6)). Following the same procedure for the parallel polarization of the electric field and both magnetic field polarizations [4, pp. 928-929], the following expressions for tangential fields in medium 1 can be found:

$$\hat{\mathbf{n}}_1 \times \mathbf{E} = \left[(1 + R_{\perp})(\hat{\mathbf{p}} \cdot \hat{\mathbf{t}})\hat{\mathbf{n}}_1 \times \hat{\mathbf{t}} - (1 - R_{\parallel})(\hat{\mathbf{n}}_1 \cdot \hat{\mathbf{k}}_i)(\hat{\mathbf{p}} \cdot \hat{\mathbf{d}})\hat{\mathbf{t}}\right] E_0 \mathrm{e}^{-jk_1 \hat{\mathbf{k}}_i \cdot \mathbf{r}}, \tag{5.5}$$

$$\hat{\mathbf{n}}_1 \times \mathbf{H} = -\frac{1}{\eta_1}\left[(1 + R_{\perp})(\hat{\mathbf{p}} \cdot \hat{\mathbf{d}})\hat{\mathbf{n}}_1 \times \hat{\mathbf{t}} + (1 - R_{\parallel})(\hat{\mathbf{n}}_1 \cdot \hat{\mathbf{k}}_i)(\hat{\mathbf{p}} \cdot \hat{\mathbf{t}})\hat{\mathbf{t}}\right] E_0 \mathrm{e}^{-jk_1 \hat{\mathbf{k}}_i \cdot \mathbf{r}}, \tag{5.6}$$

where

$$\hat{\mathbf{t}} = \frac{\hat{\mathbf{k}}_i \times \hat{\mathbf{n}}_1}{|\hat{\mathbf{k}}_i \times \hat{\mathbf{n}}_1|} \text{ and } \hat{\mathbf{d}} = \hat{\mathbf{k}}_i \times \hat{\mathbf{t}}$$

create together with $\hat{\mathbf{k}}_i$ a locally suitable, orthonormal coordinate system.

Unfortunately, an analytic solution of the Stratton-Chu integral (5.1) even with the tangential plane approximation that leads to expressions (5.5)-(5.6) has not been found. Instead, some further simplifications have to be done. For large values of $k\sigma$, *stationary phase approximation* is usually made, which leads to the so-called Geometrical Optics model (GO). If the mean value of the slope of the surface is small, the *scalar approximation* can be used. The scalar approximation leads to PO, Physical Optics model.

5.1.2 Stationary Phase Approximation and Geometric Optics

The phase of (5.1) after (5.5) and (5.6) have been substituted is:

$$Q = jk_1(\hat{\mathbf{k}}_s - \hat{\mathbf{k}}_i) \cdot \mathbf{r}. \tag{5.7}$$

In the stationary phase approximation, all scattering in a particular direction is assumed only to originate from specular points. In other words, the phase Q is assumed to be constant in the neighborhood of the studied point (x, y), that is:

$$\frac{\partial Q}{\partial x} = \frac{\partial Q}{\partial y} = 0. \tag{5.8}$$

Using

$$\begin{aligned}
\hat{\mathbf{k}}_s &= \sin\theta_s \cos\phi_s \hat{\mathbf{x}} + \sin\theta_s \sin\phi_s \hat{\mathbf{y}} + \cos\theta_s \hat{\mathbf{z}} \\
\hat{\mathbf{k}}_i &= \sin\theta_i \cos\phi_i \hat{\mathbf{x}} + \sin\theta_i \sin\phi_i \hat{\mathbf{y}} - \cos\theta_i \hat{\mathbf{z}} \\
q_x &= k_1(\sin\theta_s \cos\phi_s - \sin\theta_i \cos\phi_i) \\
q_y &= k_1(\sin\theta_s \sin\phi_s - \sin\theta_i \sin\phi_i) \\
q_z &= k_1(\cos\theta_s + \cos\theta_i)
\end{aligned}$$

(where the angles are defined in Figure 5.2) in (5.7) together with (5.8) gives:

$$\begin{aligned}
& \frac{\partial Q}{\partial x} = \frac{\partial}{\partial x}(q_x x + q_y y + q_z z) = q_x + q_z \frac{\partial z}{\partial x} = 0 \\
\Rightarrow \quad & \frac{\partial z}{\partial x} = -\frac{q_x}{q_z}, \qquad (5.9)\\
& \frac{\partial Q}{\partial y} = \frac{\partial}{\partial y}(q_x x + q_y y + q_z z) = q_y + q_z \frac{\partial z}{\partial y} = 0 \\
\Rightarrow \quad & \frac{\partial z}{\partial y} = -\frac{q_y}{q_z}, \qquad (5.10)
\end{aligned}$$

which eliminates the dependence of $\hat{\mathbf{n}}_1 \times \mathbf{E}$ and $\hat{\mathbf{n}}_1 \times \mathbf{H}$ of the surface derivatives. The Stratton-Chu integral (5.1) can now be re-written as:

$$\mathbf{E}^s = K\hat{\mathbf{k}}_s \times [\hat{\mathbf{n}}_1 \times \mathbf{E} - \eta_1 \hat{\mathbf{k}}_s \times (\hat{\mathbf{n}}_1 \times \mathbf{H})] \int \exp[jk_1(\hat{\mathbf{k}}_s - \hat{\mathbf{k}}_i)\mathbf{r}]\mathrm{d}S. \tag{5.11}$$

The normalized radar cross section for the four different polarization modes can be computed using (5.11) together with

$$\sigma^0_{pq} = \frac{4\pi R^2 \mathsf{Re}\left\{\left\langle |\mathbf{E}^s_{pq}|^2 \right\rangle / \eta_s^\star\right\}}{A_0 \mathsf{Re}\left\{|E_0|^2/\eta_i^\star\right\}}. \tag{5.12}$$

In order to be able to compute the averages $\langle \bullet \rangle$, an assumption about the correlation function has to be made.

Assuming Gaussian correlation function, the radar cross section can be computed according to Ulaby et al. [4, chap. 12-4] and it becomes:

$$\sigma_{pq} = \frac{(k_1|f_{pq}|)^2}{2q_z^2\sigma^2|\rho''(0)|} \exp\left[-\frac{q_x^2 + q_y^2}{2q_z^2\sigma^2|\rho''(0)|}\right], \tag{5.13}$$

where f_{pq} can be found in (C1)-(C4) and $\rho''(0)$ is the second derivative of the correlation function at the origin ($\rho''(0) = \sqrt{2}/L$ for Gaussian correlation function).

5.1.3 Scalar Approximation and Physical Optics

Using stationary phase approximation, only non-coherent scattering is taken into consideration. However, if a surface has small slopes, scattering occurs also in the coherent way and scalar approximation has to be used. According to Ulaby et al. [4, p. 937], this approximation implies that:

1) all slope terms in the local coordinate unit vectors $\hat{\mathbf{t}}$ and $\hat{\mathbf{d}}$ can be omitted
2) the local surface normal $\hat{\mathbf{n}}$ can be expressed as

$$\hat{\mathbf{n}} \approx -\hat{\mathbf{x}} Z_x - \hat{\mathbf{y}} Z_y + \hat{\mathbf{z}},$$

   where $Z_{x,y}$ are local surface slopes in x- and y-directions.

Using these facts, the Stratton-Chu integral (5.1) can now be re-written into a scalar form:

$$E^s_{pq} = K E_0 \int U_{pq} \exp\left[j k_1 (\hat{\mathbf{k}}_s - \hat{\mathbf{k}}_i) \cdot \mathbf{r} \right] \mathrm{d}S, \tag{5.14}$$

where U_{pq} can all be written in the following way:

$$U_{pq} = a_0 + a_1 Z_x + a_2 Z_y, \tag{5.15}$$

where $a_{1,2,3}$ are coefficients dependent of polarization (the exact expression for U_{pq} can be found in Ulaby et al. [4, App. 12C]).

In order to find the ensemble average $\langle |\mathbf{E}^s|^2 \rangle$, the following expression is needed:

$$I = \iint \left\langle |U_{pq}|^2 \exp\left[j k_1 (\hat{\mathbf{n}}_s - \hat{\mathbf{n}}_i) \cdot (\mathbf{r} - \mathbf{r}') \right] \right\rangle \mathrm{d}S \mathrm{d}S' \tag{5.16}$$

together with the following approximation to the first order of slope:

$$|U_{pq}|^2 \approx |a_0|^2 + a_0 a_1^\star Z'_x + a_0^\star a_1 Z_x + a_0 a_2^\star Z'_y + a_0^\star a_2 Z_y \tag{5.17}$$

where $Z'_{x,y}$ is the surface slope in a point (x', y').

The integral in (5.16) can now be computed after using a Taylor expansion of the exponential term. The scattering coefficient can be found after some tedious transformations has been performed [4, pp. 938-941]. It consists of a sum of three terms:

$$\sigma^0_{pq} = \sigma^0_{pqc} + \sigma^0_{pqn} + \sigma^0_{pqs}, \tag{5.18}$$

where

$$\sigma^0_{pqc} = \pi k_i^2 |a_0|^2 \delta(q_x) \delta(q_y) \mathrm{e}^{-q_z^2 \sigma^2} \tag{5.19}$$

is the coherent term with $\delta(x)$ being the Dirac delta function,

$$\sigma^0_{pqn} = \frac{k_1^2 |a_0|^2}{4\pi} \exp(-q_z^2 \sigma^2) \sum_{n=1}^{\infty} \frac{(q_z^2 \sigma^2)^n}{n!} \iint\limits_{R^2} \rho^n \exp\left(j q_x u + j q_y v \right) \mathrm{d}u \mathrm{d}v \tag{5.20}$$

is the non-coherent term, and

$$\sigma^0_{pqs} = -\frac{j k_1^2 \sigma^2 q_z}{2\pi} \mathrm{e}^{-q_z^2 \sigma^2} \sum_{n=0}^{\infty} \frac{(q_z^2 \sigma^2)^n}{n!} \iint\limits_{R^2} \mathrm{Re} \left[a_0 \left(a_1^\star \frac{\partial \rho}{\partial u} + a_2^\star \frac{\partial \rho}{\partial v} \right) \right] \rho^n \mathrm{e}^{j q_x u + j q_y v} \mathrm{d}u \mathrm{d}v. \tag{5.21}$$

is a term due to surface slopes. This expression can be further simplified if surface correlation function is known.

In this project, a version of Physical Optics presented in de Roo [26], de Roo and Ulaby [27] is implemented. Compared to the model presented in Ulaby et al. [4], this model has some extra terms that have earlier been omitted and it generally gives better results.

5.2 First Order Small Perturbation Model

Small perturbation model (SPM) can be used in cases when the surface correlation length and its standard deviation are smaller than the wavelength. The validity regions presented in Figure 5.1 are not precise, although they may give an idea of when SPM may be applicable. The derivation of SPM is presented in Ulaby et al. [4, chap. 12-5] and here, it is only recapitulated.

The total field in medium 1 and medium 2 (primed) can be written as:

$$\mathbf{E} = E_x\hat{\mathbf{x}} + E_y\hat{\mathbf{y}} + E_z\hat{\mathbf{z}} \tag{5.22}$$
$$\mathbf{E}' = E'_x\hat{\mathbf{x}} + E'_y\hat{\mathbf{y}} + E'_z\hat{\mathbf{z}} \tag{5.23}$$

where

$$E_x = \frac{1}{2\pi}\iint\limits_{R^2} U_x(k_x,k_y)\exp(jk_xx + jk_yy - jk_zz)\,\mathrm{d}k_x\mathrm{d}k_y \tag{5.24}$$
$$E'_x = \frac{1}{2\pi}\iint\limits_{R^2} D_x(k_x,k_y)\exp(jk_xx + jk_yy + jk'_zz)\,\mathrm{d}k_x\mathrm{d}k_y \tag{5.25}$$

and

$$E_z = \frac{1}{2\pi}\iint\limits_{R^2} U_z(k_x,k_y)\exp(jk_xx + jk_yy - jk_zz)\,\mathrm{d}k_x\mathrm{d}k_y \tag{5.26}$$
$$E'_z = \frac{1}{2\pi}\iint\limits_{R^2} D_z(k_x,k_y)\exp(jk_xx + jk_yy + jk'_zz)\,\mathrm{d}k_x\mathrm{d}k_y \tag{5.27}$$

consist of only an incoherent part, and

$$E_y = \underbrace{\frac{1}{2\pi}\iint\limits_{R^2} U_y(k_x,k_y)\exp(jk_xx + jk_yy - jk_zz)\,\mathrm{d}k_x\mathrm{d}k_y}_{\text{incoherent}} + \underbrace{\mathrm{e}^{-jkx\sin\theta_i}(\mathrm{e}^{jkz\cos\theta_i} + R_\perp\mathrm{e}^{-jkz\cos\theta_i})}_{\text{coherent}}, \tag{5.28}$$
$$E'_y = \underbrace{\frac{1}{2\pi}\iint\limits_{R^2} D_y(k_x,k_y)\exp(jk_xx + jk_yy + jk'_zz)\,\mathrm{d}k_x\mathrm{d}k_y}_{\text{incoherent}} + \underbrace{(1+R_\perp)\mathrm{e}^{-jk'x\sin\theta_t + jk'z\cos\theta_s}}_{\text{coherent}}, \tag{5.29}$$

that also has a coherent part that originates from the incident wave together with the specularly reflected/transmitted wave. $U_{x,y,z}(k_x,k_y)$ and $D_{x,y,z}(k_x,k_y)$ are unknown field amplitudes in medium 1 and medium 2 that can be found using boundary conditions and divergence relations for electromagnetic fields as described in Ulaby et al. [4, p. 952] but omitted here.

Expression (5.24) can now be re-written using Taylor expansion of e^{-jk_zz} for small k_zz. Moreover, U_x can be expanded in a perturbation series $U_x = U_{x1} + U_{x2} + \ldots$:

$$E_x = \frac{1}{2\pi}\iint\limits_{R^2}(U_{x1} + U_{x2} + \ldots)(1 - jk_zz - \ldots)\exp(jk_xx + jk_yy)\,\mathrm{d}k_x\mathrm{d}k_y \tag{5.30}$$

and likewise for (5.25):

$$E'_x = \frac{1}{2\pi}\iint\limits_{R^2}(D_{x1} + D_{x2} + \ldots)(1 + jk'_zz - \ldots)\exp(jk_xx + jk_yy)\,\mathrm{d}k_x\mathrm{d}k_y, \tag{5.31}$$

where the expansions have been done up to second order. After some further mathematical transformations [4, pp. 953-955], fields U_{x1} and U_{y1} are found and presented explicitly and all other unknown fields in the integrands of (5.30)-(5.31) can be found using these fields.

In order to find explicit expressions for E_x and the other fields after the integration in (5.30)-(5.31), unit polarization vectors have to be chosen wisely. Some rather simple mathematical transformations in Ulaby et al. [4, pp. 956-960] lead to a final expression for the scattering coefficient σ^0_{pq} in the upper medium:

$$\sigma^0_{pq} = 8|k^2\sigma\cos\theta_i\cos\theta_s\alpha_{pq}|^2 W(k_x + k\sin\theta, k_y), \tag{5.32}$$

where α_{pq} can be found in (C27)-(C30) and

$$W(k_x, k_y) = \frac{1}{2\pi} \iint\limits_{R^2} \rho(u, v) \exp\left[-jk_x u - jk_y v\right] \mathrm{d}u\mathrm{d}v \tag{5.33}$$

is a Fourier transform of the surface correlation function. This model is the first order Small Perturbation Model. Higher order models are available but their expressions are much more complicated.

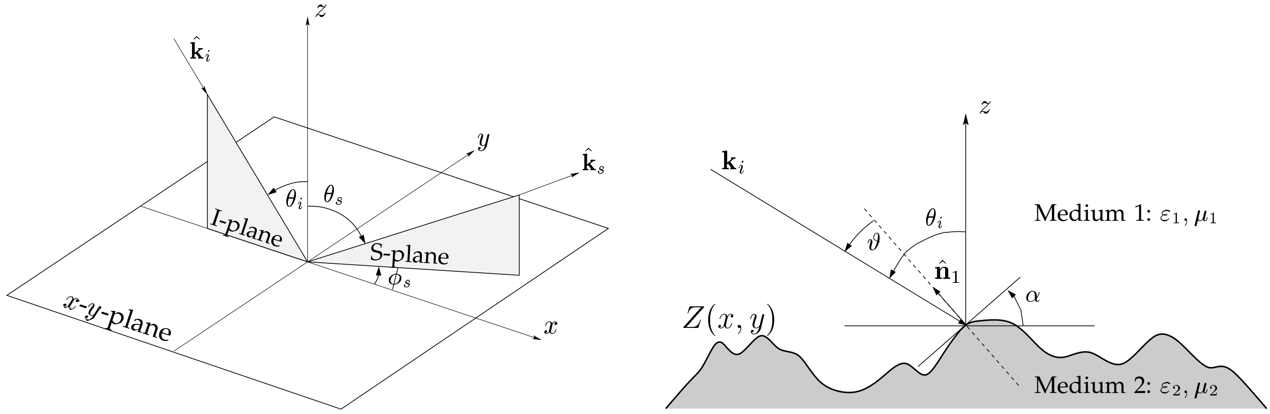

(a) 3D geometry (b) Incident plane geometry

Fig. 6.1: The geometry and nomenclature used for IEM derivation. For simplicity, ϕ_i has been set to 0 here.

6 Integral Equation Model

Integral Equation Model (IEM) was first introduced year 1992 by Fung, Li, and Chen [9]. It was the first method that tried to bridge the gap between KM and SPM that has been described in Section 5. The method is based on KM but has also an additional term that takes over in places where KM is not valid. The original IEM was built on several assumptions and simplifications that have been gradually reviewed and partially removed.

In this section, the derivation of the original IEM will be presented in detail as in Fung et al. [9] and Fung [22, chap. 4]. Thereafter, differences between the newer models and IEM will be presented in Section 7 and the latest version of IEM will be implemented and used for the scattering studies presented in Section 9.

6.1 Plane Waves

Assume that a plane wave with frequency ν propagates through a homogenous medium 1 (with dielectric permittivity ε_1 and magnetic permeability μ_1) in a direction described by a unit vector $\hat{\mathbf{k}}_i$. The wave number is then $k_1 = 2\pi\nu\sqrt{\varepsilon_1\mu_1}$ and the wave vector is $\mathbf{k}_i = k_1\hat{\mathbf{k}}_i$. The polarization of the wave is described by the polarization unit vector $\hat{\mathbf{p}}$. The electric and magnetic fields are then:

$$\mathbf{E}_i = \hat{\mathbf{p}} E_0 \mathrm{e}^{-j(\mathbf{k}_i \cdot \mathbf{r})} \tag{6.1}$$

$$\mathbf{H}_i = \hat{\mathbf{k}}_i \times \mathbf{E}_i / \eta_1 \tag{6.2}$$

where η_1 is the intrinsic impedance of medium 1. In both (6.1) and (6.2) a time factor $\mathrm{e}^{j\omega t}$ is understood.

The tangential surface fields in medium 1 can be written in the following way [4, 10, 22]:

$$\hat{\mathbf{n}}_1 \times \mathbf{E} = 2\hat{\mathbf{n}}_1 \times \mathbf{E}^i - \frac{2}{4\pi}\hat{\mathbf{n}}_1 \times \int \mathcal{E}^i \, \mathrm{d}s' \tag{6.3}$$

$$\hat{\mathbf{n}}_1 \times \mathbf{H} = 2\hat{\mathbf{n}}_1 \times \mathbf{H}^i + \frac{2}{4\pi}\hat{\mathbf{n}}_1 \times \int \mathcal{H}^i \, \mathrm{d}s' \tag{6.4}$$

and in medium 2 as:

$$\hat{\mathbf{n}}_2 \times \mathbf{E}^t = -\frac{2}{4\pi}\hat{\mathbf{n}}_2 \times \int \mathcal{E}^t \, \mathrm{d}s' \tag{6.5}$$

$$\hat{\mathbf{n}}_2 \times \mathbf{H}^t = \frac{2}{4\pi}\hat{\mathbf{n}}_2 \times \int \mathcal{H}^t \, \mathrm{d}s' \tag{6.6}$$

where

$$\mathcal{E}^i = jk_i\eta_i \left(\hat{\mathbf{n}}' \times \mathbf{H}'\right)\chi_i - \left(\hat{\mathbf{n}}' \times \mathbf{E}'\right) \times \nabla'\chi_i - \left(\hat{\mathbf{n}}' \cdot \mathbf{E}'\right)\nabla'\chi_i \tag{6.7}$$

$$\mathcal{H}^i = \frac{jk_i}{\eta_i}\left(\hat{\mathbf{n}}' \times \mathbf{E}'\right)\chi_i + \left(\hat{\mathbf{n}}' \times \mathbf{H}'\right) \times \nabla'\chi_i + \left(\hat{\mathbf{n}}' \cdot \mathbf{H}'\right)\nabla'\chi_i \tag{6.8}$$

$$\mathcal{E}^t = -jk_t\eta_t \left(\hat{\mathbf{n}}' \times \mathbf{H}'\right)\chi_t + \left(\hat{\mathbf{n}}' \times \mathbf{E}'\right) \times \nabla'\chi_t + \left(\hat{\mathbf{n}}' \cdot \mathbf{E}'\right)\nabla'\chi_t \left(1/\varepsilon_r\right) \tag{6.9}$$

$$\mathcal{H}^t = -\frac{jk_t}{\eta_t}\left(\hat{\mathbf{n}}' \times \mathbf{E}'\right)\chi_t - \left(\hat{\mathbf{n}}' \times \mathbf{H}'\right) \times \nabla'\chi_t - \left(\hat{\mathbf{n}}' \cdot \mathbf{H}'\right)\nabla'\chi_t \left(1/\mu_r\right) \tag{6.10}$$

where $\varepsilon_r = \varepsilon_2/\varepsilon_1$, $\mu_r = \mu_2/\mu_1$, $k_2 = k_1\sqrt{\varepsilon_r\mu_r} = 2\pi\nu\sqrt{\varepsilon_2\mu_2}$, $\eta_1 = \sqrt{\mu_1/\varepsilon_1}$, $\eta_2 = \sqrt{\mu_2/\varepsilon_2}$, and $\chi_{i,t}$ are Green functions as described in Appendix A (functions that solve the wave equation). Note that the primed versions of vectors and the operator ∇ indicate that they are expressed inside the integral. Also note, that

$$\hat{\mathbf{n}} \equiv \hat{\mathbf{n}}_1 = -\hat{\mathbf{n}}_2$$

(likewise for the primed version) and thus from now on, only $\hat{\mathbf{n}}$ will be used. The fields for medium 2 are found using fields for medium 1 and boundary conditions for electric and magnetic fields found in Kraus and Carver [28].

6.2 Kirchhoff Fields and Complementary Fields

The Integral Equation Model originates from the Kirchhoff Model with an extra complementary term. This way, the expression for total tangential field can be written as a sum of an expression for the Kirchhoff field and the complementary field:

$$\hat{\mathbf{n}} \times \mathbf{E} = (\hat{\mathbf{n}} \times \mathbf{E})_k + (\hat{\mathbf{n}} \times \mathbf{E})_c, \tag{6.11}$$

$$\hat{\mathbf{n}} \times \mathbf{H} = (\hat{\mathbf{n}} \times \mathbf{H})_k + (\hat{\mathbf{n}} \times \mathbf{H})_c. \tag{6.12}$$

Since the first term on the right hand side of (6.11) and (6.12) comes from the Kirchhoff approximation, one can re-write it as:

$$(\hat{\mathbf{n}} \times \mathbf{E})_k = \hat{\mathbf{n}} \times (\mathbf{E}^i + \mathbf{E}^r), \tag{6.13}$$

$$(\hat{\mathbf{n}} \times \mathbf{H})_k = \hat{\mathbf{n}} \times (\mathbf{H}^i + \mathbf{H}^r), \tag{6.14}$$

where the superscript r stands for the reflected fields. The complementary electric and magnetic fields are found from (6.3), (6.4), and (6.11)-(6.14):

$$(\hat{\mathbf{n}} \times \mathbf{E})_c \quad = \quad \hat{\mathbf{n}} \times (\mathbf{E}^i - \mathbf{E}^r) - \frac{2}{4\pi}\hat{\mathbf{n}} \times \int \mathcal{E}^i \, \mathrm{d}s', \tag{6.15}$$

$$(\hat{\mathbf{n}} \times \mathbf{H})_c \quad = \quad \hat{\mathbf{n}} \times (\mathbf{H}^i - \mathbf{H}^r) + \frac{2}{4\pi}\hat{\mathbf{n}} \times \int \mathcal{H}^i \, \mathrm{d}s'. \tag{6.16}$$

Now, the expressions for the reflected fields in (6.13) and (6.14) should be expressed as a function of the incident fields. For this, the Fresnel reflection coefficients are used.

6.3 Tangential Fields Expressed in the Local Vectors $\hat{\mathbf{t}}$ and $\hat{\mathbf{d}}$

The reflected field and the incident field can be related to each other through Fresnel coefficients:

$$R_{\|} = \frac{\varepsilon_r \cos\vartheta - \sqrt{\mu_r\varepsilon_r - \sin^2\vartheta}}{\varepsilon_r \cos\vartheta + \sqrt{\mu_r\varepsilon_r - \sin^2\vartheta}}, \tag{6.17}$$

$$R_{\perp} = \frac{\mu_r \cos\vartheta - \sqrt{\mu_r\varepsilon_r - \sin^2\vartheta}}{\mu_r \cos\vartheta + \sqrt{\mu_r\varepsilon_r - \sin^2\vartheta}}, \tag{6.18}$$

where ϑ is the local incidence angle (see Section 7.3 to see how it is chosen). In order to be able to use the Fresnel reflection coefficients, the fields in (6.13) and (6.14) should be divided into parallel and perpendicular components. Using the following orthogonal set of unit vectors (recall from Kirchhoff Model derivation in Section 5.1):

$$\hat{\mathbf{t}} = \frac{\hat{\mathbf{k}}_i \times \hat{\mathbf{n}}}{|\hat{\mathbf{k}}_i \times \hat{\mathbf{n}}|},\ \hat{\mathbf{d}} = \hat{\mathbf{k}}_i \times \hat{\mathbf{t}},\ \text{and}\ \hat{\mathbf{k}}_i = \hat{\mathbf{t}} \times \hat{\mathbf{d}}$$

one can re-write $\mathbf{E}^i = \hat{\mathbf{p}}E^i$ and $\mathbf{H}^i = \hat{\mathbf{k}}_i \times \mathbf{E}^i/\eta$ (where $E^i = |\mathbf{E}^i| = E_0\mathrm{e}^{-j(\hat{\mathbf{k}}_i\cdot\hat{\mathbf{r}})}$) as:

$$\mathbf{E}^i = \mathbf{E}^i_{\perp} + \mathbf{E}^i_{\|} = (\hat{\mathbf{p}} \cdot \hat{\mathbf{t}})\hat{\mathbf{t}}E^i + (\hat{\mathbf{p}} \cdot \hat{\mathbf{d}})\hat{\mathbf{d}}E^i, \tag{6.19}$$

$$\mathbf{H}^i = \mathbf{H}^i_{\perp} + \mathbf{H}^i_{\|} = \left[(\hat{\mathbf{p}} \cdot \hat{\mathbf{t}})\hat{\mathbf{d}}E^i + (\hat{\mathbf{p}} \cdot \hat{\mathbf{d}})\hat{\mathbf{t}}E^i\right]\Big/\eta. \tag{6.20}$$

The Fresnel coefficients can now be used in (6.13) and (6.14) and the following equations are derived after some mathematical transformations [22, p. 168]:

$$(\hat{\mathbf{n}} \times \mathbf{E}_{\perp})_k \quad = \quad (1 + R_{\perp})(\hat{\mathbf{p}} \cdot \hat{\mathbf{t}})\hat{\mathbf{n}} \times \hat{\mathbf{t}}E^i, \tag{6.21}$$

$$(\hat{\mathbf{n}} \times \mathbf{E}_{\|})_k \quad = \quad (1 - R_{\|})(\hat{\mathbf{p}} \cdot \hat{\mathbf{d}})\hat{\mathbf{n}} \times \hat{\mathbf{d}}E^i, \tag{6.22}$$

and similar for $\mathbf{H}$-fields.

After (6.19)-(6.22) have been used, the Kirchhoff tangential fields (6.13) and (6.14) can be expressed as a linear combination of two components in the tangential plane spanned by the two unit vectors $\hat{\mathbf{t}}$ and $\hat{\mathbf{n}} \times \hat{\mathbf{t}}$:

$$\begin{aligned}(\hat{\mathbf{n}} \times \mathbf{E})_k &= \hat{\mathbf{n}} \times \Big[(1-R_{\|})(\hat{\mathbf{p}}\cdot\hat{\mathbf{d}})\hat{\mathbf{d}} + (1+R_{\perp})(\hat{\mathbf{p}}\cdot\hat{\mathbf{t}})\hat{\mathbf{t}}\Big] E^i = && (6.23)\\ &= -\Big[(1-R_{\|})(\hat{\mathbf{p}}\cdot\hat{\mathbf{d}})(\hat{\mathbf{n}}\cdot\hat{\mathbf{k}}_i)\hat{\mathbf{t}} - (1+R_{\perp})(\hat{\mathbf{p}}\cdot\hat{\mathbf{t}})\hat{\mathbf{n}}\times\hat{\mathbf{t}}\Big] E^i && (6.24)\end{aligned}$$

and

$$\begin{aligned}(\hat{\mathbf{n}} \times \mathbf{H})_k &= \frac{1}{\eta}\hat{\mathbf{n}} \times \Big[(1-R_{\perp})(\hat{\mathbf{p}}\cdot\hat{\mathbf{t}})\hat{\mathbf{d}} - (1+R_{\|})(\hat{\mathbf{p}}\cdot\hat{\mathbf{d}})\hat{\mathbf{t}}\Big] E^i = && (6.25)\\ &= -\frac{1}{\eta}\Big[(1-R_{\perp})(\hat{\mathbf{p}}\cdot\hat{\mathbf{t}})(\hat{\mathbf{n}}\cdot\hat{\mathbf{k}}_i)\hat{\mathbf{t}} + (1+R_{\|})(\hat{\mathbf{p}}\cdot\hat{\mathbf{d}})\hat{\mathbf{n}}\times\hat{\mathbf{t}}\Big] E^i. && (6.26)\end{aligned}$$

The next step is to express the complementary fields in a similar way. Both terms on the right-hand side of (6.3) and (6.4) should be expressed in the integral form. By adding (6.3) and (6.4) to (6.5) and (6.6), respectively, and after applying boundary conditions, the following relations are found:

$$\begin{aligned}\hat{\mathbf{n}} \times \mathbf{E}^i &= \frac{1}{4\pi}\hat{\mathbf{n}} \times \int (\mathcal{E}^i - \mathcal{E}^t)\,\mathrm{d}s', && (6.27)\\ \hat{\mathbf{n}} \times \mathbf{H}^i &= -\frac{1}{4\pi}\hat{\mathbf{n}} \times \int (\mathcal{H}^i - \mathcal{H}^t)\,\mathrm{d}s'. && (6.28)\end{aligned}$$

In terms of unit vectors $\hat{\mathbf{t}}$ and $\hat{\mathbf{n}} \times \hat{\mathbf{t}}$, the left-hand side of (6.27) becomes

$$\hat{\mathbf{n}} \times \mathbf{E}^i = (\hat{\mathbf{p}}\cdot\hat{\mathbf{t}})\hat{\mathbf{n}}\times\hat{\mathbf{t}}E^i - (\hat{\mathbf{n}}\cdot\hat{\mathbf{k}}_i)(\hat{\mathbf{p}}\cdot\hat{\mathbf{d}})\hat{\mathbf{t}}E^i \quad (6.29)$$

while the right-hand side becomes:

$$\frac{1}{4\pi}\hat{\mathbf{n}} \times \int (\mathcal{E}^i - \mathcal{E}^t)\,\mathrm{d}s' = \frac{1}{4\pi}\hat{\mathbf{n}}\times\hat{\mathbf{t}}\left[(\hat{\mathbf{n}}\times\hat{\mathbf{t}})\cdot(\hat{\mathbf{n}}\times\int(\mathcal{E}^i - \mathcal{E}^t)\,\mathrm{d}s')\right] + \frac{1}{4\pi}\hat{\mathbf{t}}\left[\hat{\mathbf{t}}\cdot\hat{\mathbf{n}}\times\int(\mathcal{E}^i - \mathcal{E}^t)\,\mathrm{d}s'\right]. \quad (6.30)$$

Since (6.29) and (6.30) are equal, the corresponding vector components are equal and thus:

$$\begin{aligned}(\hat{\mathbf{p}}\cdot\hat{\mathbf{t}})E^i &= \frac{1}{4\pi}(\hat{\mathbf{n}}\times\hat{\mathbf{t}})\cdot\left(\hat{\mathbf{n}}\times\int(\mathcal{E}^i - \mathcal{E}^t)\,\mathrm{d}s'\right), && (6.31)\\ (\hat{\mathbf{n}}\cdot\hat{\mathbf{k}}_i)(\hat{\mathbf{p}}\cdot\hat{\mathbf{d}})E^i &= -\frac{1}{4\pi}\hat{\mathbf{t}}\cdot\hat{\mathbf{n}}\times\int(\mathcal{E}^i - \mathcal{E}^t)\,\mathrm{d}s', && (6.32)\end{aligned}$$

and correspondingly for (6.28).

In the similar way as in (6.27) and (6.28), the differences between the incident and reflected tangential surface fields found in (6.15) and (6.16) can be expressed as integrals:

$$\begin{aligned}\hat{\mathbf{n}} \times (\mathbf{E}^i - \mathbf{E}^r) &= \frac{1}{4\pi}(1-R_{\perp})(\hat{\mathbf{n}}\times\hat{\mathbf{t}})\cdot\left(\hat{\mathbf{n}}\times\int(\mathcal{E}^i - \mathcal{E}^t)\,\mathrm{d}s'\right)\hat{\mathbf{n}}\times\hat{\mathbf{t}} +\\ &\quad \frac{1}{4\pi}(1+R_{\|})\hat{\mathbf{t}}\cdot\left(\hat{\mathbf{n}}\times\int(\mathcal{E}^i - \mathcal{E}^t)\,\mathrm{d}s'\right)\hat{\mathbf{t}}, && (6.33)\\ \hat{\mathbf{n}} \times (\mathbf{H}^i - \mathbf{H}^r) &= -\frac{1}{4\pi}(1-R_{\|})(\hat{\mathbf{n}}\times\hat{\mathbf{t}})\cdot\left(\hat{\mathbf{n}}\times\int(\mathcal{H}^i - \mathcal{H}^t)\,\mathrm{d}s'\right)\hat{\mathbf{n}}\times\hat{\mathbf{t}} +\\ &\quad -\frac{1}{4\pi}(1+R_{\perp})\hat{\mathbf{t}}\cdot\left(\hat{\mathbf{n}}\times\int(\mathcal{H}^i - \mathcal{H}^t)\,\mathrm{d}s'\right)\hat{\mathbf{t}}. && (6.34)\end{aligned}$$

This way, both parts of the right-hand side of (6.15) and (6.16) can be expressed as a linear combination of vectors $\hat{\mathbf{t}}$ and $\hat{\mathbf{n}} \times \hat{\mathbf{t}}$:

$$\begin{aligned}(\hat{\mathbf{n}} \times \mathbf{E})_c &= -\frac{1}{4\pi}(\hat{\mathbf{n}}\times\hat{\mathbf{t}})\cdot\left(\hat{\mathbf{n}}\times\int\left[(1+R_{\perp})\mathcal{E}^i + (1-R_{\perp})\mathcal{E}^t\right]\,\mathrm{d}s'\right)\hat{\mathbf{n}}\times\hat{\mathbf{t}} +\\ &\quad -\frac{1}{4\pi}\hat{\mathbf{t}}\cdot\left(\hat{\mathbf{n}}\times\int\left[(1-R_{\|})\mathcal{E}^i + (1+R_{\|})\mathcal{E}^t\right]\,\mathrm{d}s'\right)\hat{\mathbf{t}}, && (6.35)\\ (\hat{\mathbf{n}} \times \mathbf{H})_c &= \frac{1}{4\pi}(\hat{\mathbf{n}}\times\hat{\mathbf{t}})\cdot\left(\hat{\mathbf{n}}\times\int\left[(1+R_{\|})\mathcal{H}^i + (1-R_{\|})\mathcal{H}^t\right]\,\mathrm{d}s'\right)\hat{\mathbf{n}}\times\hat{\mathbf{t}} +\\ &\quad +\frac{1}{4\pi}\hat{\mathbf{t}}\cdot\left(\hat{\mathbf{n}}\times\int\left[(1-R_{\perp})\mathcal{H}^i + (1+R_{\perp})\mathcal{H}^t\right]\,\mathrm{d}s'\right)\hat{\mathbf{t}}. && (6.36)\end{aligned}$$

This, combined with (6.23) and (6.25) gives us an expression for the total tangential surface fields expressed in local coordinates $\hat{\mathbf{t}}$ and $\hat{\mathbf{n}} \times \hat{\mathbf{t}}$, the Fresnel reflection coefficients $R_\perp$ and $R_\|$, and the incident fields:

$$\begin{aligned}
\hat{\mathbf{n}} \times \mathbf{E} &= -\Big[(1-R_\|)(\hat{\mathbf{p}}\cdot\hat{\mathbf{d}})(\hat{\mathbf{n}}\cdot\hat{\mathbf{k}}_i)\hat{\mathbf{t}} - (1+R_\perp)(\hat{\mathbf{p}}\cdot\hat{\mathbf{t}})\hat{\mathbf{n}}\times\hat{\mathbf{t}}\Big] E^i + \\
&\quad -\frac{1}{4\pi}(\hat{\mathbf{n}}\times\hat{\mathbf{t}})\cdot\left(\hat{\mathbf{n}}\times\int\left[(1+R_\perp)\mathcal{E}^i + (1-R_\perp)\mathcal{E}^t\right]\,\mathrm{d}s'\right)\hat{\mathbf{n}}\times\hat{\mathbf{t}} + \\
&\quad -\frac{1}{4\pi}\hat{\mathbf{t}}\cdot\left(\hat{\mathbf{n}}\times\int\left[(1-R_\|)\mathcal{E}^i + (1+R_\|)\mathcal{E}^t\right]\,\mathrm{d}s'\right)\hat{\mathbf{t}}, \qquad (6.37)\\
\hat{\mathbf{n}} \times \mathbf{H} &= -\frac{1}{\eta}\Big[(1-R_\perp)(\hat{\mathbf{p}}\cdot\hat{\mathbf{t}})(\hat{\mathbf{n}}\cdot\hat{\mathbf{k}}_i)\hat{\mathbf{t}} + (1+R_\|)(\hat{\mathbf{p}}\cdot\hat{\mathbf{d}})\hat{\mathbf{n}}\times\hat{\mathbf{t}}\Big] E^i + \\
&\quad +\frac{1}{4\pi}(\hat{\mathbf{n}}\times\hat{\mathbf{t}})\cdot\left(\hat{\mathbf{n}}\times\int\left[(1+R_\|)\mathcal{H}^i + (1-R_\|)\mathcal{H}^t\right]\,\mathrm{d}s'\right)\hat{\mathbf{n}}\times\hat{\mathbf{t}} + \\
&\quad +\frac{1}{4\pi}\hat{\mathbf{t}}\cdot\left(\hat{\mathbf{n}}\times\int\left[(1-R_\perp)\mathcal{H}^i + (1+R_\perp)\mathcal{H}^t\right]\,\mathrm{d}s'\right)\hat{\mathbf{t}}. \qquad (6.38)
\end{aligned}$$

Since the expressions for $\mathcal{E}^{i,t}$ and $\mathcal{H}^{i,t}$ are functions of $\mathbf{E}^i$ and $\mathbf{H}^i$, and

$$\hat{\mathbf{n}}\cdot\mathbf{E} = \frac{j\eta}{k}\nabla_s\cdot(\hat{\mathbf{n}}\times\mathbf{H}),$$
$$\hat{\mathbf{n}}\cdot\mathbf{H} = -\frac{j}{k\eta}\nabla_s\cdot(\hat{\mathbf{n}}\times\mathbf{E}),$$

according to Poggio and Miller [10], the total fields and the tangential surface tangential fields are connected through the surface divergence ∇_s thus making (6.37) and (6.38) integral equations. Equations (6.37) and (6.38) has to be solved. In order to do that, some simplifications need to be introduced.

6.4 Simplified Expressions for Tangential Surface Fields

In the first Integral Equation Model [9, 22], some approximations have been introduced in order to simplify the mathematical expressions. These approximations have gradually been removed in further work by the same research group [11–14, 20, 29–32] as well as by Álvarez-Pérez in his model IEM2M (see Section 7). In the following paragraphs, some important approximations will be pointed out in the same was as it is done in Álvarez-Pérez [33].

6.4.1 Kirchhoff Fields

The major complication in the expressions (6.24) and (6.26) for the Kirchhoff fields is the local dependence of the $\hat{\mathbf{d}}$- and $\hat{\mathbf{t}}$-vector. By adding and subtracting $\hat{\mathbf{n}}\times\Big[(1+R_\perp)(\hat{\mathbf{p}}\cdot\hat{\mathbf{d}})\hat{\mathbf{d}}\Big]$ or $\hat{\mathbf{n}}\times\left[(1-R_\|)(\hat{\mathbf{p}}\cdot\hat{\mathbf{t}})\hat{\mathbf{t}}\right]$ in the right-hand side of (6.24), the expression can be re-written as:

$$\begin{aligned}
(\hat{\mathbf{n}}\times\mathbf{E})_k &= \hat{\mathbf{n}}\times\Big[(1-R_\|)(\hat{\mathbf{p}}\cdot\hat{\mathbf{d}})\hat{\mathbf{d}} + (1+R_\perp)(\hat{\mathbf{p}}\cdot\hat{\mathbf{t}})\hat{\mathbf{t}}\Big] E^i = \\
&= \hat{\mathbf{n}}\times\Big[(1+R_\perp)\hat{\mathbf{p}} - (R_\perp + R_\|)(\hat{\mathbf{p}}\cdot\hat{\mathbf{d}})\hat{\mathbf{d}}\Big] E^i = \\
&= \hat{\mathbf{n}}\times\left[(1-R_\|)\hat{\mathbf{p}} + (R_\perp + R_\|)(\hat{\mathbf{p}}\cdot\hat{\mathbf{t}})\hat{\mathbf{t}}\right] E^i \qquad (6.39)
\end{aligned}$$

and similarly for (6.26):

$$\begin{aligned}
(\hat{\mathbf{n}}\times\mathbf{H})_k &= \frac{1}{\eta}\hat{\mathbf{n}}\times\Big[(1-R_\perp)(\hat{\mathbf{p}}\cdot\hat{\mathbf{t}})\hat{\mathbf{d}} - (1+R_\|)(\hat{\mathbf{p}}\cdot\hat{\mathbf{d}})\hat{\mathbf{t}}\Big] E^i = \\
&= \frac{1}{\eta}\hat{\mathbf{n}}\times\Big\{\hat{\mathbf{k}}_i\times\Big[(1-R_\perp)\hat{\mathbf{p}} + (R_\perp + R_\|)(\hat{\mathbf{p}}\cdot\hat{\mathbf{d}})\hat{\mathbf{d}}\Big]\Big\} E^i = \\
&= \frac{1}{\eta}\hat{\mathbf{n}}\times\Big\{\hat{\mathbf{k}}_i\times\left[(1+R_\|)\hat{\mathbf{p}} + (R_\perp + R_\|)(\hat{\mathbf{p}}\cdot\hat{\mathbf{t}})\hat{\mathbf{t}}\right]\Big\} E^i. \qquad (6.40)
\end{aligned}$$

If the incident field is vertically polarized, that is $\hat{\mathbf{p}} = \hat{\mathbf{v}}_i$, then $\hat{\mathbf{v}}_i\cdot\hat{\mathbf{t}} \ll 1$ for most surfaces. Additionally, $R_\| + R_\perp \ll 1$ for moderate incident angles. This reduces (6.39) to

$$(\hat{\mathbf{n}}\times\mathbf{E}_v)_k \approx (1-R_\|)\hat{\mathbf{n}}\times\hat{\mathbf{v}}_i E^i \qquad (6.41)$$

and a similar derivation, but with $\hat{\mathbf{p}} = \hat{\mathbf{h}}_i$ and $\hat{\mathbf{h}}_i \cdot \hat{\mathbf{d}} \ll 1$ gives a simplified version of the Kirchhoff field for horizontal polarization:

$$(\hat{\mathbf{n}} \times \mathbf{E}_h)_k \approx (1 + R_\perp)\hat{\mathbf{n}} \times \hat{\mathbf{h}}_i E^i. \tag{6.42}$$

For magnetic fields, the corresponding results are:

$$\begin{aligned}(\hat{\mathbf{n}} \times \mathbf{H}_v)_k &\approx \frac{1}{\eta}(1 + R_\parallel)\hat{\mathbf{n}} \times (\hat{\mathbf{k}}_i \times \hat{\mathbf{v}}_i)E^i, & (6.43)\\ (\hat{\mathbf{n}} \times \mathbf{H}_h)_k &\approx \frac{1}{\eta}(1 - R_\perp)\hat{\mathbf{n}} \times (\hat{\mathbf{k}}_i \times \hat{\mathbf{h}}_i)E^i. & (6.44)\end{aligned}$$

For cross-polarization, the both terms in (6.39) and (6.40) including the $1 \pm R_{\parallel,\perp}$-terms are comparable in size with $R_\parallel + R_\perp$ and none of them can be dropped. One other simplification is made in Fung [22, chap. 4] instead. The average of the second and third line in (6.39) and (6.40) is used together with the assumption that the $R_\parallel + R_\perp$-term is smaller than the others gaining:

$$\begin{aligned}(\hat{\mathbf{n}} \times \mathbf{E}_p)_k &\approx (1 - R)(\hat{\mathbf{n}} \times \hat{\mathbf{p}})E^i, & (6.45)\\ (\hat{\mathbf{n}} \times \mathbf{H}_p)_k &\approx \frac{1}{\eta}(1 + R)\hat{\mathbf{n}} \times (\hat{\mathbf{k}}_i \times \hat{\mathbf{p}})E^i. & (6.46)\end{aligned}$$

with $R = \frac{R_\parallel - R_\perp}{2}$. This result applies for both HV and VH polarization. The approximations made for cross-polarization are less accurate than the corresponding ones made for co-polarization.

The assumptions above are the first simplifications made in the IEM and they have first been removed in AIEM [14]. From here on, the assumptions $\hat{\mathbf{v}}_i \cdot \hat{\mathbf{t}} \ll 1$ and $\hat{\mathbf{h}}_i \cdot \hat{\mathbf{d}} \ll 1$ will be referred to as ***A1a*** and $R_\parallel + R_\perp \ll 1$ as ***A1b***.

6.4.2 Complementary Fields

In order to remove the unknowns under the integral sign in (6.35) and (6.36), the same approximations as for the Kirchhoff fields (that is to remove a term including $R_\parallel + R_\perp$) are used in the expressions for $\mathcal{E}^i$ and $\mathcal{E}^t$. Moreover, in order to make some further mathematical simplifications, the following two terms are added and removed in expressions (6.35) and (6.36) in vertical polarization case:

$$(1 - R_\parallel)\frac{1}{4\pi}(\hat{\mathbf{n}} \times \hat{\mathbf{t}})(\hat{\mathbf{n}} \times \hat{\mathbf{t}} \cdot \hat{\mathbf{n}} \times \int \mathcal{E}_v^i \,\mathrm{d}s')$$

and

$$(1 + R_\parallel)\frac{1}{4\pi}(\hat{\mathbf{n}} \times \hat{\mathbf{t}})(\hat{\mathbf{n}} \times \hat{\mathbf{t}} \cdot \hat{\mathbf{n}} \times \int \mathcal{E}_v^t \,\mathrm{d}s')$$

yielding:

$$\begin{aligned}(\hat{\mathbf{n}} \times \mathbf{E}_v)_c &= -(1 - R_\parallel)\frac{1}{4\pi}\hat{\mathbf{n}} \times \int \mathcal{E}_v^i \,\mathrm{d}s' - (1 + R_\parallel)\frac{1}{4\pi}\hat{\mathbf{n}} \times \int \mathcal{E}_v^t \,\mathrm{d}s' + \\ &\quad -(R_\parallel + R_\perp)\frac{1}{4\pi}\hat{\mathbf{n}} \times \hat{\mathbf{t}}\left\{\hat{\mathbf{n}} \times \hat{\mathbf{t}} \cdot \left[\hat{\mathbf{n}} \times \int (\mathcal{E}_v^i - \mathcal{E}_v^t)\,\mathrm{d}s'\right]\right\} \approx \\ &\approx -\frac{1}{4\pi}\hat{\mathbf{n}} \times \int \left[(1 - R_\parallel)\mathcal{E}_v^i + (1 + R_\parallel)\mathcal{E}_v^t\right] \mathrm{d}s' \end{aligned} \tag{6.47}$$

where assumptions ***A1a*** and ***A1b*** have been used to remove the last term including $R_\parallel + R_\perp$. The integral that follows $R_\parallel + R_\perp$ can be substituted using (6.27) and $\mathbf{E}_v^i = E^i\hat{\mathbf{v}}_i$, which together with ***A1a*** gives a small value of $(\hat{\mathbf{n}} \times \hat{\mathbf{t}}) \cdot (\hat{\mathbf{n}} \times \hat{\mathbf{v}}_i)E^i$.

A similar expression is found in the same way for the magnetic field:

$$(\hat{\mathbf{n}} \times \mathbf{H}_v)_c \approx \frac{1}{4\pi}\hat{\mathbf{n}} \times \int \left[(1 + R_\parallel)\mathcal{H}_v^i + (1 - R_\parallel)\mathcal{H}_v^t\right] \mathrm{d}s', \tag{6.48}$$

and for both electric and magnetic fields in the horizontal polarization case:

$$\begin{aligned}(\hat{\mathbf{n}} \times \mathbf{E}_h)_c &\approx -\frac{1}{4\pi}\hat{\mathbf{n}} \times \int \left[(1 + R_\perp)\mathcal{E}_h^i + (1 - R_\perp)\mathcal{E}_h^t\right] \mathrm{d}s', \\ (\hat{\mathbf{n}} \times \mathbf{H}_h)_c &\approx \frac{1}{4\pi}\hat{\mathbf{n}} \times \int \left[(1 - R_\perp)\mathcal{H}_h^i + (1 + R_\perp)\mathcal{H}_h^t\right] \mathrm{d}s'. \end{aligned} \tag{6.49}$$

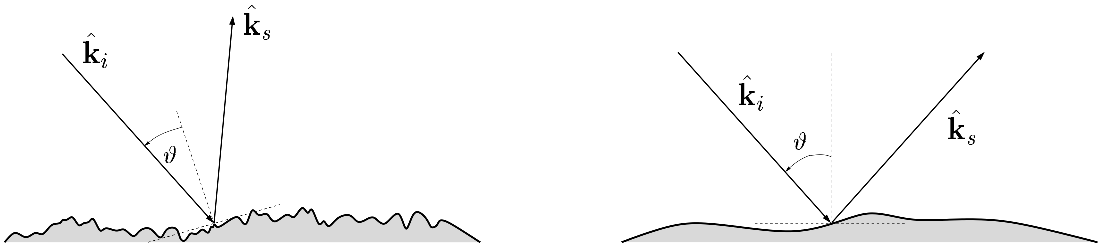

(a) Specular angle

(b) Incident angle

Fig. 6.2: The choice of angle for the Fresnel coefficients. For a surface with short correlation length (low kL), the only contribution in a particular direction comes from specular reflection and the angle ϑ is thus set to the specular angle (half the angle between $-\hat{\mathbf{k}}_i$ and $\hat{\mathbf{k}}_s$). For a very slowly undulating surface, the surface is close to horizontal and the used angle will then be the incident angle ($\vartheta = \theta_i$).

The cross-polarization terms are found using the same routine as for Kirchhoff fields — by averaging two equal expressions for $(\hat{\mathbf{n}} \times \mathbf{E}_p)_c$ and removing the $R_\parallel + R_\perp$–term:

$$(\hat{\mathbf{n}} \times \mathbf{E}_p)_c \approx -\frac{1}{4\pi}\hat{\mathbf{n}} \times \int \left[(1-R)\mathcal{E}_p^i + (1+R)\mathcal{E}_p^t\right] \mathrm{d}s', \tag{6.50}$$

$$(\hat{\mathbf{n}} \times \mathbf{H}_p)_c \approx \frac{1}{4\pi}\hat{\mathbf{n}} \times \int \left[(1+R)\mathcal{H}_p^i + (1-R)\mathcal{H}_p^t\right] \mathrm{d}s'. \tag{6.51}$$

6.5 Far Fields

Having the tangential surface fields in simplified versions, it is now possible to compute the electric and magnetic fields far away from the surface using the Stratton-Chu integral derived in Appendix B:

$$\begin{aligned} E_{pq}^s &= \hat{\mathbf{q}} \cdot \mathbf{E}_{pq}^s = -\frac{jk\mathrm{e}^{-jkr}}{4\pi r}\hat{\mathbf{q}} \cdot \hat{\mathbf{r}} \times \int \left[(\hat{\mathbf{n}} \times \mathbf{E}_p^s) - \hat{\mathbf{r}} \times (\hat{\mathbf{n}} \times \mathbf{H}_p^s)\eta\right] \mathrm{e}^{j\hat{\mathbf{k}}_i \cdot \mathbf{r}}\, \mathrm{d}s = \\ &= -\frac{jk\mathrm{e}^{-jkr}}{4\pi r} \int \left[\hat{\mathbf{q}} \times \hat{\mathbf{k}}_i \cdot (\hat{\mathbf{n}} \times \mathbf{E}_p^s) + \hat{\mathbf{q}} \cdot (\hat{\mathbf{n}} \times \mathbf{H}_p^s)\eta\right] \mathrm{e}^{j\hat{\mathbf{k}}_i \cdot \hat{\mathbf{r}}}\, \mathrm{d}s. \end{aligned} \tag{6.52}$$

and since $\hat{\mathbf{n}} \times \hat{\mathbf{E}} = (\hat{\mathbf{n}} \times \hat{\mathbf{E}})_k + (\hat{\mathbf{n}} \times \hat{\mathbf{E}})_c$, then:

$$\begin{aligned} E_{pq}^s &= E_{pq}^k + E_{pq}^c = \\ &= -\frac{jk_s E_0 \mathrm{e}^{-jk_s R_0}}{4\pi R_0}\left\{\int f_{pq} \exp\left[j\hat{\mathbf{r}} \cdot (\hat{\mathbf{k}}_s - \hat{\mathbf{k}}_i)\mathrm{d}x\mathrm{d}y + \right.\right. \\ &\left.\left. + \frac{1}{8\pi^2}\int \mathcal{F}_{pq} \exp\left[ju(x-x') + jv(y-y') + j\hat{\mathbf{k}}_s \cdot \hat{\mathbf{r}}' - j\hat{\mathbf{k}}_i \cdot \hat{\mathbf{r}}'\right]\mathrm{d}x\mathrm{d}y\mathrm{d}x'\mathrm{d}y'\mathrm{d}u\mathrm{d}v\right\}\right. \end{aligned} \tag{6.53}$$

where

$$f_{pq} = \frac{D_1}{E^i}[\hat{\mathbf{q}} \times \hat{\mathbf{k}}_s \cdot (\hat{\mathbf{n}} \times \hat{\mathbf{E}}_p)_k + \eta\hat{\mathbf{q}} \cdot (\hat{\mathbf{n}} \times \mathbf{H}_p)_k], \tag{6.54}$$

$$\mathcal{F}'_{pq} = \frac{8\pi^2 D_1}{E^i}[\hat{\mathbf{q}} \times \hat{\mathbf{k}}_s \cdot (\hat{\mathbf{n}} \times \hat{\mathbf{E}}_p)_c + \eta\hat{\mathbf{q}} \cdot (\hat{\mathbf{n}} \times \mathbf{H}_p)_c]. \tag{6.55}$$

where $D_1 = (Z_y^2 + Z_x^2 + 1)^{1/2}$, $Z_x = \frac{\partial Z(x,y)}{\partial x}$, and $Z_y = \frac{\partial Z(x,y)}{\partial y}$. $\mathcal{F}_{pq}$ becomes $\mathcal{F}'_{pq}$ after χ and $\nabla\chi$ have been replaced in the expressions for the complementary tangential surface fields by a proper Green's function and its gradient and the integrations with respect to u, v, x', and y' have been carried out.

In the fields f_{pq} and $\mathcal{F}_{pq}$, there are expressions for $R_\perp$ and $R_\parallel$ that include the local incidence angle ϑ. This angle cannot be known exactly and instead, there are some approximations made in the model. This angle is chosen to be either the incident angle θ_i if the correlation length is large enough, or the specular angle (half the angle between $\hat{\mathbf{k}}_s$ and $-\hat{\mathbf{k}}_i$), see Figure 6.2. This approximation will from now on be referred to as ***A2*** and will be discussed later in Section 7.3.

6.6 Approximate Expressions for f_{pq}

In order to find expressions for f_{pq} that are practical and applicable, expressions (6.41)-(6.46) are used to find:

$$\begin{aligned}
f_{vv} &\approx -\left[(1-R_{\|})\hat{\mathbf{h}}_s\cdot(\hat{\mathbf{n}}\times\hat{\mathbf{v}}_i)+(1+R_{\|})\hat{\mathbf{v}}_s\cdot(\hat{\mathbf{n}}\times\hat{\mathbf{h}}_i)\right]D_1, &(6.56)\\
f_{hh} &\approx \left[(1-R_{\perp})\hat{\mathbf{h}}_s\cdot(\hat{\mathbf{n}}\times\hat{\mathbf{v}}_i)+(1+R_{\perp})\hat{\mathbf{v}}_s\cdot(\hat{\mathbf{n}}\times\hat{\mathbf{h}}_i)\right]D_1, &(6.57)\\
f_{hv} &= \left[(1-R_{\|})\hat{\mathbf{v}}_s\cdot(\hat{\mathbf{n}}\times\hat{\mathbf{v}}_i)-(1+R_{\|})\hat{\mathbf{h}}_s\cdot(\hat{\mathbf{n}}\times\hat{\mathbf{h}}_i)\right]D_1+\\
&\quad +(R_{\perp}+R_{\|})(\hat{\mathbf{v}}_i\cdot\hat{\mathbf{t}})\left[\hat{\mathbf{v}}_s\cdot(\hat{\mathbf{n}}\times\hat{\mathbf{t}})-\hat{\mathbf{h}}_s\cdot(\hat{\mathbf{n}}\times\hat{\mathbf{d}})\right]D_1, &(6.58)\\
f_{vh} &= \left[(1-R_{\perp})\hat{\mathbf{v}}_s\cdot(\hat{\mathbf{n}}\times\hat{\mathbf{v}}_i)-(1+R_{\perp})\hat{\mathbf{h}}_s\cdot(\hat{\mathbf{n}}\times\hat{\mathbf{h}}_i)\right]D_1+\\
&\quad -(R_{\perp}+R_{\|})(\hat{\mathbf{h}}_i\cdot\hat{\mathbf{d}})\left[\hat{\mathbf{v}}_s\cdot(\hat{\mathbf{n}}\times\hat{\mathbf{t}})-\hat{\mathbf{h}}_s\cdot(\hat{\mathbf{n}}\times\hat{\mathbf{d}})\right]D_1. &(6.59)
\end{aligned}$$

6.7 Approximate Expressions for $\mathcal{F}_{pq}$

The complementary field coefficient $\mathcal{F}_{pq}$ has a very complicated expression involving cross products, integrals and Green's function. First, Green's function used in (6.7)-(6.10) is written in its spectral representation:

$$\chi(\mathbf{r},\mathbf{r}')=-\frac{1}{2\pi}\int\frac{j}{q}e^{ju(x-x')+jv(y-y')-jq|z-z'|}\,\mathrm{d}u\mathrm{d}v \tag{6.60}$$

where $q=(k^2-u^2-v^2)^{1/2}$ (q can be either $q_i=(k_1^2-u^2-v^2)^{1/2}$ or $q_t=(k_2^2-u^2-v^2)^{1/2}$ depending on the medium). The gradient becomes

$$\nabla\chi(\mathbf{r},\mathbf{r}')=-\frac{1}{2\pi}\int\frac{\mathbf{g}}{q}e^{ju(x-x')+jv(y-y')-jq|z-z'|}\,\mathrm{d}u\mathrm{d}v, \tag{6.61}$$

where $\mathbf{g}=u\hat{\mathbf{x}}+v\hat{\mathbf{y}}\pm q\hat{\mathbf{z}}$.

At this point, there is an approximation made in the first version of IEM [22]. This approximation will be called ***A3*** and it consists of removing the terms including q in the expressions for χ and $\nabla\chi$. This is justified by the two following arguments:

- factor $jq|z-z'|$ is small if two points on a surface are close together and hence can be removed,
- factor $\pm q\hat{\mathbf{z}}$ can be removed due to the fact that most of the factors with minus sign will cancel the factors with plus sign in the integral and thus the whole contribution will be zero.

These assumptions give simpler expressions for (6.7)-(6.10):

$$\begin{aligned}
\mathcal{E}_p^i &= \int\frac{P}{2\pi q_i}\left[k_1\eta_1(\hat{\mathbf{n}}'\times\mathbf{H}_p')+(\hat{\mathbf{n}}'\times\mathbf{E}_p')\times\mathbf{g}+(\hat{\mathbf{n}}'\cdot\mathbf{E}_p')\mathbf{g}\right]\mathrm{d}u\mathrm{d}v, &(6.62)\\
\mathcal{E}_p^t &= -\int\frac{P}{2\pi q_t}\left[k_2\eta_2(\hat{\mathbf{n}}'\times\mathbf{H}_p')+(\hat{\mathbf{n}}'\times\mathbf{E}_p')\times\mathbf{g}+(\hat{\mathbf{n}}'\cdot\mathbf{E}_p')\mathbf{g}/\varepsilon_r\right]\mathrm{d}u\mathrm{d}v, &(6.63)\\
\mathcal{H}_p^i &= \int\frac{P}{2\pi q_i}\left[\frac{k_1}{\eta_1}(\hat{\mathbf{n}}'\times\mathbf{E}_p')-(\hat{\mathbf{n}}'\times\mathbf{H}_p')\times\mathbf{g}+(\hat{\mathbf{n}}'\cdot\mathbf{H}_p')\mathbf{g}\right]\mathrm{d}u\mathrm{d}v, &(6.64)\\
\mathcal{H}_p^t &= -\int\frac{P}{2\pi q_t}\left[\frac{k_2}{\eta_2}(\hat{\mathbf{n}}'\times\mathbf{E}_p')-(\hat{\mathbf{n}}'\times\mathbf{H}_p')\times\mathbf{g}+(\hat{\mathbf{n}}'\cdot\mathbf{H}_p')\mathbf{g}/\mu_r\right]\mathrm{d}u\mathrm{d}v, &(6.65)
\end{aligned}$$

where $\mathbf{q}=u\hat{\mathbf{x}}+v\hat{\mathbf{y}}$ and the phase factor P is $P=\exp\left[ju(x-x')+jv(y-y')\right]$.

Next, the expressions above are used together with the simplified complementary tangential fields (6.47)-(6.51) in order to find the expressions for F_{pq}' found in (6.55). First, the integrations with respect to x', y', u, and v are carried out. Next, the remaining tangential fields inside $\mathcal{F}_{pq}$ are replaced by their approximative values — namely the Kirchhoff tangential fields. The procedures described in this paragraph are very lengthy and are omitted. They follow exactly the derivation found in Fung [22, pp. 181-185].

The resulting complementary field coefficient for HH becomes:

$$\begin{aligned}\mathcal{F}_{hh} \approx\ & \hat{\mathbf{v}}_s \cdot \hat{\mathbf{n}} \times \left\{ - \left[(1+R_\perp)\frac{k}{q} - (1-R_\perp)\frac{k_t\eta_t}{q_t\eta} \right] (1-R_\perp)(\hat{\mathbf{n}} \times \hat{\mathbf{v}}_i) + \right. \\ & - \left[(1+R_\perp)/q - (1-R_\perp)/q_t \right] (1+R_\perp)(\hat{\mathbf{n}} \times \hat{\mathbf{h}}_i) \times \mathbf{q} + \\ & \left. - \left[(1+R_\perp)/q - (1-R_\perp)/(\varepsilon_r q_t) \right] (1-R_\perp)(\hat{\mathbf{n}} \cdot \hat{\mathbf{h}}_i) \times \mathbf{q} \right\} + \\ & + \hat{\mathbf{h}}_s \cdot \hat{\mathbf{n}} \times \left\{ \left[(1-R_\perp)\frac{k}{q} - (1+R_\perp)\frac{k_t\eta_t}{q_t\eta} \right] (1+R_\perp)(\hat{\mathbf{n}} \times \hat{\mathbf{h}}_i) + \right. \\ & - \left[(1-R_\perp)/q - (1+R_\perp)/q_t \right] (1-R_\perp)(\hat{\mathbf{n}} \times \hat{\mathbf{v}}_i) \times \mathbf{q} + \\ & \left. - \left[(1-R_\perp)/q - (1+R_\perp)/(\varepsilon_r q_t) \right] (1+R_\perp)(\hat{\mathbf{n}} \cdot \hat{\mathbf{v}}_i) \times \mathbf{q} \right\} \end{aligned} \tag{6.66}$$

while the other coefficients can be found in Fung [22, pp. 183-184].

6.8 Average Power and Scattering Coefficient

In order to find the incoherent power for the scattered field E^s_{pq}, the mean-squared power is subtracted from the total power:

$$\begin{aligned} P^{incoh}_{pq} &= P^{total}_{pq} - P^{mean}_{pq} = \\ &= \langle E^s_{pq} E^{s\,\star}_{pq} \rangle - \langle E^s_{pq} \rangle \langle E^s_{pq} \rangle^\star = \\ &= \left(\langle E^k_{pq} E^{k\,\star}_{pq} \rangle - \langle E^k_{pq} \rangle \langle E^k_{pq} \rangle^\star \right) + \\ & \quad + 2\mathrm{Re} \left(\langle E^c_{pq} E^{k\,\star}_{pq} \rangle - \langle E^c_{pq} \rangle \langle E^k_{pq} \rangle^\star \right) + \\ & \quad + \left(\langle E^c_{pq} E^{c\,\star}_{pq} \rangle - \langle E^c_{pq} \rangle \langle E^c_{pq} \rangle^\star \right) = \\ &= P^k_{pq} + P^{kc}_{pq} + P^c_{pq} \end{aligned} \tag{6.67}$$

where $\langle \bullet \rangle$ means average of $\bullet$ over all realizations of the random surface $Z(x, y)$, * is the complex conjugate, and Re is the real part. Now, from the radar equation and the expression for the radar cross section (2.9):

$$\sigma^0_{pq} = \frac{P^{incoh}_{pq}}{E_0^2} \cdot \frac{4\pi R^2}{A_0}. \tag{6.68}$$

In order to find an explicit expression for σ^0, an assumption regarding the surface has to be made so that all the averages in (6.67) can be found. In Fung [22, pp. 232-245], a detailed description of how to transform the complicated expression that (6.67) gives into a more easy to implement expression is presented. The final result is also re-written so that the final scattering coefficient consists of two parts: one part that originates from direct scattering from the surface (σ^S_{pq}), and the other part that originates from multiple scattering from the surface:

$$\sigma_{pq} = \sigma^S_{pq} + \sigma^M_{pq}. \tag{6.69}$$

In the single scattering case, the coefficient is

$$\sigma^S_{pq} = \frac{k_1^2}{2} \exp\left[-\sigma^2 (k_{iz}^2 + k_{sz}^2) \right] \sum_{n=1}^{\infty} \left[\sigma^{2n} \left| I^n_{pq} \right| \frac{W^{(n)}(k_{sx} - k_{ix}, k_{sy} - k_{iy})}{n!} \right] \tag{6.70}$$

where

$$I^n_{pq} = (k_{sz} - k_{iz})^n f_{pq} \exp\left(-\sigma^2 k_{iz} k_{sz} \right) + \frac{k^n_{sz} \mathcal{F}_{pq}(-k_{ix}, -k_{iy}) + k^n_{iz} \mathcal{F}_{pq}(-k_{sx}, -k_{sy})}{2}, \tag{6.71}$$

and $W^{(n)}(u, v)$ is the nth power Fourier spectrum of the correlation function, see Section 4.2.2. The multiple scattering term can be found in Fung [22, p. 247] and is omitted here. The expressions for the Kirchhoff fields f_{pq} can be found in (C1)-(C4) while the expressions for the complementary fields $\mathcal{F}_{pq}$ for IEM can be found in (C35)-(C42). In both single and multiple scattering cases, large $k\sigma$ results in a negligible second part of the sum in (6.71) and the sum in (6.70) can be replaced with an exponential function which gives the Geometrical Optics model after stationary phase approximation (see Section C.2).

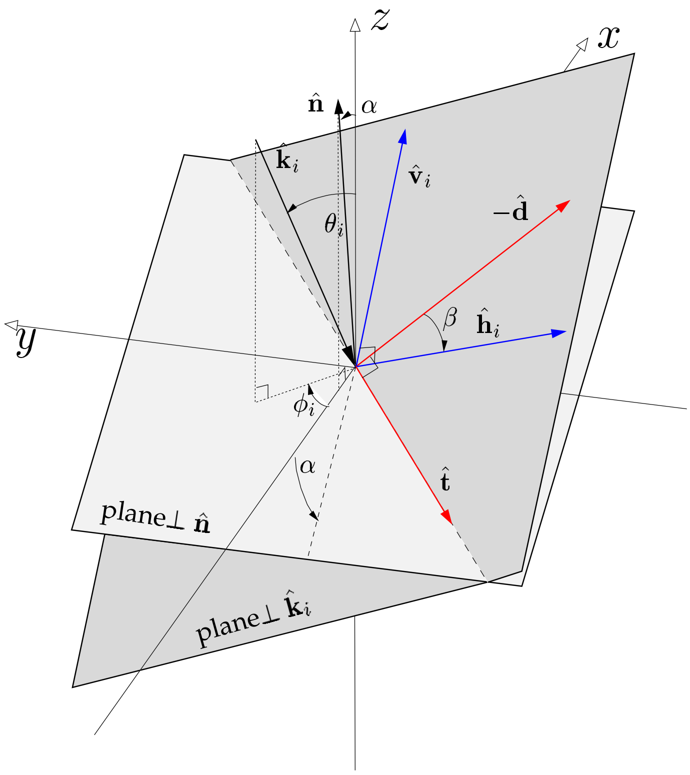

Fig. 7.1: The local coordinate system consists of the three vectors: $\hat{\mathbf{t}} = \frac{\hat{\mathbf{k}}_i \times \hat{\mathbf{n}}}{|\hat{\mathbf{k}}_i \times \hat{\mathbf{n}}|}$, $\hat{\mathbf{d}} = \hat{\mathbf{k}}_i \times \hat{\mathbf{t}}$, and $\hat{\mathbf{k}}_i = \hat{\mathbf{t}} \times \hat{\mathbf{d}}$. The two polarization vectors $\hat{\mathbf{v}}_i$ and $\hat{\mathbf{h}}_i$ are taken to be almost orthogonal to $\hat{\mathbf{t}}$ and $\hat{\mathbf{d}}$, respectively, according to ***A1a*** ($\hat{\mathbf{v}}_i \cdot \hat{\mathbf{t}} \ll 1$). The angle between the x-axis and the tangent plane that is perpendicular to $\hat{\mathbf{n}}$ is α and the coordinate axes are chosen so, that only a rotation around y-axis is present. Then, the angle β is close to $90°$ if the azimuth angle ϕ_i is small, that is the rotation of the plane perpendicalar to $\hat{\mathbf{k}}_i$ around x- and z axis is very small.

7 Assumptions and Simplifications in IEM-based Models

Previously in the text, a derivation of the Integral Equation Model was presented. Some assumptions were made and these assumptions will now be explained and justified.

7.1 Assumption A1a — Low $\hat{\mathbf{v}}_i \cdot \hat{\mathbf{t}}$

Assumption ***A1*** that was made on page 22 was:

$$\hat{\mathbf{v}}_i \cdot \hat{\mathbf{t}} \ll 1 \tag{7.1}$$

which is equivalent to [33]

$$\hat{\mathbf{h}}_i \cdot \hat{\mathbf{d}} \ll 1 \tag{7.2}$$

and to

$$(\hat{\mathbf{n}} \times \hat{\mathbf{t}}) \cdot (\hat{\mathbf{n}} \times \hat{\mathbf{v}}_i) \ll 1. \tag{7.3}$$

Using the geometry in Figure 7.1, it can be seen that this assumption originates from the fact that $\hat{\mathbf{k}}_i$ and $\hat{\mathbf{n}}$ are parallel or almost parallel (they both lie in the plane of incidence). This assumption makes the mathematics described in Section 6 much easier and it is fairly justified for backscattering and forward scattering. However, it is not valid for bistatic scattering and has been removed in the latest version of the Advanced Integral Equation Model [14]. In Figure 7.2, one can see what happens with $\hat{\mathbf{v}}_i \cdot \hat{\mathbf{t}}$ for some chosen angles θ_i, ϕ_i, and α (the local slope angle).

7.2 Assumption A1b — $R_{\|} + R_{\perp} \ll 1$

Assumption ***A1b*** is mentioned on page 22. The absolute value of the sum of the two Fresnel coefficients is:

$$|S_R| \equiv |R_{\|} + R_{\perp}| \ll 1 \tag{7.4}$$

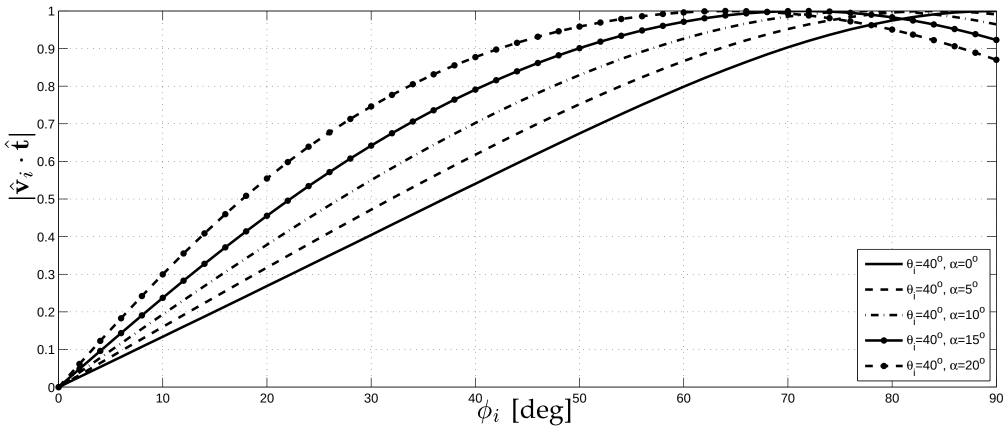

Fig. 7.2: In this graph, $|\hat{\mathbf{v}}_i \cdot \hat{\mathbf{t}}|$ is plotted against the incident azimuth ϕ_i for a fixed value of the incident latitude θ_i and some chosen values of the root-mean-square slope angle α. The value of $|\hat{\mathbf{v}}_i \cdot \hat{\mathbf{t}}|$ increases with the incident azimuth. Also, higher slopes give higher $|\hat{\mathbf{v}}_i \cdot \hat{\mathbf{t}}|$. The approximation $|\hat{\mathbf{v}}_i \cdot \hat{\mathbf{t}}| \ll 1$ works thus only for low values of ϕ_i and α.

and together with the formulas for $R_{\|,\perp}$ found in (6.17) and (6.18), the sum can be written as:

$$R_{\|} + R_{\perp} = \frac{2\epsilon_r\mu_r \cos\vartheta^2 - 2\sqrt{\epsilon_r - \sin\vartheta^2}\sqrt{\epsilon_r\mu_r - \sin\vartheta^2}}{\left(\mu_r \cos\vartheta + \sqrt{\epsilon_r - \sin\vartheta^2}\right)\left(\epsilon_r \cos\vartheta + \sqrt{\epsilon_r\mu_r - \sin\vartheta^2}\right)}. \tag{7.5}$$

Now using the definition of root-mean-square slope for a Gaussian surface ($\rho''(0) = \frac{2}{L^2}$):

$$\sigma_s = \sqrt{\sigma^2\rho''(0)} = \sqrt{2}\frac{\sigma}{L} \tag{7.6}$$

the mean slope angle can be found:

$$\langle\alpha\rangle = \tan^{-1}\sigma_s, \tag{7.7}$$

see Figure 6.1b. The mean angle of incidence is now:

$$\langle\vartheta\rangle = \theta_i - \langle\alpha\rangle = \theta_i - \tan^{-1}\left(\sqrt{2}\frac{\sigma}{L}\right) \tag{7.8}$$

which now gives us the sum of reflection coefficients as a function of the ratio $\frac{\sigma}{L}$.

In order to examine the behavior of $|S_R|$, a study of both ϵ_r- and θ_i-dependence is needed (μ_r is almost always 1 except for magnetic surfaces which are not of an interest here). First, it should be noticed that ϵ_r is of higher order in the denominator of (7.5) and thus lower values give higher $|S_R|$ (see Figure 7.3a and Figure 7.3b). Next, a plot of $|S_R|$ versus $\frac{\sigma}{L}$ is shown in Figure 7.3c for different angles θ_i. Usually, $\sigma < L$ and then $\frac{\sigma}{L} < 1$ and angles near grazing give high values of $|S_R|$. The same conclusions are published in Fung [22] and Álvarez-Pérez [33]. This simplification was lifted off by Wu et al., which led to more extensive computations but also more accurate results [14]. In that article, it is also mentioned that the inclusion of the terms with $R_{\|} + R_{\perp}$ gives more accurate results especially in bistatic directions ($\phi_s \neq 0°$).

7.3 Assumption A2 — Discrete Choice of Local Incidence Angle

In the first Integral Equation Model, the local incident angle ϑ used in the computation of Fresnel reflection coefficients was assumed to be either the specular angle or the global incident angle θ_i. This assumption can be found att page 23.

The first option is correct when a rather rough surface is examined. For a rough surface, scattering occurs in all directions and the only contribution in the direction of $\hat{\mathbf{k}}_s$ is from the parts of the surface that have their normals halfway between $-\hat{\mathbf{k}}_i$ and $\hat{\mathbf{k}}_s$, that is when

$$\hat{\mathbf{n}} = \frac{\hat{\mathbf{k}}_s - \hat{\mathbf{k}}_i}{|\hat{\mathbf{k}}_s - \hat{\mathbf{k}}_i|},$$

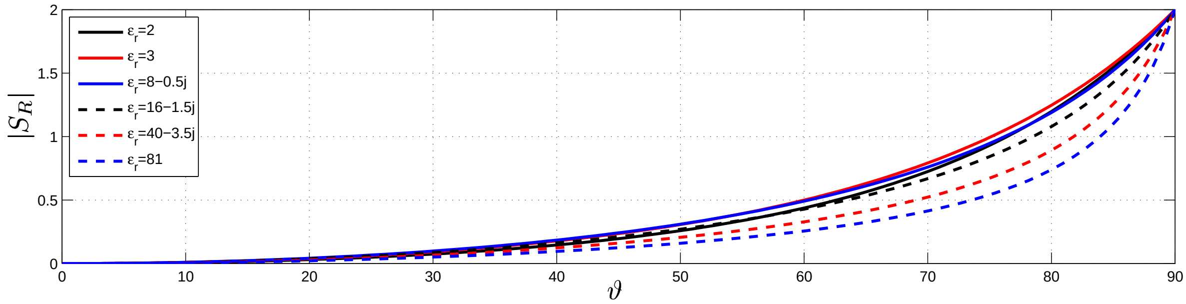

(a) $|R_{||} + R_{\perp}|$ for different ϑ and ϵ_r

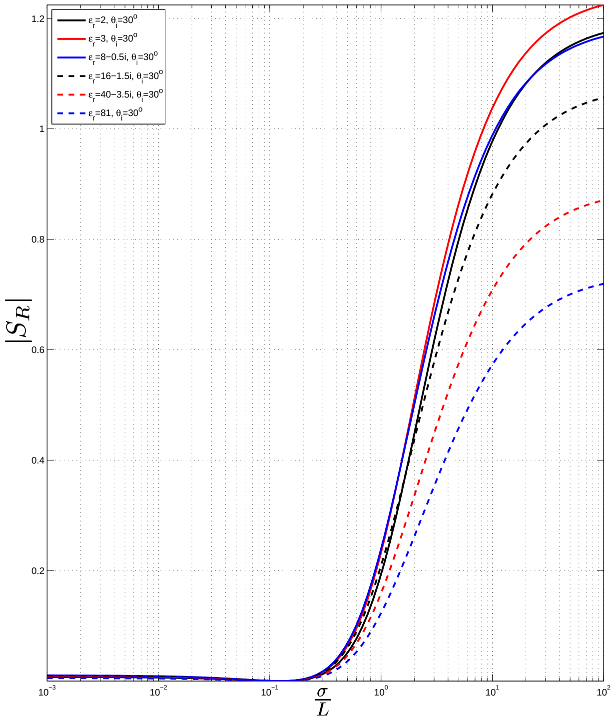

(b) Constant θ_i

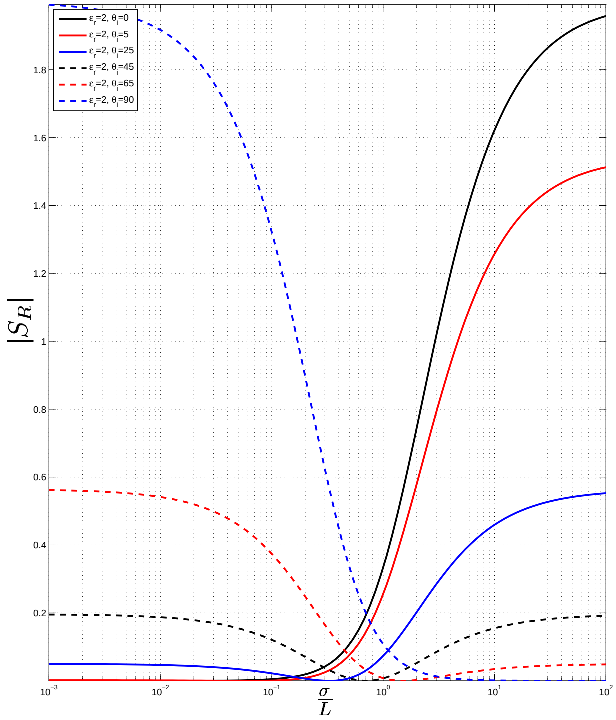

(c) Constant ϵ_r

Fig. 7.3: (a) $|S_R|$ plotted versus the local incidence angle ϑ. It can be clearly seen that $|S_R|$ increases with the local incidence angle. Higher relative permittivity ϵ_r generally gives lower value for $|S_R|$ except for grazing incidence where $|S_R| = 2$ for all values of ϵ_r. (b) $|S_R|$ plotted versus the ratio of σ to L after using expression (7.8) for the global incident angle θ_i equal to $30°$. The same results regarding ϵ_r-dependency can be drawn here as well. For $\frac{\sigma}{L} < 1$, the values of $|S_R|$ do not exceed 0.2. (c) Since low values for ϵ_r give highest $|S_R|$, $\epsilon_r = 2$ is chosen and $|S_R|$ is plotted for different incidence angles θ_i. For $\frac{\sigma}{L} < 1$, the values of $|S_R|$ become high for θ_i approaching grazing. For θ_i lower than approximately $45°$ the values of $|S_R|$ are negligible.

and the local incidence angle ϑ can be computed using

$$\vartheta = \cos^{-1}(\hat{\mathbf{k}}_i \cdot \hat{\mathbf{n}}). \tag{7.9}$$

The second option, that is $\vartheta = \theta_i$ is more correct in cases when correlation lengths are large. The surface can then be seen as locally flat and most scattering happens in the forward direction (the incoherent component is small).

An obvious problem is the choice of the roughness value for which one case goes into the other. This problem has been studied by among others Wu et al. who also derived the so-called transition function [13, 20, 34].

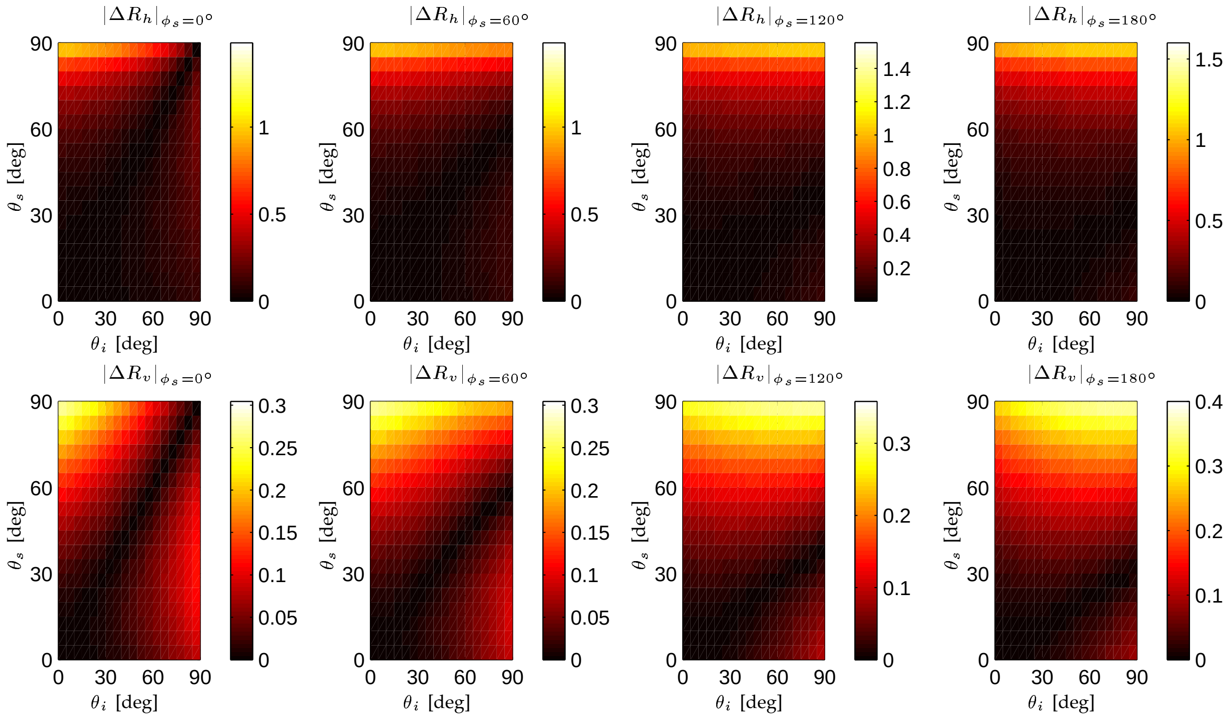

Fig. 7.4: Here, the difference between the Fresnel reflection coefficients computed from the incident angle and the specular angle (often referred to as $R_p(\theta_i)$ and $R_p(0)$, respectively) is plotted. In the upper row, $\Delta R_h = |R_h(0) - R_h(\theta_i)|$ is plotted while the lower row ΔR_v is shown. Four azimuth angles are chosen and each plot shows the dependence of ΔR_p of θ_i and θ_s. Light cells represent high ΔR_p and vice versa.

The difference in $R_{\perp,\parallel}$ between the two possibilities presented above is plotted in Figure 7.4 as a function of the three angles θ_i, θ_s, and ϕ_s. It can be clearly seen that the difference is greatest for R_h with θ_s close to 90°. For R_v, the difference is generally much lower, especially for small angles θ_i and θ_s, and for scattering at ϕ_0 when $\theta_i \approx \theta_s$.

7.4 Assumption A3 — Simplifications in the Green's Function

The spectral representation of Green's function as presented in (6.60) was:

$$\chi = -\frac{1}{2\pi} \int \frac{j}{q} \mathrm{e}^{ju(x-x')+jv(y-y')-\underline{jq|z-z'|}} \mathrm{d}u\mathrm{d}v \tag{7.10}$$

where $q = (k^2 - u^2 - z^2)^{1/2}$, and the gradient was:

$$\nabla\chi = -\frac{1}{2\pi} \int \frac{\mathbf{g}}{q} \mathrm{e}^{ju(x-x')+jv(y-y')-\underline{jq|z-z'|}} \mathrm{d}u\mathrm{d}v, \tag{7.11}$$

where

$$\mathbf{g} = \hat{\mathbf{x}}u + \hat{\mathbf{y}}v \pm \underline{\hat{\mathbf{z}}q}. \tag{7.12}$$

Recall from Section 6.7 that in the approximation used in IEM, all the underlined terms in (7.10)-(7.12) have been omitted, which was justified by the two following arguments:

- factor $jq|z-z'|$ is small if two points on a surface are close together and hence can be removed,
- factor $\pm q\hat{\mathbf{z}}$ can be removed due to the fact, that most of the factors with minus sign will cancel the factors with plus sign in the integral and thus the whole contribution will be zero.

This assumption affects only the complementary term and it is rather accurate in the case of single scattering. In multiple scattering, it has been shown quite early [31, 32] that the removal of the terms including q was not justified other than for backscattering and so the full Green function was implemented. In single scattering, this took longer

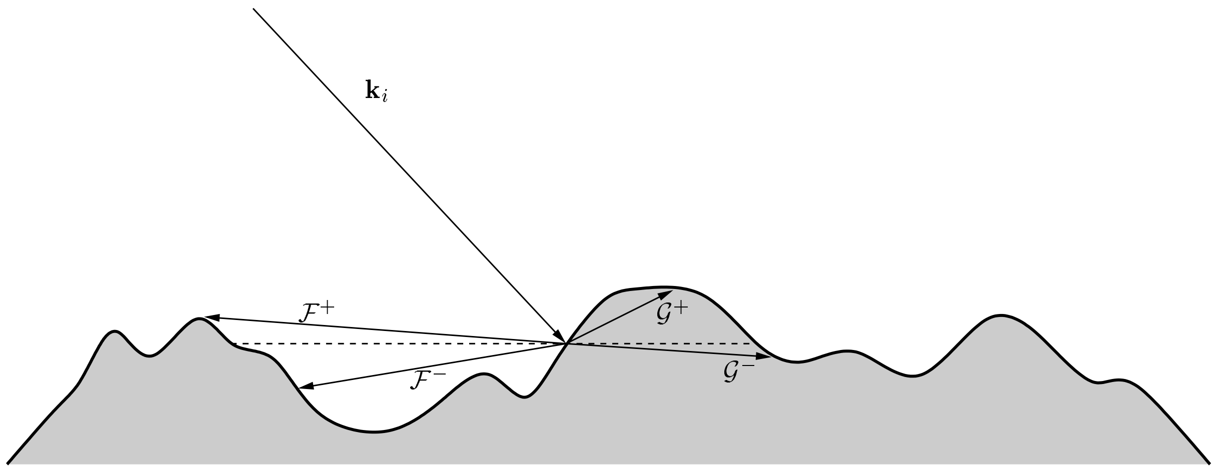

Fig. 7.5: Due to the fact that $jq|z-z'|$ can have four values depending on the direction and medium of propagation, the complementary field coefficients in Advanced Integral Equation Model are divided into four parts: $\mathcal{F}^+$ for upward propagation in medium 1, $\mathcal{F}^-$ for downward propagation in medium 1, $\mathcal{G}^+$ for upward propagation in medium 2, and $\mathcal{G}^-$ for downward propagation in medium 2.

time and it was first in Fung et al. [11] that the discussed simplification was removed.

By keeping the $jq|z-z'|$-term, one has to deal with two cases:

- when $z' > z$, $jq|z-z'| = -jq(z-z')$ (upward propagation),
- when $z' < z$, $jq|z-z'| = jq(z-z')$ (downward propagation),

so that the equation is now divided in two cases. Additionally, the value of q depends on the medium the wave crosses so that q can be either q_i or q_t with $q_{i,t} = \sqrt{k_{i,t}^2 - u^2 - v^2}$. In the complementary term, the waves of interest can travel in four ways (see Figure 7.5):

$\mathcal{F}^+$: upward through medium 1: $jq|z-z'| = -jq_i(z-z')$,
$\mathcal{F}^-$: downward through medium 1: $jq|z-z'| = jq_i(z-z')$,
$\mathcal{G}^+$: upward through medium 2: $jq|z-z'| = -jq_t(z-z')$,
$\mathcal{G}^-$: downward through medium 2: $jq|z-z'| = jq_t(z-z')$,

which now gives a total of four possible cases. In IIEM [11], only $\mathcal{F}^+$ and $\mathcal{F}^-$ are used since it is assumed that the field coefficients for medium 2 are small. In AIEM [12–14], all four cases are treated, which gives much more complicated expressions but also much more accurate results (for the explicit expression, see Appendix C.7).

The effects of this approximation are difficult to study separately. Generally, the change in assumption ***A3*** is the major difference between IEM, IIEM, and AIEM, and thus the general behavior can be studied by comparing the results produced by these methods in cases when approximations ***A1*** and ***A2*** are valid.

7.5 Summary of IEM Based Models

In the beginning of Section 6 and in Sections 7.1-7.4 it was mentioned how approximations have been gradually removed in different versions of the Integral Equation Model. Almost all the work on IEM has been done by the same research group lead by the creators of IEM, Fung et al. Some work has been done by other researchers, most notably Álvarez-Pérez [33], who was first with removing assumption ***A3*** in the single scattering case. For a brief summary, see Table 7.1.

Shadowing functions can be included in all functions and they have been used in IEM from the very beginning. More about them can be read in Sancer [35], Smith [36]. In Appendix D.2 two shadowing functions are presented.

The Advanced Integral Equation Model is the first model to use the so-called transition function, even though the function can be used in all models. For an explicit expression, see Appendix D.1. More about transition function can be found in Wu et al. [20], Fung and Chen [34].

TABLE 7.1: A short summary of the different versions of the Integral Equation Model.

Model:	**Source:**	**Description:**
IEM	Fung et al. [9], Fung [22]	***A1***, ***A2*** and ***A3*** present for both single and multiple scattering
IEMM	Hsieh and Fung [31], Hsieh et al. [32]	like IEM but ***A3*** removed in multiple scattering with $\mathcal{F}^{\pm}$ used only, shadowing function used
	Chen et al. [30]	like IEMM above but with slightly modified $\mathcal{F}^{\pm}$ in multiple scattering
IEM2M	Álvarez-Pérez [33]	like IEM but ***A3*** modified in single scattering for better agreement with SPM
IIEM	Fung et al. [11]	like IEM but ***A3*** removed in single scattering and $\mathcal{F}^{\pm}$ used, multiple scattering not included in the article, shadowing function used
AIEM	Chen et al. [12]	like IIEM for single scattering but with $\mathcal{F}^{\pm}$ and $\mathcal{G}^{\pm}$ used, multiple scattering not included in the article
	Wu and Chen [13]	like IIEM for single scattering and IEMM for multiple scattering, both with $\mathcal{F}^{\pm}$ and $\mathcal{G}^{\pm}$ used, ***A2*** removed by transition function
	Wu et al. [14]	like IIEM for single scattering with both $\mathcal{F}^{\pm}$ and $\mathcal{G}^{\pm}$ used, ***A1*** removed, ***A2*** removed by transition function, multiple scattering not included in the article

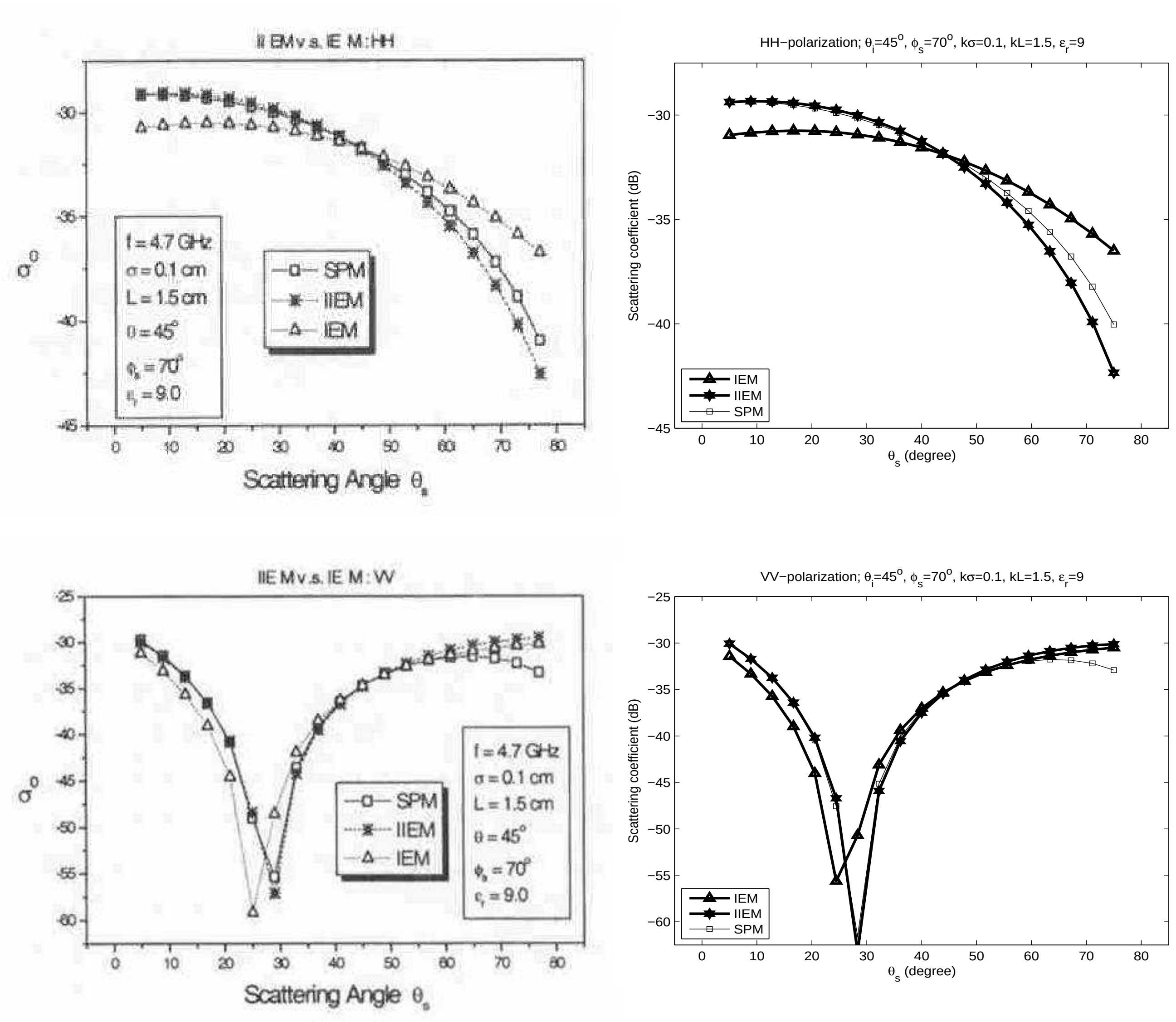

Fig. 8.1: The scattering coefficients for HH (upper row) and VV (bottom row), computed by the models implemented for this project (right), are compared with corresponding results found in Fung et al. [11] (left). The results agree very well in the SPM-region (roughness parameters are $kL = 1.5$ and $k\sigma = 0.1$). The other parameters are: $\epsilon_r = 9.0$, $\theta_i = 45°$, and $\phi_s = 70°$.

8 Verification and Validation of the Models

After the models have been implemented in Matlab®, they have been tested against published results. In Fung et al. [11], the authors present figures in which IIEM is tested against KM, SPM, and IEM. In Wu et al. [14], AIEM is also included and there are more cases presented. The verification process was mainly done by comparison with the results published in those two articles. Also, the models were tested against other articles [9, 13, 20, 27] with very good results. These results are however not presented in this text.

8.1 Comparison with Fung et al. [11]

First, a comparison with Fung et al. [11] was done in order to confirm that IIEM was correctly implemented. SPM, GO, and IEM implemented by the author as presented in Appendix C were used together with an implementation of IIEM provided by Gustafsson [37]. In this section, two figures will be presented side-by-side with each other: reference figure to the left, and a figure resulting from simulations using the implemented models to the right.

In Figure 8.1, one can see the results for simulations in the SPM region ($kL = 1.5$, $k\sigma = 0.1$) with $\epsilon_r = 9.0$, $\theta_i = 45°$, and $\phi_s = 70°$. The agreement is very good. In VV-mode, one can clearly see a dip at the approximate

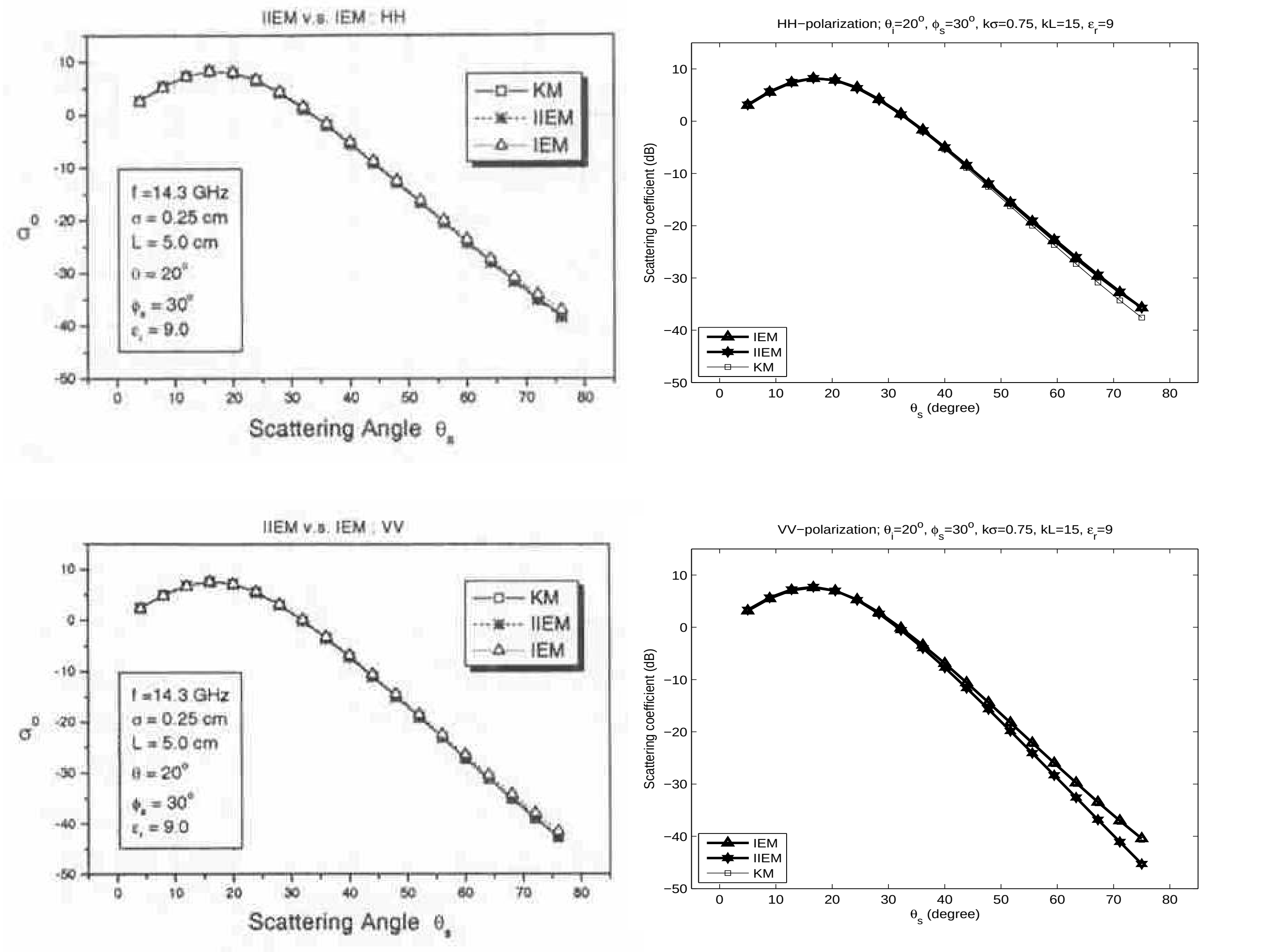

Fig. 8.2: In the PO-region, a comparison with the reference (left) shows that IIEM agrees slightly better than IEM and KM but in overall, the scattering coefficient agrees fairly well (the current setup is: $kL = 15$, $k\sigma = 0.75$, $\epsilon_r = 9.0$, $\theta_i = 20°$, and $\phi_s = 30°$.

position of the Brewster angle.

In Figure 8.2, one can see results from a case in the region where Physical Optics model is valid. The agreement is generally good except for large angles θ_s. In the case presented in this figure, $kL = 15$ and $k\sigma = 0.75$, which is a rather extreme case of a very smooth surface. IIEM agrees very well with the reference while IEM and KM show some minor deviations.

8.2 Comparison with Wu et al. [14]

In Wu et al. [14], the authors test the Advanced Integral Equation Model (AIEM) against PO, GO, and SPM. Moreover, Wu et al. also include IEM and IIEM in their evaluation. The scattering coefficients were thus computed for the same cases as those presented in Wu et al. [14], and the plots were compared. Multiple scattering was not implemented in any of the models. Since the chosen roughness parameters were slightly outside validity regions for both PO and GO, both methods were tested while reproducing the results from Wu et al. [14], and the one that had the best agreement in each figure was kept and simply called KM. Due to lack of space in this report, the original figures published in Wu et al. [14] will not be shown in this text as it was done in the previous section.

8.2.1 Scattered Elevation Angle Dependancy

Small Perturbation Region

In Figure 8.4, the scattering coefficient is plotted as a function of the scattered elevation angle θ_s for three dielectric permittivities: $9.0 - 0.5j$, $16 - 1.5j$, and $40 - 3.0j$. The other parameters are kept constant: $kL = 1.5$, $k\sigma = 0.1$, $\phi_s = 30°$, and $\theta_i = 30°$. The roughness parameters indicate that Small Perturbation Model can be used. It can be clearly seen that the scattering coefficient decreases as the scattering angle increases and it also increases with a higher dielectric permittivity. The same observation can be made in Figure 8.5, in which $\theta_i = 45°$ while all other parameters are the same as in Figure 8.4. Both figures are in excellent agreement with Wu et al. [14, Figure 3 and 4].

Figure 8.6 shows scattering in the plane of incidence ($\phi_s = 0°$ or $\phi_s = 180°$) at incident angles $30°$ and $60°$. The surface parameters are $\epsilon_r = 12 - 1.8j$, $kL = 1.5$, and $k\sigma = 0.1$, which is still in the validity region for SPM. One can see that lines for the different methods all go through the point where $\theta_s = \theta_i$, which means that they all agree in the case of forward and backward scattering. Otherwise, the curves show the same tendencies as in the previous paragraph. All curves in Figure 8.6 agree very well with Wu et al. [14, Figure 3 and 4].

Kirchhoff Region
Figure 8.7 shows some results in the region where Kirchhoff approximation is valid. Roughness parameters are set to $kL = 7.5$ and $k\sigma = 2.8$ while electric permittivity is switched between $12 - 1.8j$ and $40 - 3j$. First, the scattering coefficients are plotted as a function of θ_s for $\theta_i = 30°$ and $\phi_s = 30°$. According to the graphs, the scattering coefficient for HH-polarization do not change much for different θ_s while it decreases with increasing angle for VV-polarization. As expected, higher ϵ_r gives higher scattering in all directions (less energy is transmitted through the surface). Higher incident angle ($\theta_i = 45°$) gives slightly lower scattering coefficient but the main trends are the same. Compared to corresponding figures in reference material [14, Figure 7 and 8], all the graphs look almost the same, with a reservation for high θ_s-angles, where the scattering coefficient is too low for HH-polarization and too high for VV-polarization (the difference is around 2 dB).

The last results, see Figure 8.8, concern incident plane behavior for the integral equation-based models in the Kirchhoff region. The surface parameters are the same as in the previous paragraph and ϵ_r is chosen to be $12 - 1.8j$. The incident angle is chosen to be $\theta_i = 30°$ and ϕ_s is switched between $0°$ and $180°$. Also, there is a slight disagreement with Wu et al. [14, Figure 9 and 10] in the region where θ_s is high.

8.2.2 Azimuthal Behavior

In Figure 8.9, the surface parameters were: $\epsilon_r = 16$, $kL = 7.5$, and $k\sigma = 2.8$ and both HH and VV polarization modes were plotted. The angles were chosen to be $\theta_i = 30°$ and $\theta_s = 50°$ in the first case, $\theta_i = 45°$ and $\theta_s = 45°$ in the second case, and $\theta_i = 50°$ and $\theta_s = 30°$ in the third case. Since the surface is rather smooth, Kirchhoff Model is used as a reference. One can see that the curves are maximal in the backscatter and forward scattering direction and they gradually fall to a dip around $75°$. For this surface roughness and for models that do not include multiple scattering, major part of scattering occurs in the incident plane in the coherent way without much depolarization. As ϕ_s increases, the field is still measured for the same polarization but for $\phi_i > 0°$, the field along the measured polarization vector decreases since it is just a projection of the field in the plane of incidence. In comparison with Wu et al. [14, Figure 2], the results shown in Figure 8.9 differ in the position of the dips in all six figures. The most prominent difference, however, is the lack of change in the dip position in Figure 8.9 between HH and VV. In Wu et al. [14, Figure 2], that change is around $10°$.

In Figure 8.10, the scattering coefficients were plotted as a function of azimuth for two elevation angle combinations — $\theta_i = 30°$ and $\theta_s = 60°$ in the first case in Wu et al. [14, Figure 11], and $\theta_i = 60°$ and $\theta_s = 30°$ in the second case [14, Figure 12]. kL was set to 9.42 in both cases while $k\sigma$ was switched between 1.73 and 5.12. The relative dielectric permittivity was set to 3.0. The results remind a lot of the results from the previous paragraph. First, one can see that for the rougher surface, the scattering coefficient in backward direction is almost equal to that in forward direction. For the smoother surface, forward scattering is less prominent compared to backscattering. The location of the dips is also different compared to reference. Moreover, in Wu et al. [14, Figures 11 and 12], the dips change with around $30°$ between HH and VV while in Figure 8.10 this change is not present. Finally, IIEM differs a lot from the other methods just like in Figure 8.9, but it still agrees well with the reference.

The change of dip position is a possible explanation for the disagreement that occurred earlier in elevation angle studies in the Kirchhoff region. For $\phi_s = 30°$, the disagreement became higher when θ_s increased. Looking at Figure 8.3, one can see that for the constant value of ϕ_s and increasing θ_s, the examined direciton moves closer to the direction of the dip. Since there is a slight disagreement in the dip position between Figures 8.9-8.10 and the reference figures, moving closer to the dip results in higher uncertainty in the results. The possible reasons for the dip position disagreement will be discussed in Section 10.

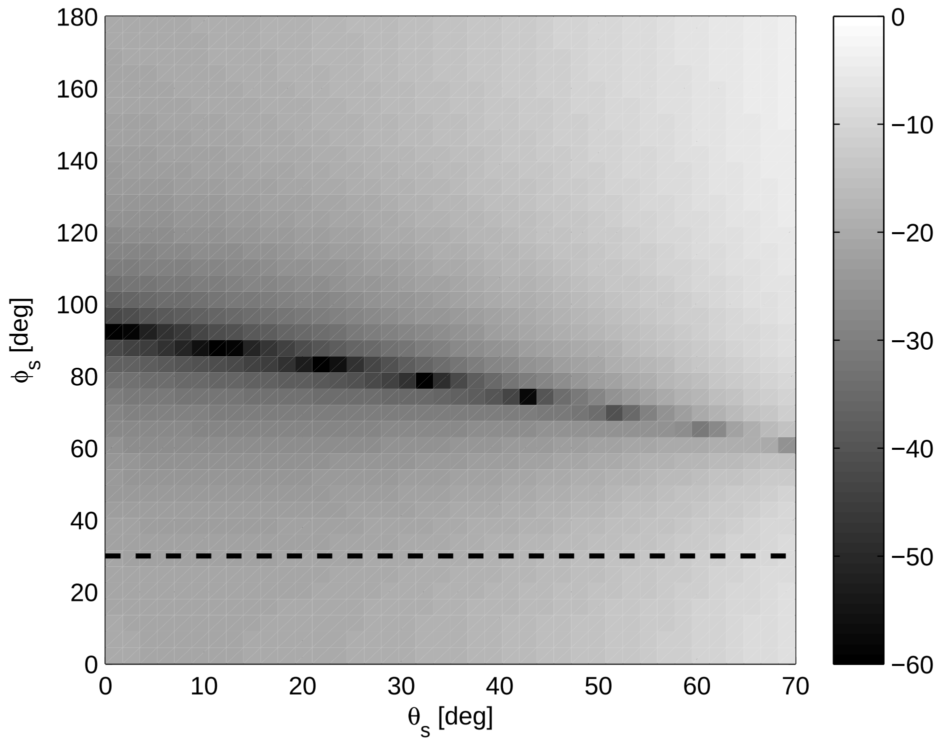

Fig. 8.3: The scattering coefficient for AIEM and HH is here plotted as a function of both θ_s and ϕ_s for the same surface as in Figure 8.7. The dashed line corresponds to $\phi_s = 30°$. As θ_s increases, the dashed line and the dip come closer to each other. Since there is a slight disagreement in dip position between Figures 8.9-8.10 and corresponding figures in the reference article, there will also be a slight disagreement in the other figures especially for azimuth angles close to the dip.

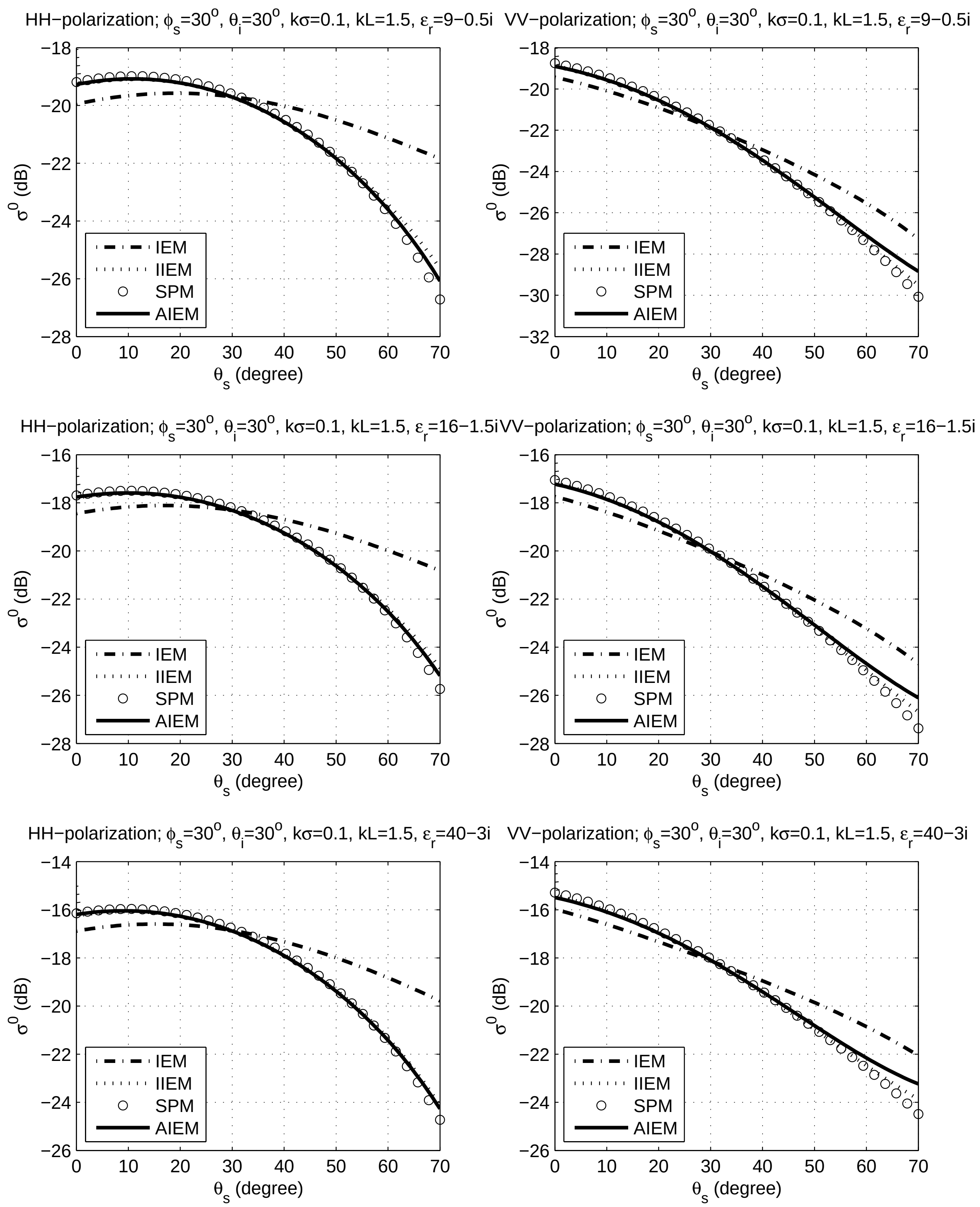

Fig. 8.4: Results for cases found in Wu et al. [14, Figure 3]. The agreement with Wu et al. [14] is perfect for all models.

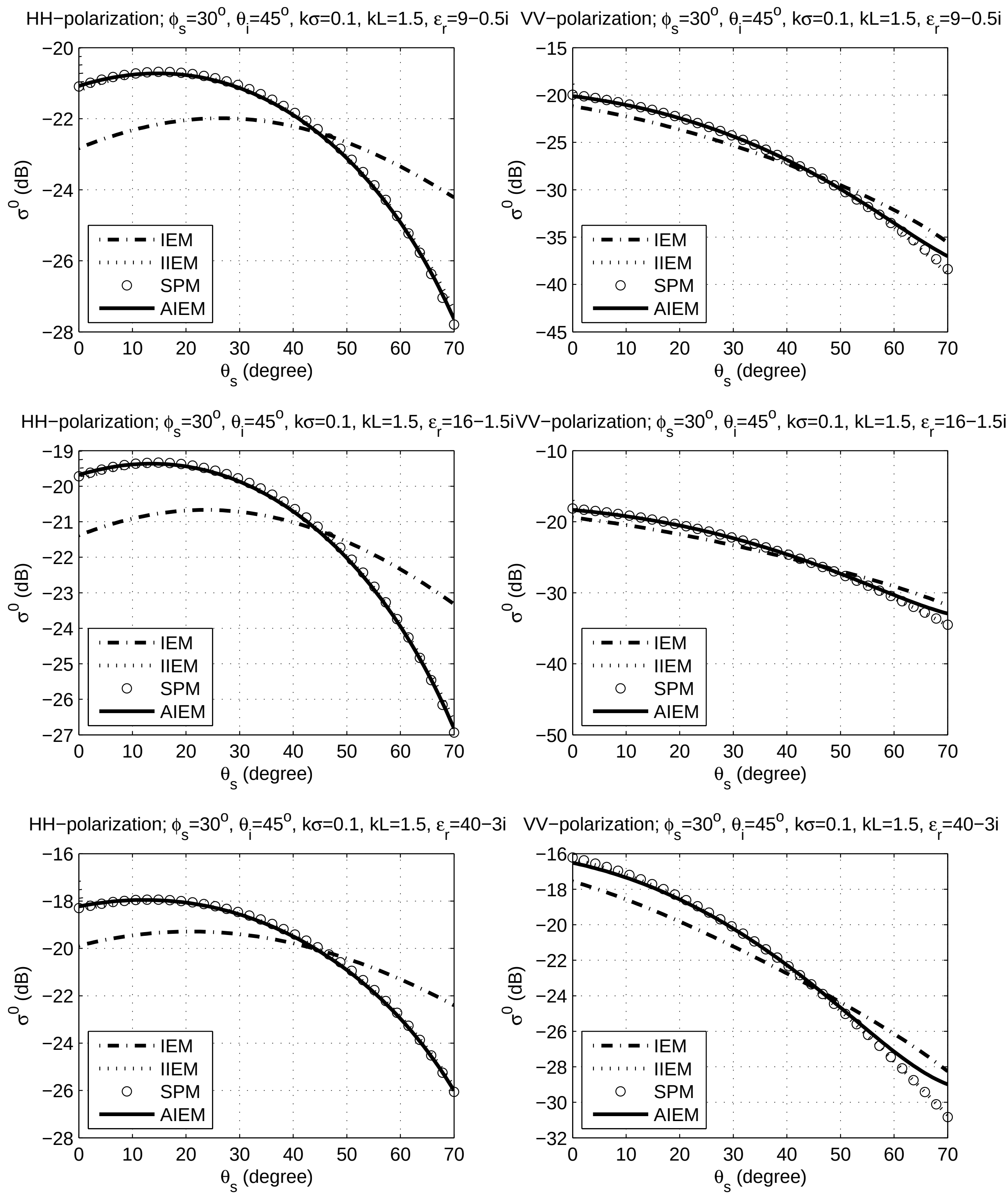

Fig. 8.5: Results for cases found in Wu et al. [14, Figure 4]. The agreement with Wu et al. [14] is excellent.

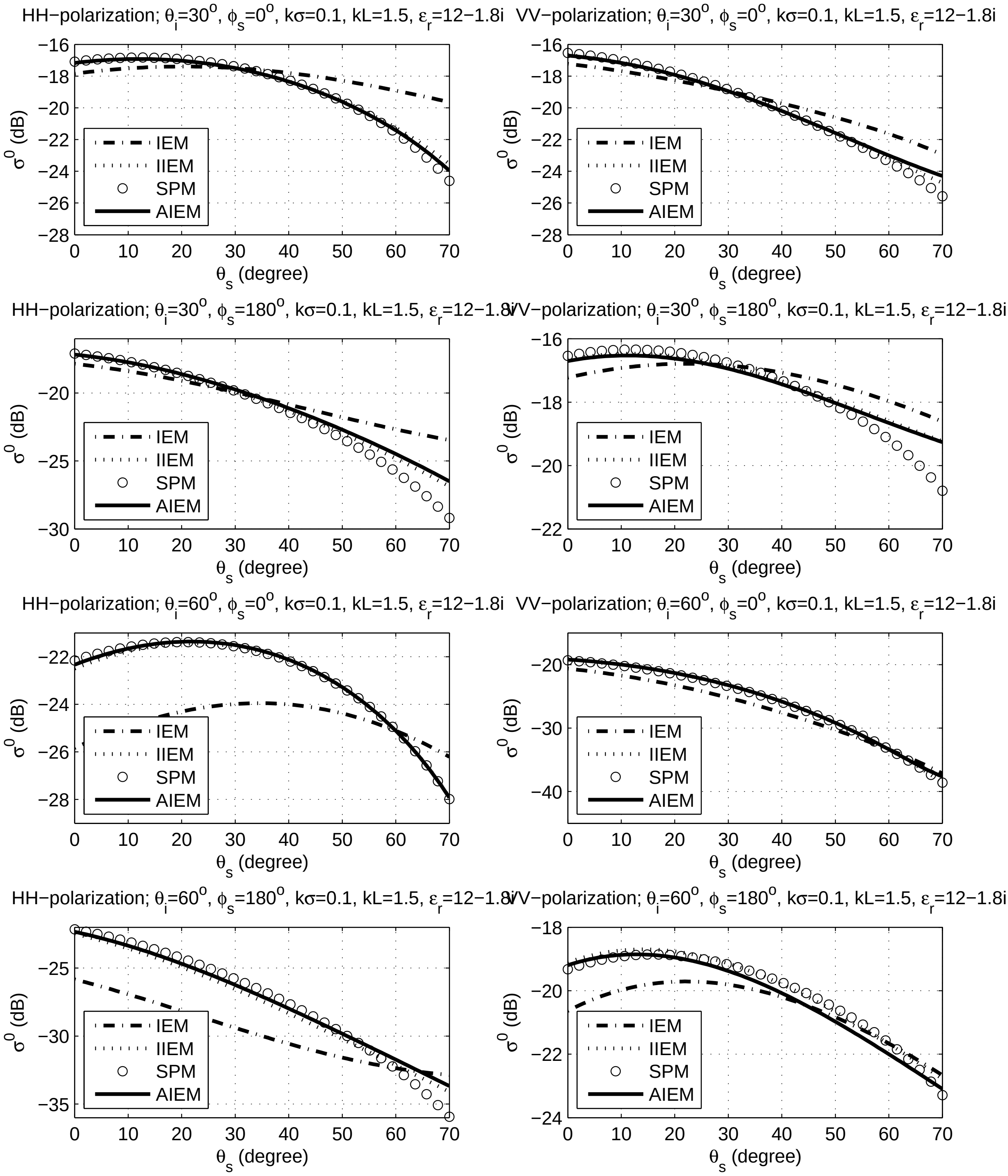

Fig. 8.6: Scattering coefficients for cases found in Wu et al. [14, Figures 5 and 6] are shown. In this figure, just like in Figures 8.4-8.5, the agreement with the reference is also perfect which gives the conclusion that SPM, IEM, and AIEM were implemented correctly by the author (at least in those terms that are important in the SPM-validity region). IIEM also shows good agreement with the reference article.

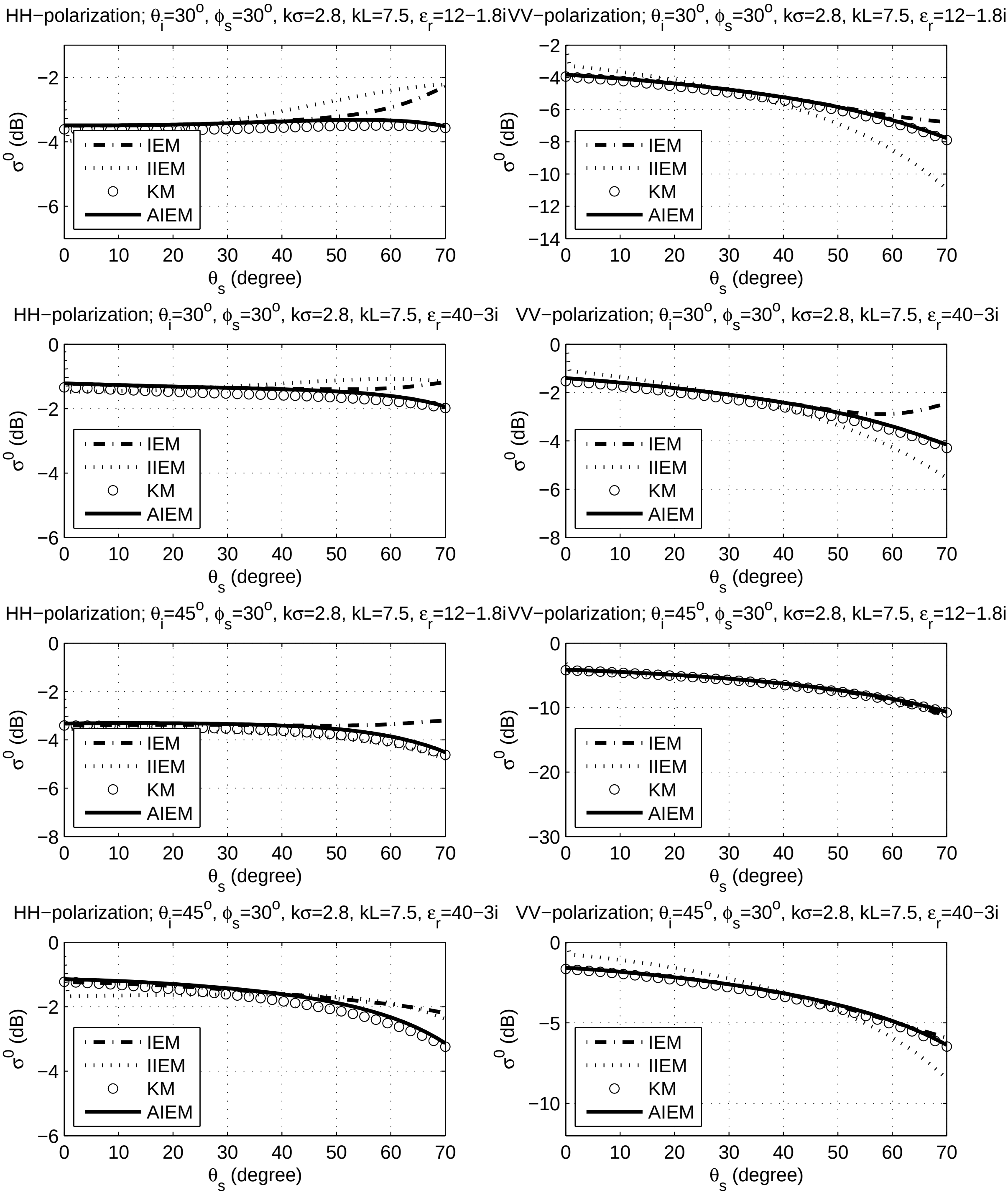

Fig. 8.7: Results for cases found in Wu et al. [14, Figures 7 and 8]. For HH-polarization, a slight underestimation of σ^0 is observed for high values of θ_s for all models. For VV-mode, an overestimation is observed instead. The difference is at most 2dB. The form of the curves is otherwise very close to the form of the graphs in Wu et al. [14]. The small deviations can be explained by the results observed in Figures 8.9-8.10.

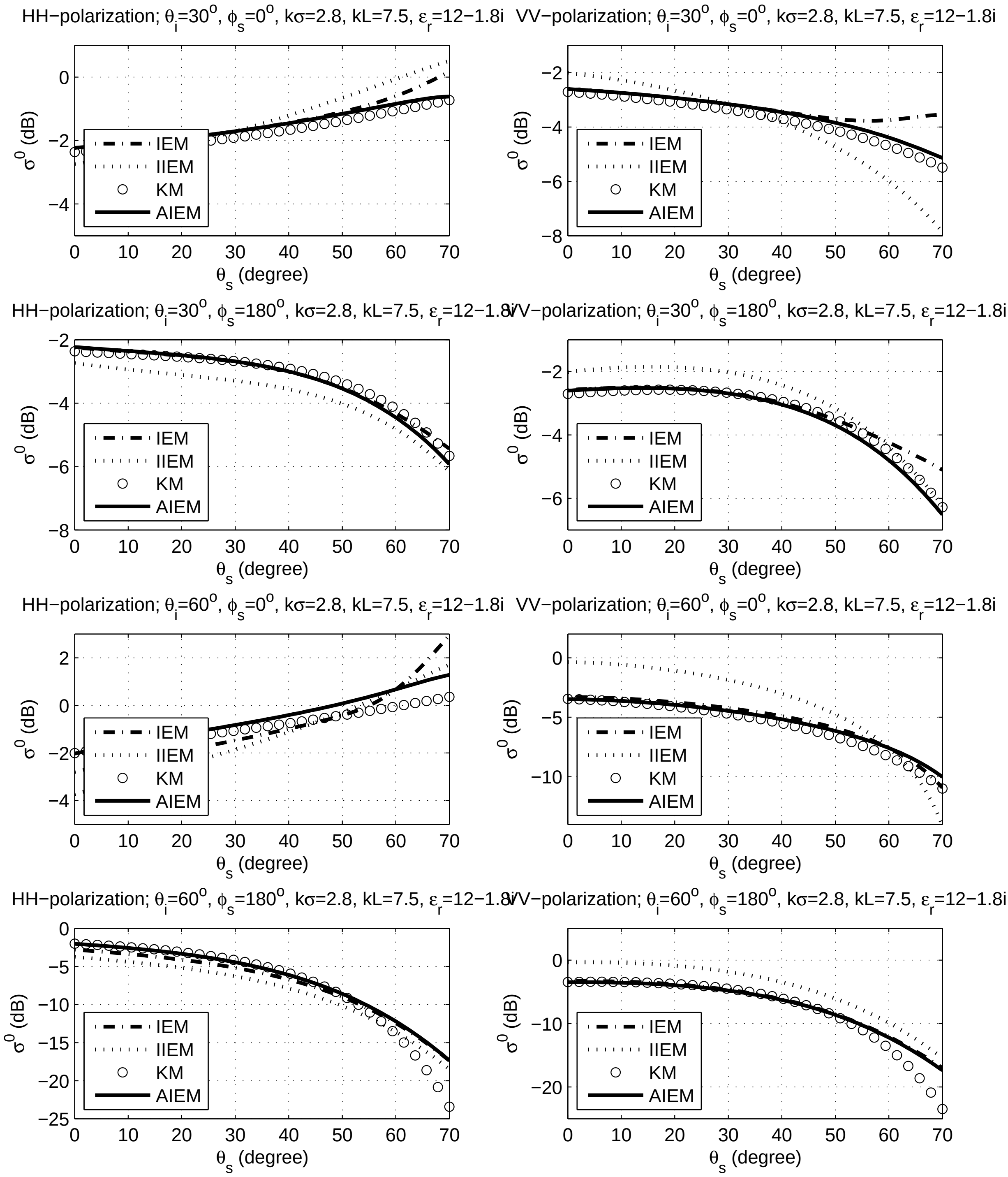

Fig. 8.8: Results for cases found in Wu et al. [14, Figures 9 and 10]. Scattering coefficients for high angles θ_s are slightly overestimated for VV and underestimated for HH just like in Figure 8.7.

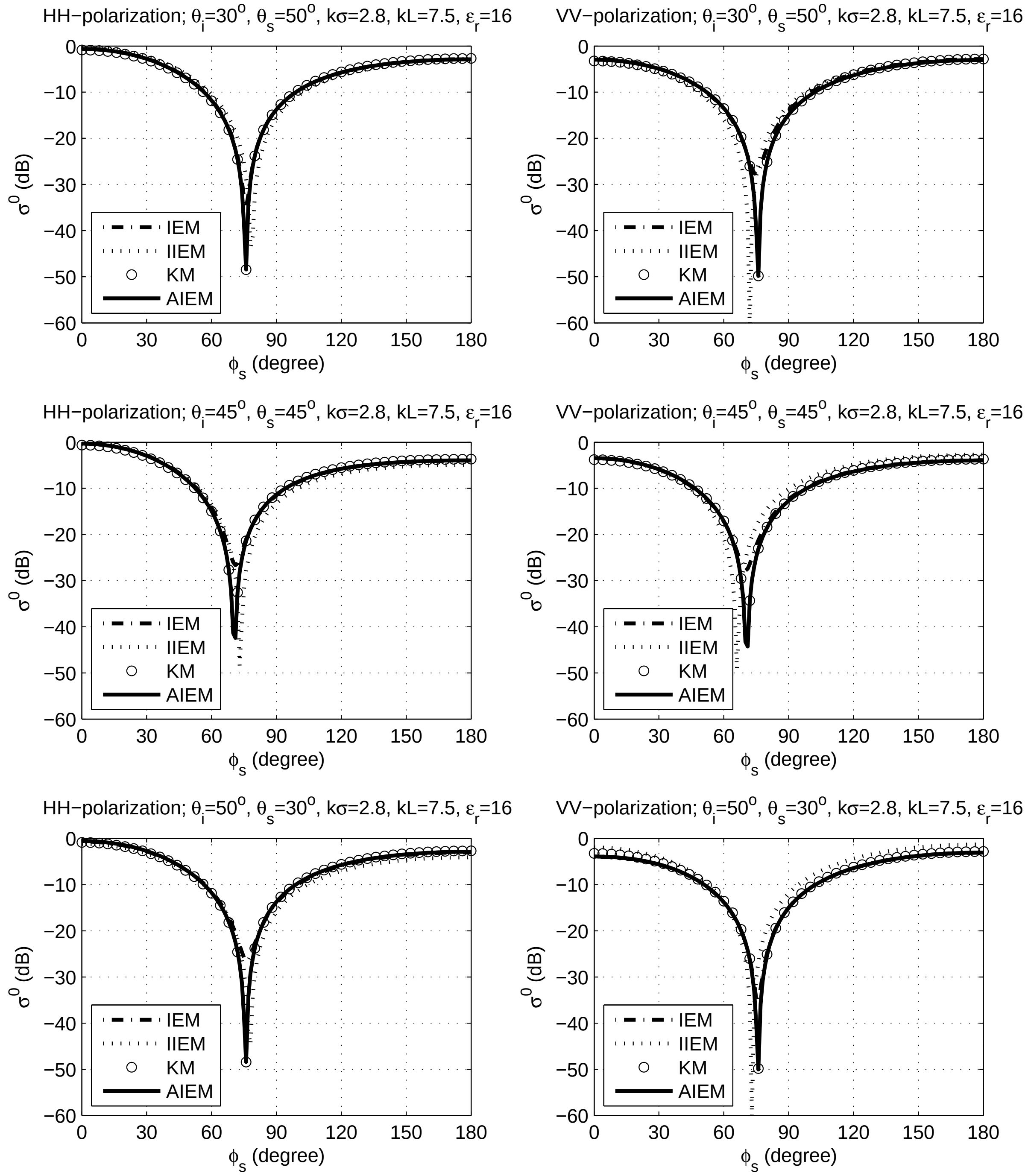

Fig. 8.9: Results for cases found in Wu et al. [14, Figure 2]. Compared to the original, figures above do not show a change in the location of the dip between HH and VV for KM, IEM, and AIEM as they do in the reference. The relative displacement of IIEM has a correct direction but once again, the position of the dip is different. Values of σ^0 for $\phi_s = 0°$ and $\phi_s = 180°$ are the same as in the reference. The relative change between different angle setups do also agree with the relative changes in the reference.

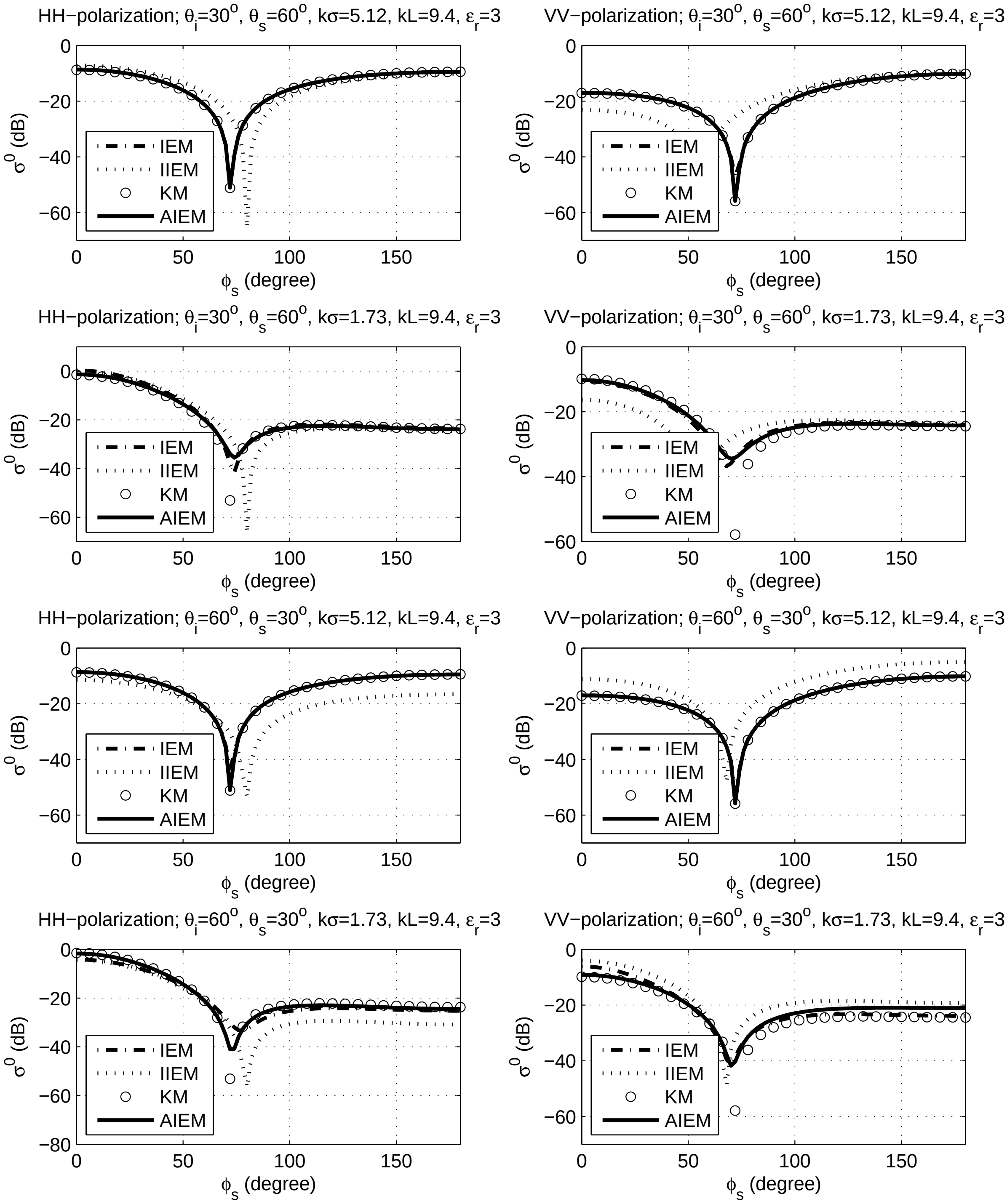

Fig. 8.10: Results for cases found in Wu et al. [14, Figures 11 and 12]. Also here, the position of the dip is the same for HH and VV, which does not agree with Wu et al. [14]. The difference here is however much bigger than in Figure 8.9. Otherwise, the differences are just the same as in Figure 8.9. IIEM shows good general behavior but the exact position of the dip is also shifted.

8.3 Root Mean Square Testing of Model Validity

Here, the implemented methods were tested against each other in order to see in which regions they agree best. This was done in the following way:

1) a uniformly distributed random set of $N = 400$ angle combinations was created using Matlab® function `rand` and the angles were chosen from the following intervals:
$$\theta_i \in [5°, 75°],\ \theta_s \in [-75°, 75°],\ \phi_s \in [0°, 180°], \text{ and } \phi_i = 0°,$$
2) $n_L = 20$ and $n_\sigma = 15$ equally spaced values for kL and $k\sigma$, respectively, were chosen from the intervals $[0.1, 10]$ and $[0.01, 5]$,
3) five different σ^0-values were computed for all angles, all kL-$k\sigma$-combinations, and all polarization modes, for each one of the models: PO, GO, SPM, IEM, and AIEM,
4) root mean square deviations between IEM, AIEM, PO, GO, and SPM were computed:
$$RMSD_{m,r}(kL, k\sigma) = \sqrt{\frac{1}{N}\sum_{n=1}^{N}\left[\sigma_m^0(kL, k\sigma) - \sigma_r^0(kL, k\sigma)\right]^2}, \tag{8.1}$$
where σ_m^0 comes from either IEM or AIEM and σ_r^0 from either GO, PO, or SPM (σ_0 is in linear units and so is the resulting $RMSD_{m,r}$),
5) the resulting averages over all polarization modes were plotted in decibels for Gaussian correlation function in Figure 8.11a and for exponential correlation in 8.11b.

The number of angle combinations was chosen as a compromise between computation time and accuracy. No improvement in result quality was found when the number of angle combinations was increased but computation time became much longer. Averaging over all four polarization modes was done since no specific differences were noticed in the different polarization modes.

First, one can see that for both Gaussian and exponential correlation functions, SPM and IEM/AIEM agree very well in the region where kL and $k\sigma$ are low. AIEM and IEM agrees very well with both PO and GO for all kL and $k\sigma$ which should not be a surprise due to the fact that IEM is a method based on the Kirchhoff Approximation but with more terms included.

Comparing Figure 8.11 with Figure 5.1, one can see that there are some regions that overlap (mostly for SPM, but also for GO with the Gaussian correlation function). It is important to note that regions of low RMSD in Figure 8.11 do not show the same thing as the validity regions do in Figure 5.1. RMSD-plots only show places where IEM/AIEM agrees with the asymptotic methods and do not say anything about agreement with real-life, measured data (as they do in Figure 5.1).

For the exponential correlation function, the agreement is generally slightly worse than for the Gaussian function. Root-mean-square deviation between IEM and AIEM is slightly higher for both Kirchhoff models. One can also see that for both correlation functions and both Kirchhoff based methods, there is a surprisingly good agreement in for high $k\sigma$ and low kL. This is a typical example of a region where both methods agree but none is valid.

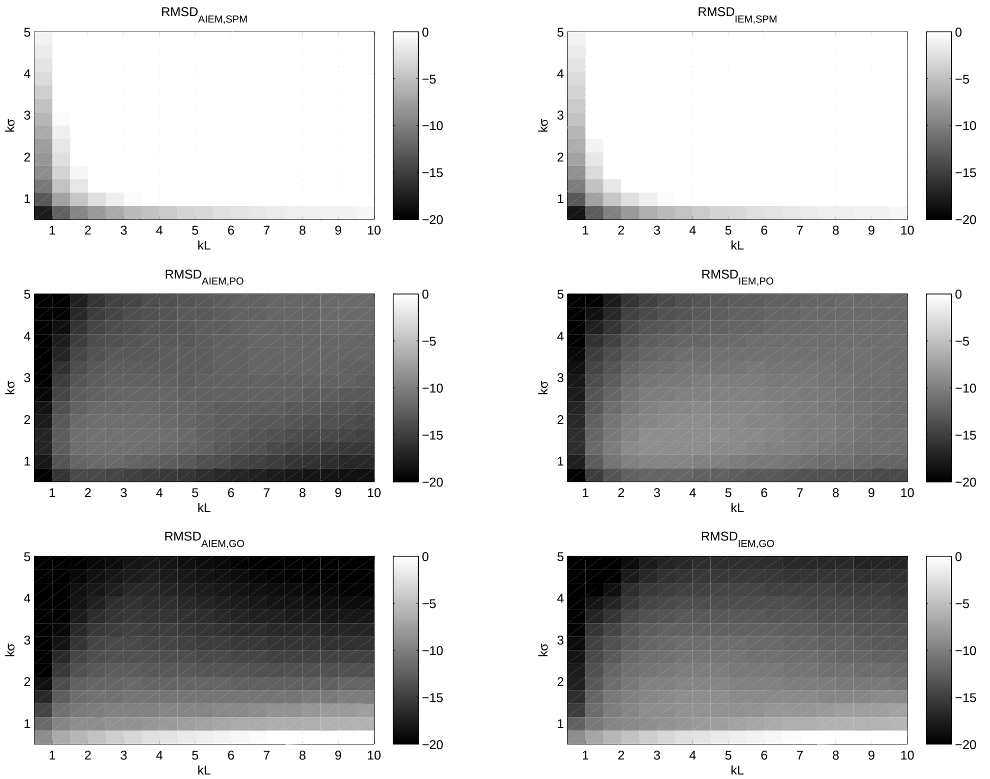

(a) RMSD in decibel for Gaussian correlation function. The values are clipped below -20 dB and above 0 dB for better viewing.

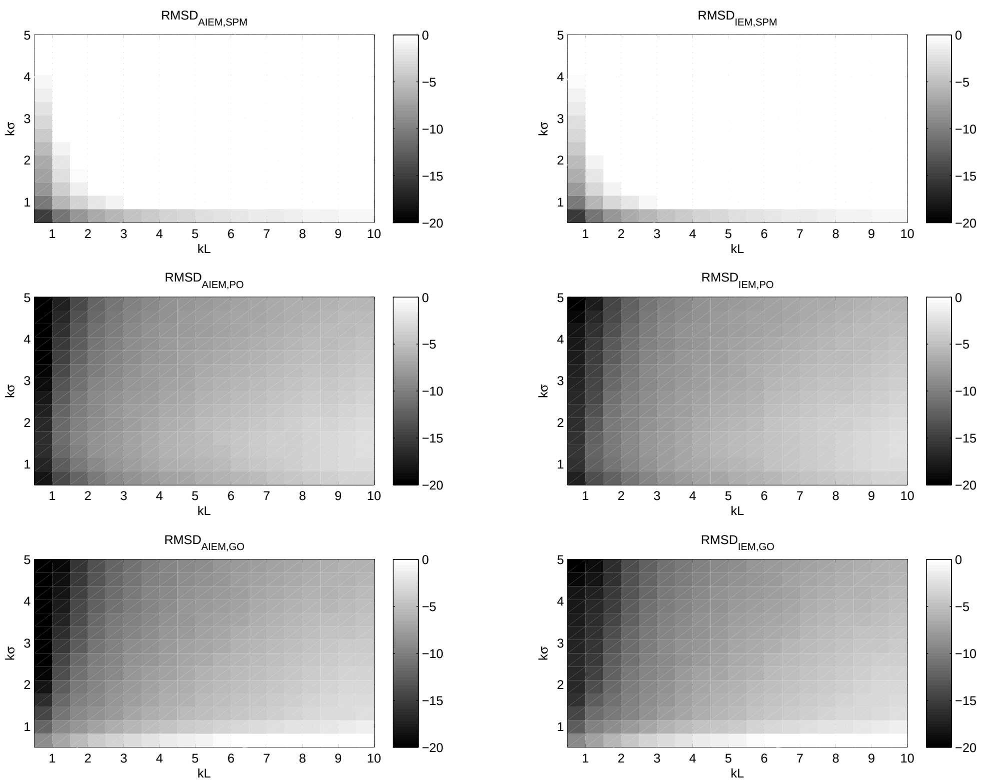

(b) RMSD in decibel for exponential correlation function. The values are clipped below -20 dB and above 0 dB for better viewing.

Fig. 8.11: RMSD plot for Gaussian and exponential correlation functions. The intensity value is equal to the RMSD in dB between two modelled scattering coefficients. The results are averages of HH, VV, HV, and VH for each function. AIEM has slightly better agreement with GO in the region of high kL and $k\sigma$ and with PO for high kL and low $k\sigma$ region. Note: for better viewing, the values below -20 dB and above 0 dB are shown as -20 dB and 0 dB, respectively.

8.4 Angular Dependency

An interesting question that arises after looking at the graphs presented in Section 8.2 is how the scattering coefficients depend on the position of measurement (θ_s and ϕ_s) and what is the angular distribution of the scattering coefficients. This can be examined by doing an AIEM simulation for different angles and looking at $\sigma^0_{dB}(\theta_s, \phi_s)$-plots for different θ_i settings for a particular surface. In the following section, a comparison between AIEM and PO/SPM will be done in the corresponding validity regions. The relative electric permittivity has been set to $\epsilon_r = 16$. Two settings of surface roughness are chosen as well: $kL = 1.5$, $k\sigma = 0.1$ for SPM validity, and $kL = 7.5$, $k\sigma = 2.8$ for Physical Optics validity (which is slightly outside the validity regions described in Figure 5.1, but the results from Wu et al. [14] are obtained for the same parameters with good results). The incident angle θ_i was switched between $40°$, $65°$, and $80°$.

For each setting, two plots were created for both HH- and VV-mode (see Figure 8.14):

- a two-dimensional image with ϕ_s on the x-axis and θ_s on the y-axis (the y-axis was flipped upside-down in order to create a more intuitive plot). The intensity in each point was:

$$\widetilde{\sigma}^0_{dB} = \frac{\sigma^0_{dB} - \min(\sigma^0_{dB})}{\max(\sigma^0_{dB}) - \min(\sigma^0_{dB})},$$

  which is a scaled and normalized version of σ^0_{dB} ($\widetilde{\sigma}^0_{dB}$ lies in the interval $[0, 1]$; this plot will from now on be referred to as "2D-image" or simply "image"),
- a three-dimensional surface that shows the angular distribution of the scattering coefficient. Spherical coordinates for each point $(\widetilde{\sigma}^0_{dB}, \phi_s, \theta_s)$ have to be transformed into Cartesian coordinates:

$$x = \widetilde{\sigma}^0_{dB} \sin\theta_s \cos\phi_s, \tag{8.2}$$
$$y = \widetilde{\sigma}^0_{dB} \sin\theta_s \sin\phi_s, \tag{8.3}$$
$$z = \widetilde{\sigma}^0_{dB} \cos\theta_s. \tag{8.4}$$

  This plot will be referred to as "3D-surface" or simply "surface".

Both graphs actually show the same results but in quite a different way. The 3D-surface is better for studying the angular distribution qualitatively, to discern the lobes, and to examine how the point of zero scattering (the dip) changes for different angle setups. The 2D-image is better when it comes to more quantitative analysis and comparison between models, angle settings, and modes.

Looking at Figure 8.14, one can see that the difference between the position of the dips between HH and VV polarizations for AIEM for all three angles is small or non-existent. This result was already observed in Section 8.2 but the reason is unknown (Wu et al. [14] shows a noticeable difference in this position). For Physical Optics, the difference is more obvious especially for high θ_s.

For surfaces that have long correlation length, scattering is most prominent in the specular direction. One mechanism that affects the position of the dip is the fact that, for angles ϕ_s greater than zero, the measured field with a particular polarization consists of the projection of the specularly scattered field in the direction of the measurement. This explains the result for normal incidence. The location of the dip is then naturally at $90°$ for all models and polarizations. Additionally, when looking at all four polarizations, one can see that cross-polarization tops when co-polarization is the lowest, see Figure 8.12. When the azimuthal angle is increased, the co-polarized scattered field decreases because its projection becomes smaller.

In the 2D-image, three lines have been plotted. These are the contours for regions that have intensities of 99%, 95% and 80% of the maximal achieved intensity. The maximal intensity can be found for angles close to $0°$ and $180°$ (that is if the scattering is measured in the plane of incidence). An interesting result is that even though the dips are at the same positions for both HH and VV, the regions of maximal scattering (regions surrounded by the red line that represents 99% of maximal intensity) are situated in different places, both for AIEM and PO. While in HH-mode scattering is most prominent in a direction close to specular direction (although not exactly specular — some unexplained variations may be found), in VV mode, most scattering seems to occur in the normal direction.

In the region where SPM is valid, AIEM was plotted in the same way against SPM in Figure 8.15. One can clearly see looking at the 3D-surfaces that for HH, scattering occurs almost isotropically with an exception for the region around $\phi_s = 90°$, where the scattering coefficient drops in a dip. The dip in HH-mode is however very shallow for the SPM.

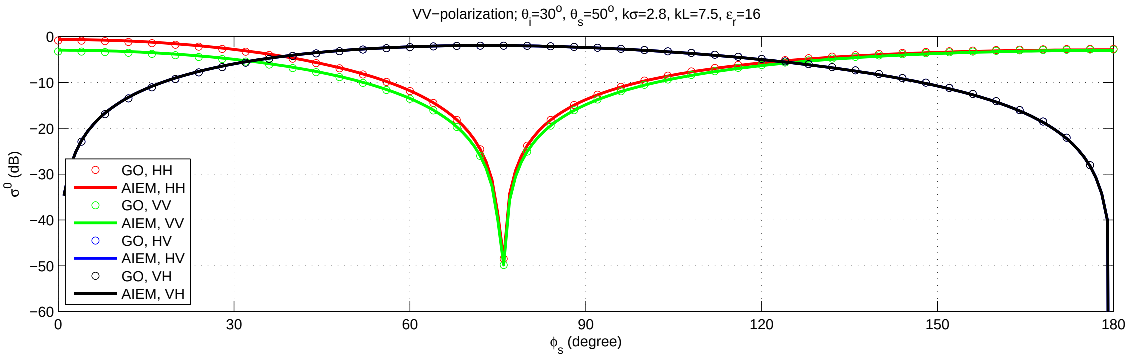

Fig. 8.12: The location of a dip in co-polarization coincides with the maximum of the scattering coefficient for cross-polarization when azimuthal dependance is studied. This confirms that an increment in the azimuthal angle decreases the scattered partly due to geometrical effects (the distribution between polarizations changes). Note that the curves for HV and VH overlap.

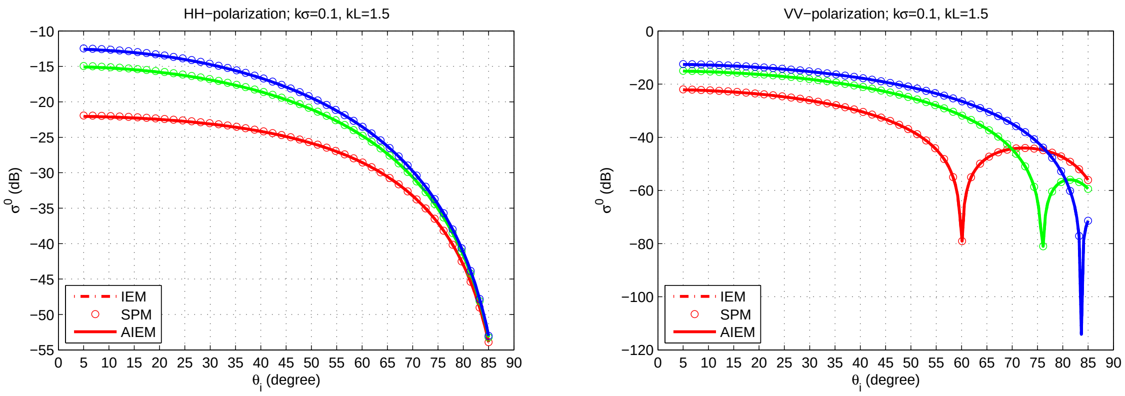

Fig. 8.13: In this figure, forward scattering is examined. The three curves in HH and VV correspond to $\epsilon_r = 3$ (red), $\epsilon_r = 16$ (green), and $\epsilon_r = 81$ (blue). If the incidence occurs at the Brewster angle, then no vertically polarized field is reflected. As it can be seen in the figure, the dip in VV occurs exactly at the expected location for both SPM, IEM, and AIEM (the Brewster angles can be computed from $\theta_B = \tan^{-1}\sqrt{\epsilon_r}$). This shows that all three models handle Brewster angle correctly.

The origin of the dip in the SPM-region may be the so-called Brewster angle. Brewster angle is the angle at which vertical polarization is not reflected at all. In IEM-based methods, the value of ϑ in the expression for the Fresnel coefficient is chosen to be half the angle between the incident and scattered direction. If $\phi_s = 0°$ and the sum of the incident and the scattered angle $\theta_i + \theta_s$ is equal to twice the Brewster angle $\theta_B = \tan^{-1}\sqrt{\epsilon_r}$, then dip should occur in VV. If the azimuth is increased, then the dip occurs for lower angles θ_s if θ_i is kept constant. Higher incident angle θ_i gives slower rate of change of the location of the dip. Looking at Figure 8.13, one can see that the effect of Brewster angle is simulated properly by the three methods SPM, IEM, and AIEM.

The location of the maximal-intensity regions in the 2D-image are slightly different for surfaces with short correlation lengths and small standard deviations. Most prominent scattering still occurs in the plane of incidence but the regions show much higher values than in the case shown in Figure 8.14. The region of 99% intensity for HH shifts towards $45°$ as θ_i goes towards $90°$ for AIEM while in SPM, it cannot be told whether that happens or not because the 99%-region is much larger and SPM-simulated scattering is thus much closer to isotropic. For VV-mode, most of the scattering is still in the normal, or close-to-normal direction.

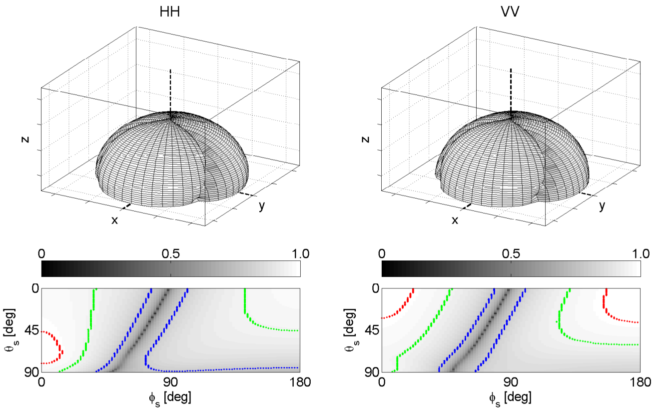

(a) Advanced Integral Equation Model, $\theta_i = 40°$

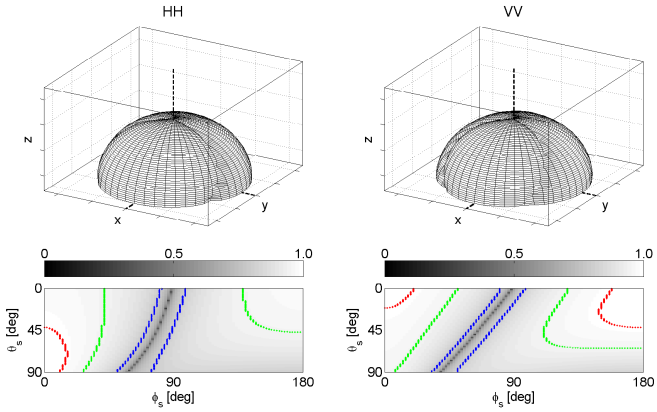

(b) Physical Optics Model, $\theta_i = 40°$

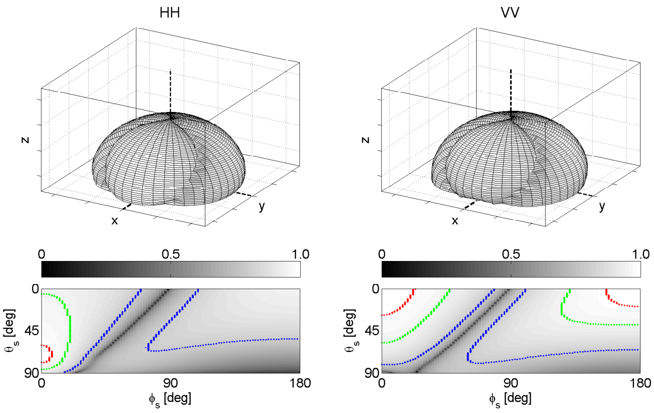

(c) Advanced Integral Equation Model, $\theta_i = 65°$

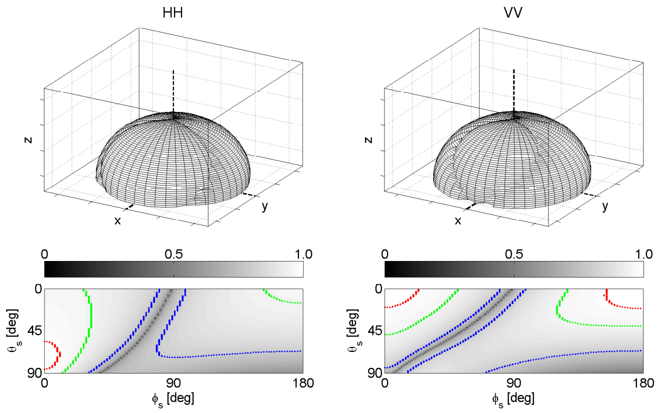

(d) Physical Optics Model, $\theta_i = 65°$

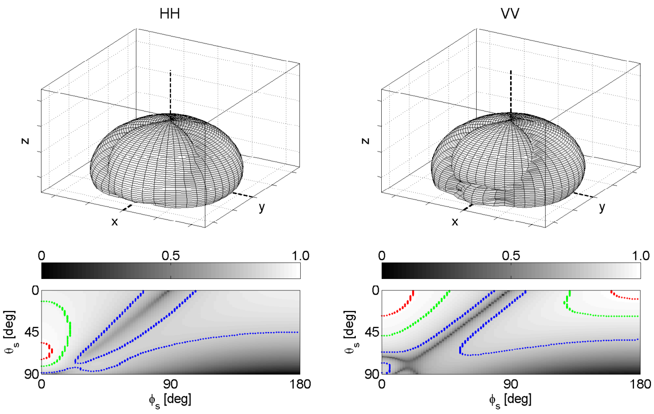

(e) Advanced Integral Equation Model, $\theta_i = 80°$

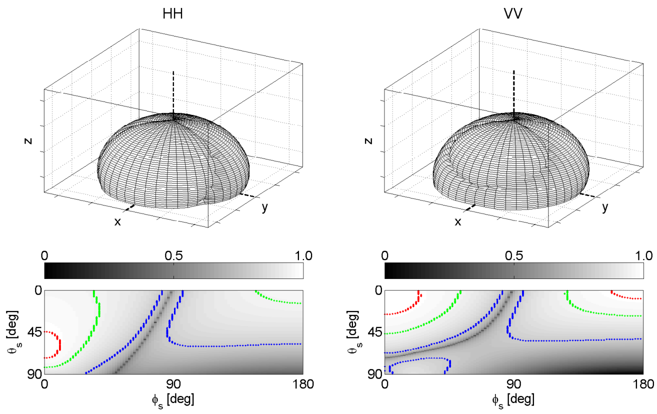

(f) Physical Optics Model, $\theta_i = 80°$

Fig. 8.14: Relative scattering coefficient for three angles θ_i from a rough Gaussian surface with $k\sigma = 2.8$ and $kL = 7.5$ using Advanced Integral Equation Model and Physical Optics Model. The three curves — red, green and blue — are contours for regions of 99%, 95% and 80% of the maximal scattering coefficient. Permittivity is set to $\epsilon_r = 16$.

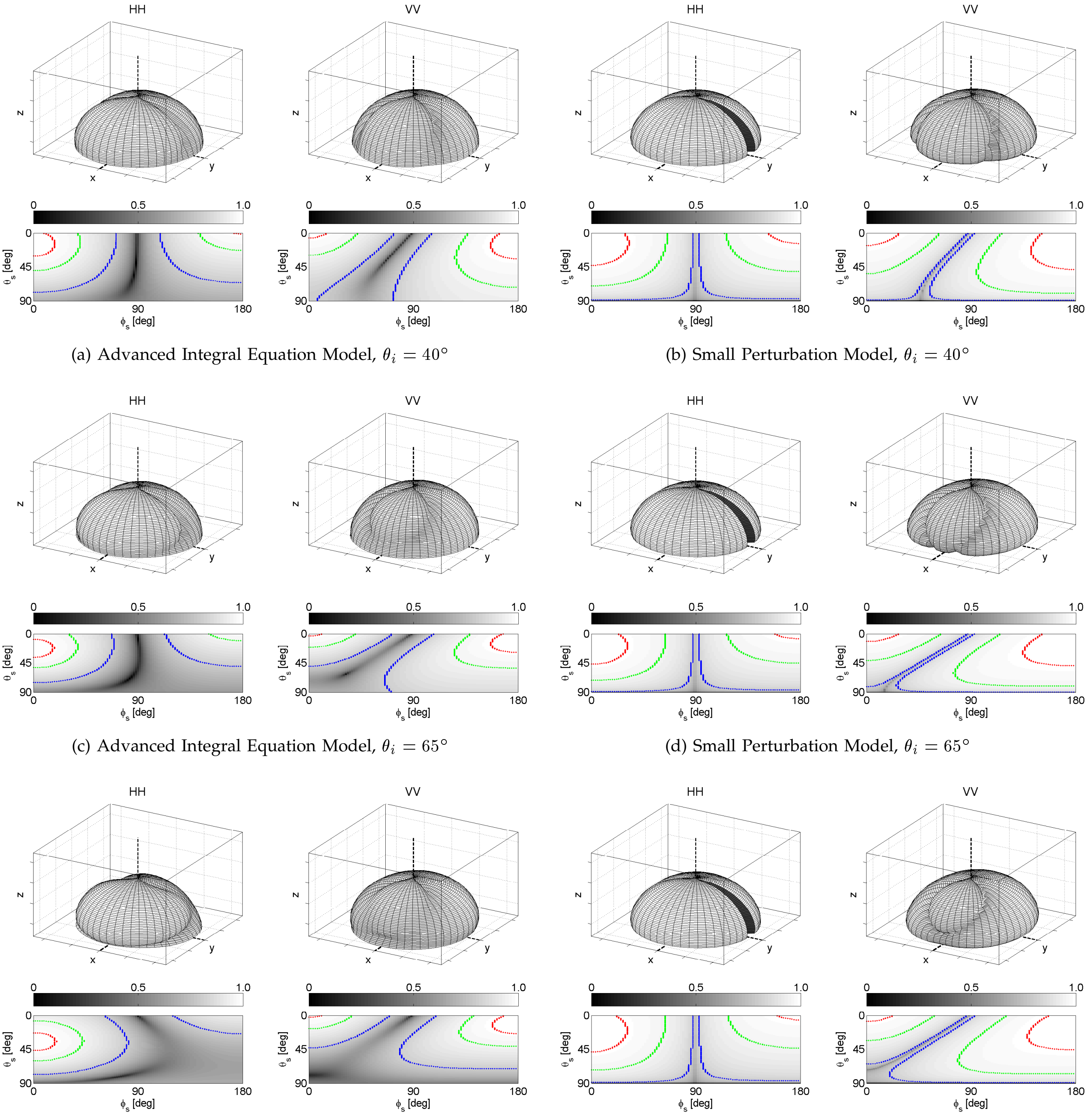

(a) Advanced Integral Equation Model, $\theta_i = 40°$

(b) Small Perturbation Model, $\theta_i = 40°$

(c) Advanced Integral Equation Model, $\theta_i = 65°$

(d) Small Perturbation Model, $\theta_i = 65°$

(e) Advanced Integral Equation Model, $\theta_i = 80°$

(f) Small Perturbation Model, $\theta_i = 80°$

Fig. 8.15: Relative scattering coefficient for three angles θ_i from a rough Gaussian surface with $k\sigma = 0.1$ and $kL = 1.5$ using Advanced Integral Equation Model and Small Perturbation Model. The three curves — red, green and blue — are contours for regions of 99%, 95% and 80% of the maximal scattering coefficient.

9 SURFACE STUDY

The main scope of this project is to study the behavior of scattering coefficients when surface structure changes. In order to do that, a number of tests has been set up. First, $k\sigma$ was kept constant and kL was swept through a wide range of values in four regions — GO, PO, SPM, and joint PO/SPM validity regions — for both forward ($\theta_s = \theta_i$, $\phi_s = 0°$), backward ($\theta_s = \theta_i$, $\phi_s = 180°$), and general bistatic scattering (no particular restriction on angles). Thereafter, kL was kept constant and $k\sigma$ was swept over a wide range of values in two regions — Kirchhoff validity region (joint PO and GO) and SPM validity region. Tests were done for both forward, backward, and bistatic scattering.

9.1 Constant Standard Deviation

The first test was performed in each region of validity for the asymptotic methods. The normalized standard deviation of the surface was set to a constant value and kL was swept over a wide range. Figure 9.1 shows an overview of the values for $k\sigma$ and kL used in this section. The lower limit for GO varies for different angular setups and in the cases when more than one angular setup was used, only the most strict restriction is shown in Figure 9.1. The colors of the marks in Figure 9.1a correspond to the colors of the curves in Figures 9.2-9.5 and the colors of the marks in Figure 9.1b correspond to the colors of the curves in Figures 9.6-9.7.

9.1.1 Forward and Backward Scattering

For simulations in the plane of incidence, the following four angle setups were used: $\theta_i = 40°$ or $\theta_i = 50°$, $\theta_s = \theta_i$, and $\phi_s = 0°$ or $\phi_s = 180°$. The relative dielectric permittivity used was $16 - 1.5j$.

Geometrical Optics Region
In the region where Geometrical Optics Model is valid, the following values of $k\sigma$ were used: 3.0, 5.0, 7.0, and 9.0. kL was swept for each value within the validity region up to 14.5 (see Figure 9.1a).

The scattering coefficient increases for decreasing $k\sigma$ in forward scattering, see Figure 9.2. This, together with the opposite trend in backscattering (lower two graphs) confirms the fact, that increasing $k\sigma$ gives more backscatter but less forward scatter in the Kirchhoff region. Moreover, a higher incident angle (closer to grazing) results in a slightly lower forward scattering but also in larger backscattering for HH-polarization while the trend is opposite for VV-polarization.

Another trend that can be observed in Figure 9.2 is that scattering coefficient increases with kL for forward scattering while it decreases for backward scattering, especially for rather low $k\sigma$ (around 3). This can also be understood quite intuitively — larger correlation lengths give larger facets and more energy can be scattered forward. The opposite relation for backscattering is also natural — more backscattering occurs when surfaces change faster. It can be seen that for backscattering (especially for $\theta_i = 50°$) that the highest $k\sigma$ gives the highest backscattering. This can be explained by the fact, that high $k\sigma$ gives a high mean slope of a surface. Higher surface slope means greater chance that the incidence will be normal to the tangential plane thus giving very high backscattering. Observing how the curves for different values of $k\sigma$ change, one can see that there must be a $k\sigma$ in between 5 and 7 for which the curve stops going upward and starts going downward. This happens only for $\theta_i = 40°$.

Physical Optics Region
The results of this simulation are presented in Figure 9.3. Standard deviation $k\sigma$ has been set to 0.8, 1.3, and 1.8 in order to fulfill the $\sqrt{2}\frac{\sigma}{L} < 0.25$-condition for Physical Optics and ϵ_r was still $16 - 1.5j$. Within this region, almost the same results are observed as for Geometrical Optics. In forward scattering, σ^0 increases with increasing kL and decreasing $k\sigma$ and it is higher for HH than for VV in all cases. One can also see that the scattering coefficient for $k\sigma = 0.8$ is generally lower for $\theta_i = 50°$ than for $\theta_i = 40°$ which does not happen for the other values of $k\sigma$. The uneven spacing between curves shows that there is a non-linear dependance on $k\sigma$ in that region.

For backscattering, the general results are also quite the same as for Geometrical Optics region apart from the fact, that the spacing between curves is much more even. For all curves, the three models agree perfectly except for high kL and low $k\sigma$ for $\theta_i = 50°$ where the Advanced Integral Equation Model shows higher values than both IEM and PO (see the four plots in the bottom part of Figure 9.3). The same observation can also be made in Figure 9.2, but then also for IEM.

Small Perturbation Region
Since the small perturbation region is rather small, only two $k\sigma$ were tested — 0.05 and 0.2. Forward and backscattering coefficient are generally lower than the corresponding ones for both Kirchhoff models (see Figure 9.4 compared to Figure 9.2 and 9.3). This is due to the fact, that for small height variations of the surface, scattering is much more evenly distributed in azimuth (much closer to isotropic) than for the Kirchhoff region. It should thus be expected to give higher scattering coefficient values in the bistatic mode (more about that later). Moreover, one can see that higher $k\sigma$ gives higher σ^0 — rougher surfaces give more forward scattering.

For backscattering (two last rows in Figure 9.4), one can see that higher $k\sigma$ also gives a higher scattering coefficient, which together with the conclusions from forward scattering is difficult to explain intuitively. One possible explanation is that higher surface deviation may give more bistatic scattering than low surface deviation values. There is also a maximal σ^0 that can be acquired for all values for kL. For backscattering, AIEM gives an overestimation for the HH-polarized scattering coefficient and an underestimation for VV-polarization compared to SPM while IEM agrees perfectly. One more observation that can be made here is that backscattering in SPM-region is the only case when HH gives lower scattering than VV.

In Ulaby et al. [4], the validity region for SPM theoretically also includes the region for high kL. Thorsos [23] shows that the validity of SPM is limited for $k\sigma > 2$ due to a disagreement with numerical simulations. In order to evaluate that, some tests were also made in the region where $kL > 2\pi$ and $k\sigma < 0.3$. In that region, Physical Optics is usually the valid asymptotic model and the results were thus compared with PO. All parameters were set just like in the previous paragraph with an exception for kL, which now was swept from 2π to 15. The results are plotted in Figure 9.5. In forward scattering, SPM, PO, IEM, and AIEM agree very well, while in backscattering, SPM gives extremely low, unrealistic values of σ^0, which shows that SPM is not a suitable modeling method in this region. Higher $k\sigma$ gives more forward and backscattering, just like the previous results showed. Higher kL gives also more forward scattering but less backscattering. Forward scattering is stronger in HH-mode than in VV-mode.

9.1.2 Bistatic Scattering

In bistatic scattering, two angle setups were used. The first setup was: $\theta_i = 45°$, $\theta_s = 45°$, $\phi_s = 30°$, and the second one was: $\theta_i = 30°$, $\theta_s = 50°$, $\phi_s = 30°$. The dielectric permittivity was set to $16 - 1.5j$ throughout all tests. The values for kL and $k\sigma$ used in the tests are shown in Figure 9.1b.

Geometrical Optics Region
In the region where Geometrical Optics Model is valid, the agreement between GO, IEM, and AIEM is perfect (see Figure 9.6). For both angle setups and both polarization modes, the general trend is that σ^0 increases with increasing kL and also is higher for lower $k\sigma$ and it is higher for HH than VV. There is a small difference between the two angle setups ($\theta_i = 30°$ gives slightly higher σ^0). This difference decreases with $k\sigma$ for HH but increases with $k\sigma$ for VV. The used values for $k\sigma$ were: 5.0, 7.0, and 9.0.

Physical Optics Region
In the region of Physical Optics validity, scattering coefficients decrease with an increasing correlation length and also, they are higher for higher $k\sigma$, see Figure 9.6. This is an opposite result compared to Geometrical Optics model and a conclusion is that there is a maximal value of σ^0 somewhere in between validity regions for both PO and GO. The different models agree with each other farily well. The difference between the two angular setups is rather small. The used values for $k\sigma$ were: 0.8, 1.3, and 1.8.

Small Perturbation Region
In the region where SPM can be used, the behavior of σ^0 for different values of kL and $k\sigma$ is generally the same for bistatic scattering as for forward and backward scattering, as in Figure 9.7 compared to Figure 9.4. This result could be predicted since scattering is much closer to isotropic for surfaces with short correlation length. Also here, the three used methods agree very well, and the difference between the two angular setups is small. The used values for $k\sigma$ were: 0.05 and 0.2.

Finally, in the region of $kL > 2\pi$ and $k\sigma < 0.3$, it can be observed that AIEM and IEM both predict values that agree with both SPM and PO. The results from forward and backward scattering showed earlier that SPM did not agree with PO and both IEM based methods in this region. The same values for $k\sigma$ were used as mentioned in the previous paragraph.

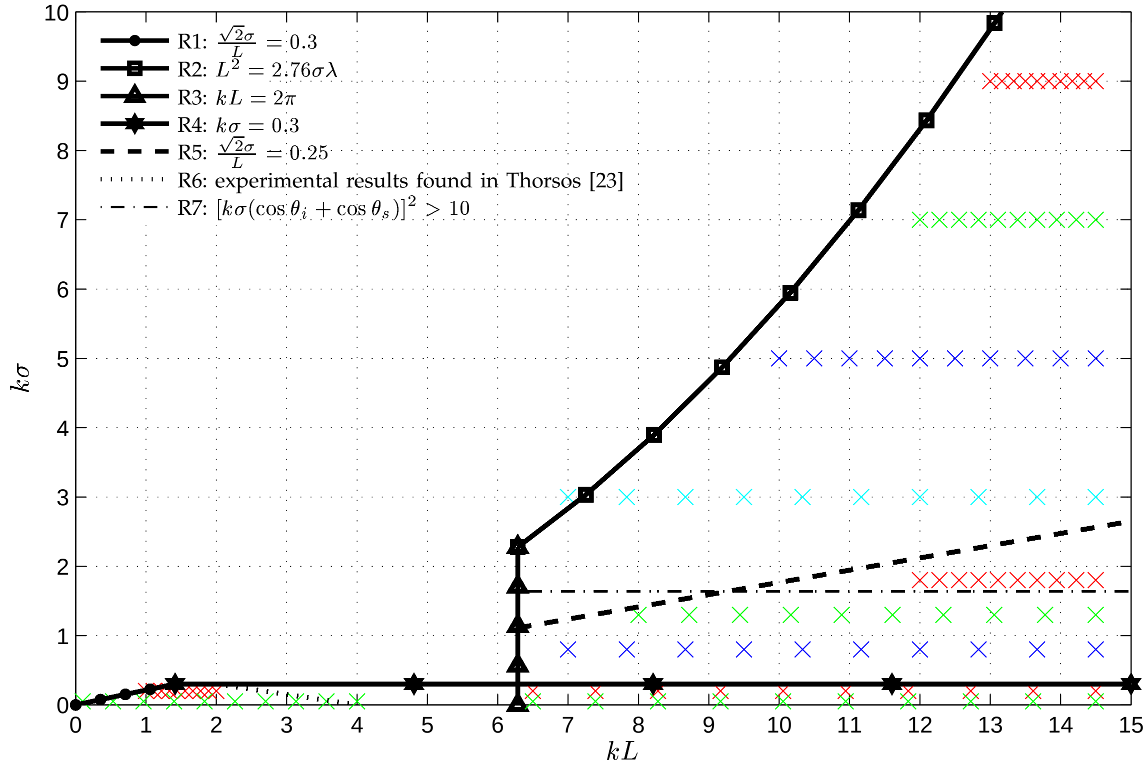

(a) Forward and backward scattering

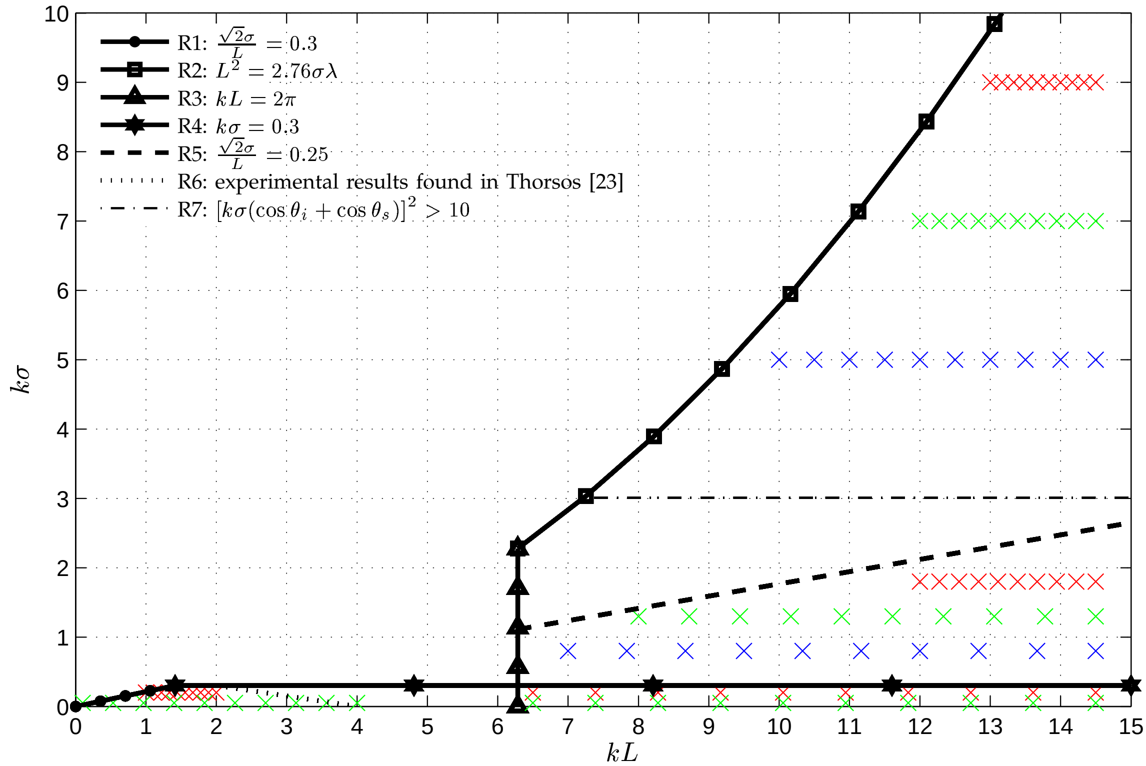

(b) Bistatic scattering

Fig. 9.1: (a) For forward and backward scattering, the chosen kL and $k\sigma$ values are shown with cross-marks in the figure and the colors correspond to the colors in Figures 9.2-9.5. The line corresponding to rule R7 is put in its highest possible position for the angle combinations used in the study described in Section 9.1.1. (b) For bistatic scattering, the same routines regarding the cross-marks applies as for forward and backward scattering but it refers to Figures 9.6-9.7 instead and the results are described in Section 9.1.2.

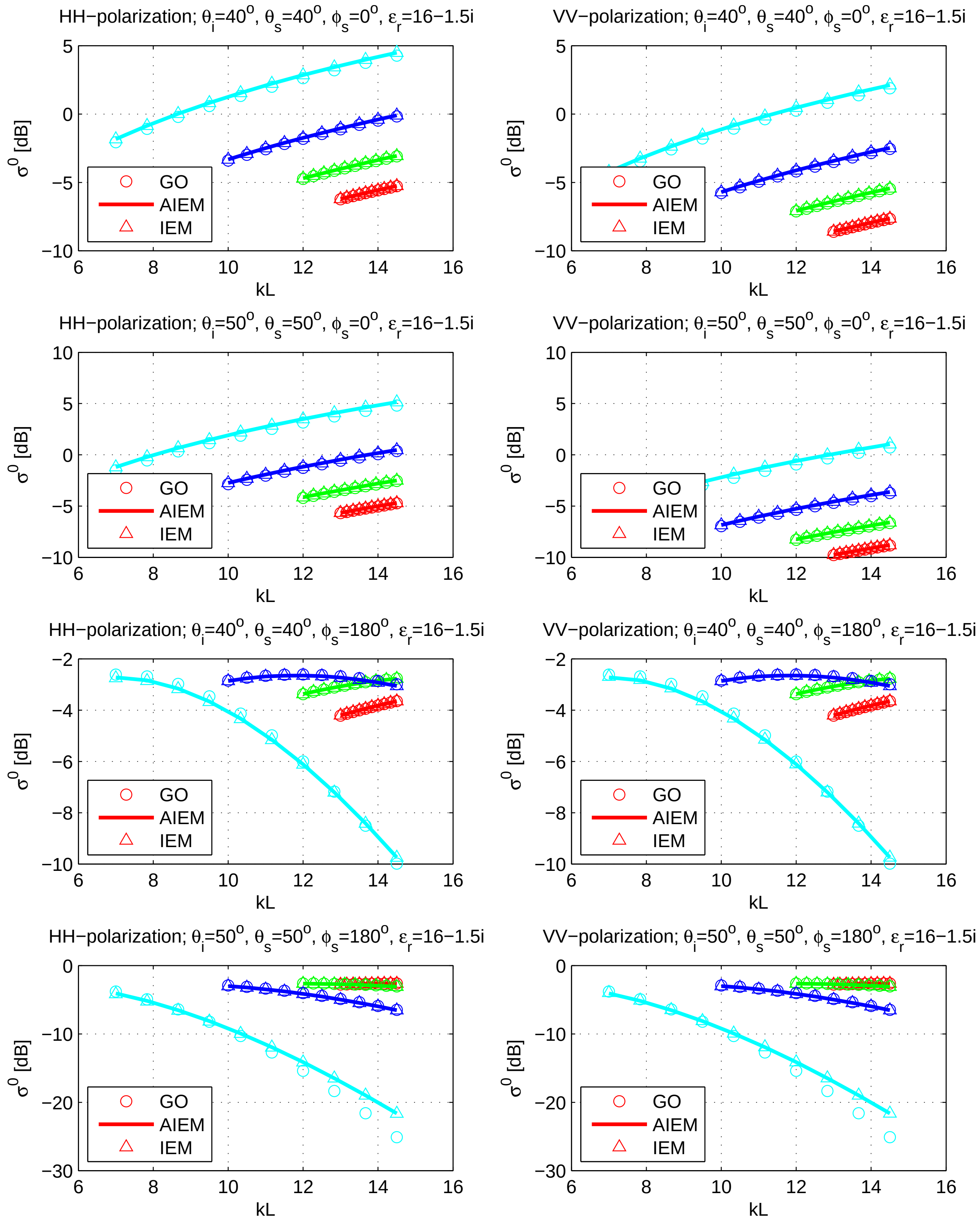

Fig. 9.2: In the case of backward and forward scattering in the GO-region, one can see that the agreement of the methods is almost perfect. One interesting observation is that for backscattering at $\theta_i = 40°$, the scattering coefficient first rises with $k\sigma$ but then starts to fall again. Apparently, there must be some kind of maximum for σ^0. Values of $k\sigma$ are 3.0 (cyan), 5.0 (blue), 7.0 (green), and 9.0 (red, see Figure 9.1a). Note an overestimation of σ^0 given by AIEM and IEM as compared with GO for backscattering, high kL-values, and low $k\sigma$-values.

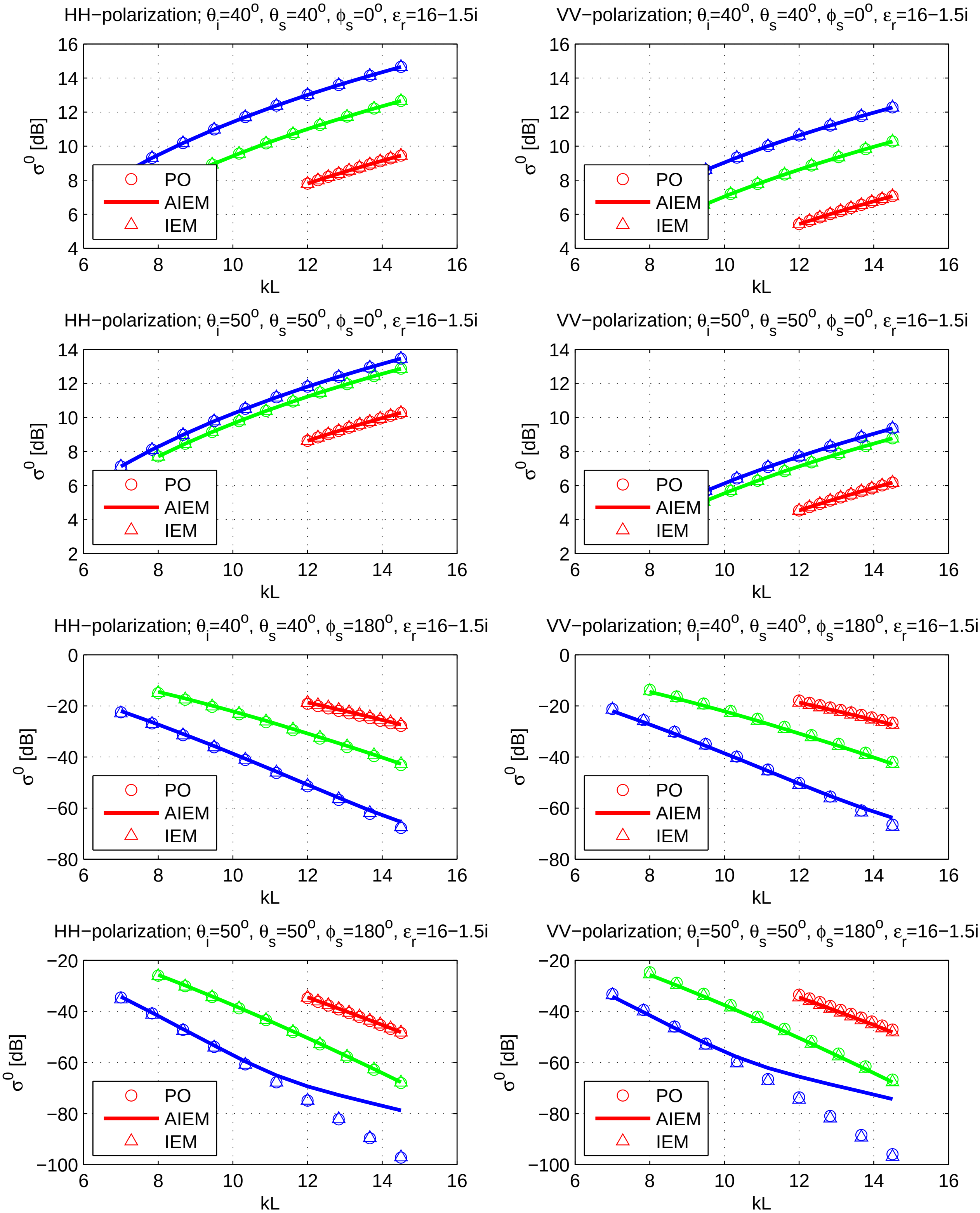

Fig. 9.3: The curves for forward scattering at $\theta_i = 50°$ show some uneven spacing that can be a result of a maximum on its way to being reached. Values of $k\sigma$ are 0.8 (blue), 1.3 (green), and 1.8 (red, see Figure 9.1a). Note a big overestimation of σ^0 given by AIEM as compared with GO for backscattering, high kL-values, and low $k\sigma$-values.

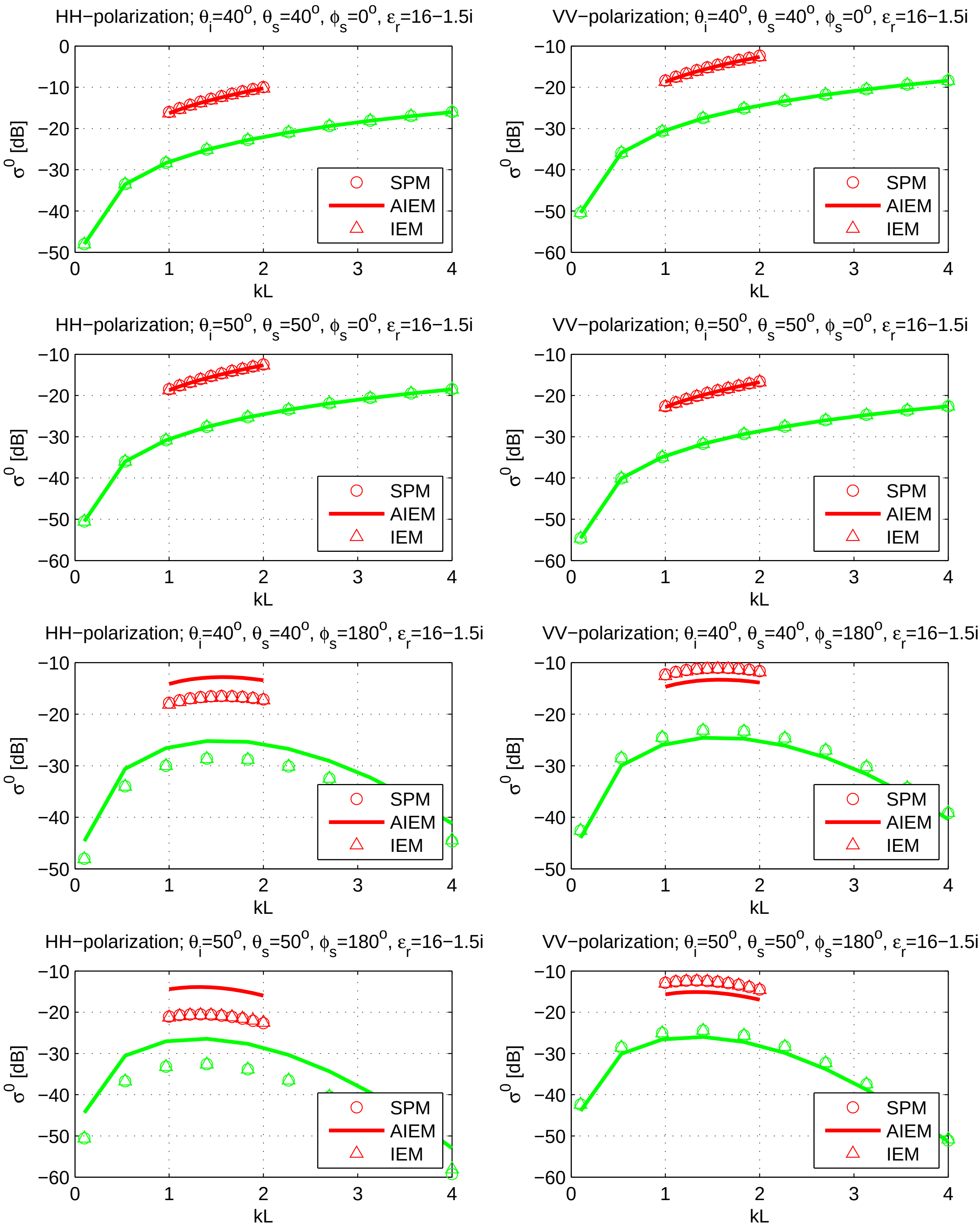

Fig. 9.4: For the SPM-region (with the restriction from Thorsos [23] included), the three models seem to agree very well except for backscattering, where AIEM does not agree well with SPM and IEM. For backscattering, there seems to be a maximum of scattering as well. In VV mode, backscatter is slightly stronger. $k\sigma$ was set to 0.05 (green) and 0.2 (red), see Figure 9.1a. Note that backscattering in the SPM-region gives higher VV than HH, a result that is not observed for any other scenario.

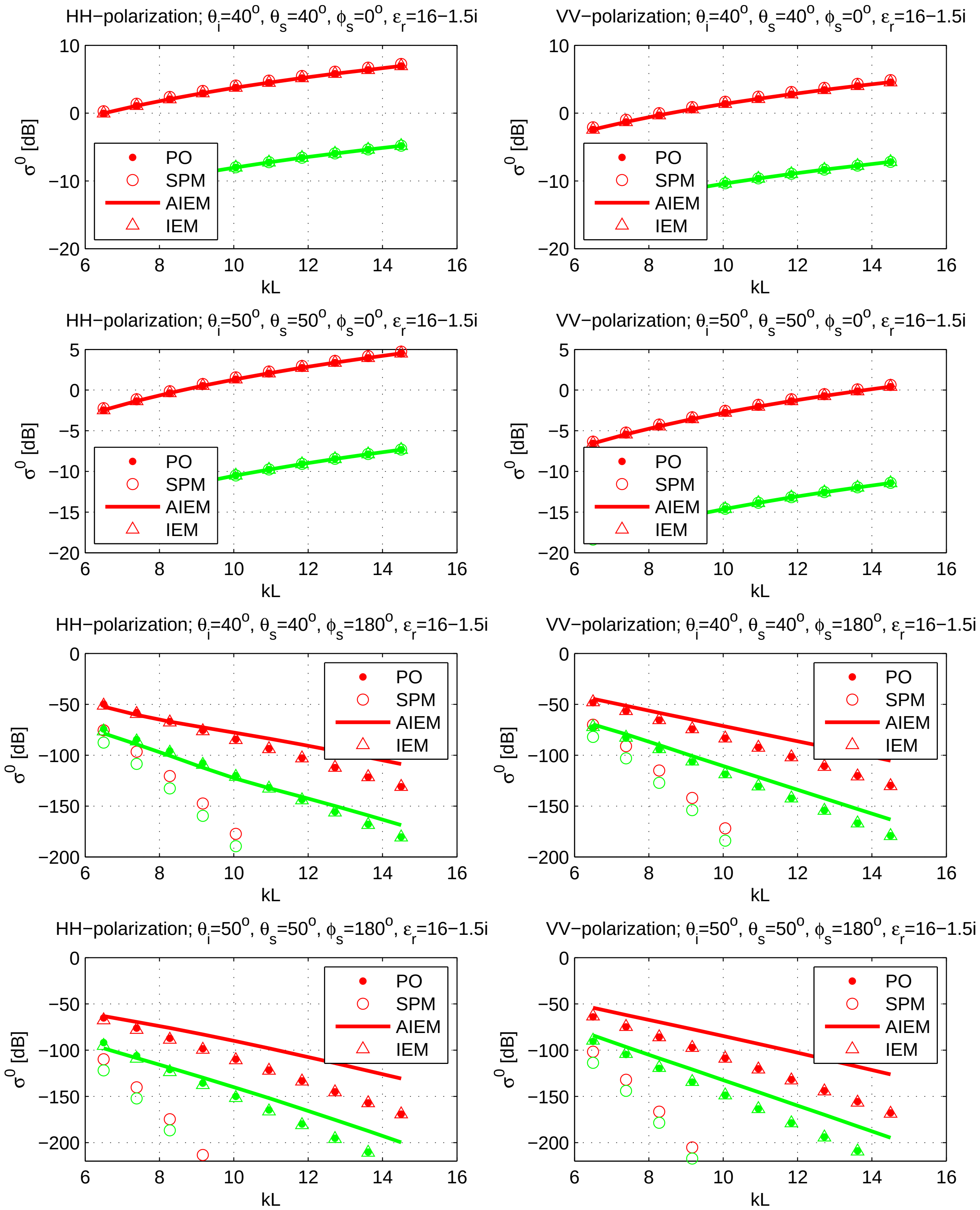

Fig. 9.5: In the region where both SPM and PO are valid according to Ulaby et al. [4], the agreement is good for forward scattering. In backward scattering, SPM gives very low, unrealistic values and AIEM also gives values higher than those predicted by both IEM and PO. The other results are rather predictable apart from the fact, that the slightly higher value of $k\sigma$ gives a stronger forward scattering coefficient. This is an interesting result that cannot be understood intuitively. $k\sigma$ was set to 0.05 (green) and 0.2 (red, see Figure 9.1a).

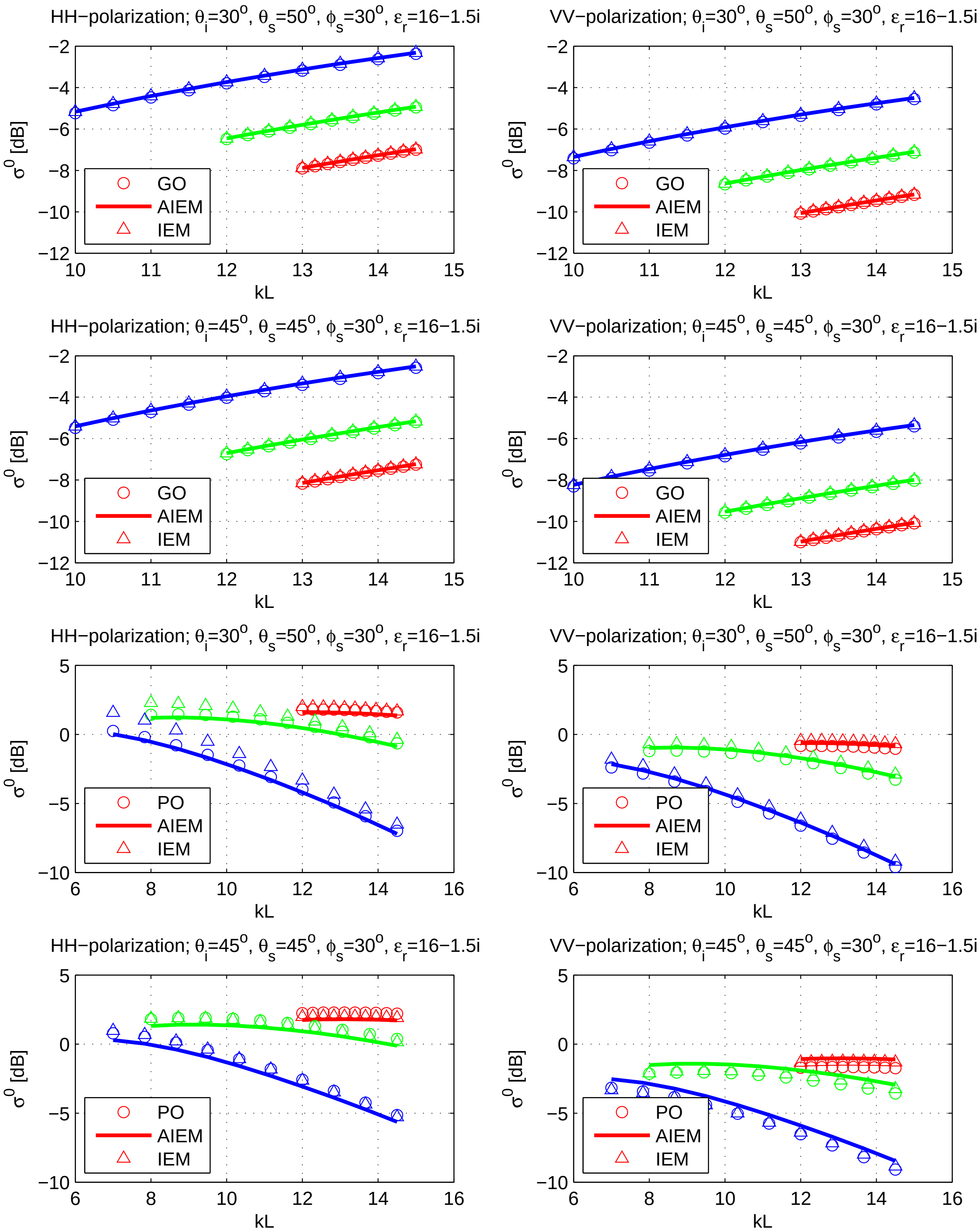

Fig. 9.6: In the bistatic case, the results in both KM-regions are quite predictable. For high $k\sigma$-region (GO, top two rows), an increase of correlation length gives higher scattering coefficient. As kL grows, the facets become bigger but there is still quite large horizontal variation so that bistatic scattering coefficient also grows. For PO (bottom two rows), larger facets together with low $k\sigma$ means that the surface becomes even more flat and less radiation is scattered in bistatic directions (and more in the forward direction). For the PO validity region, AIEM slightly disagrees with the other methods. $k\sigma$ was set to 5.0 (blue), 7.0 (green), and 9.0 (red) for GO, and 0.8 (blue), 1.3 (green), and 1.8 (red) for PO, see Figure 9.1b.

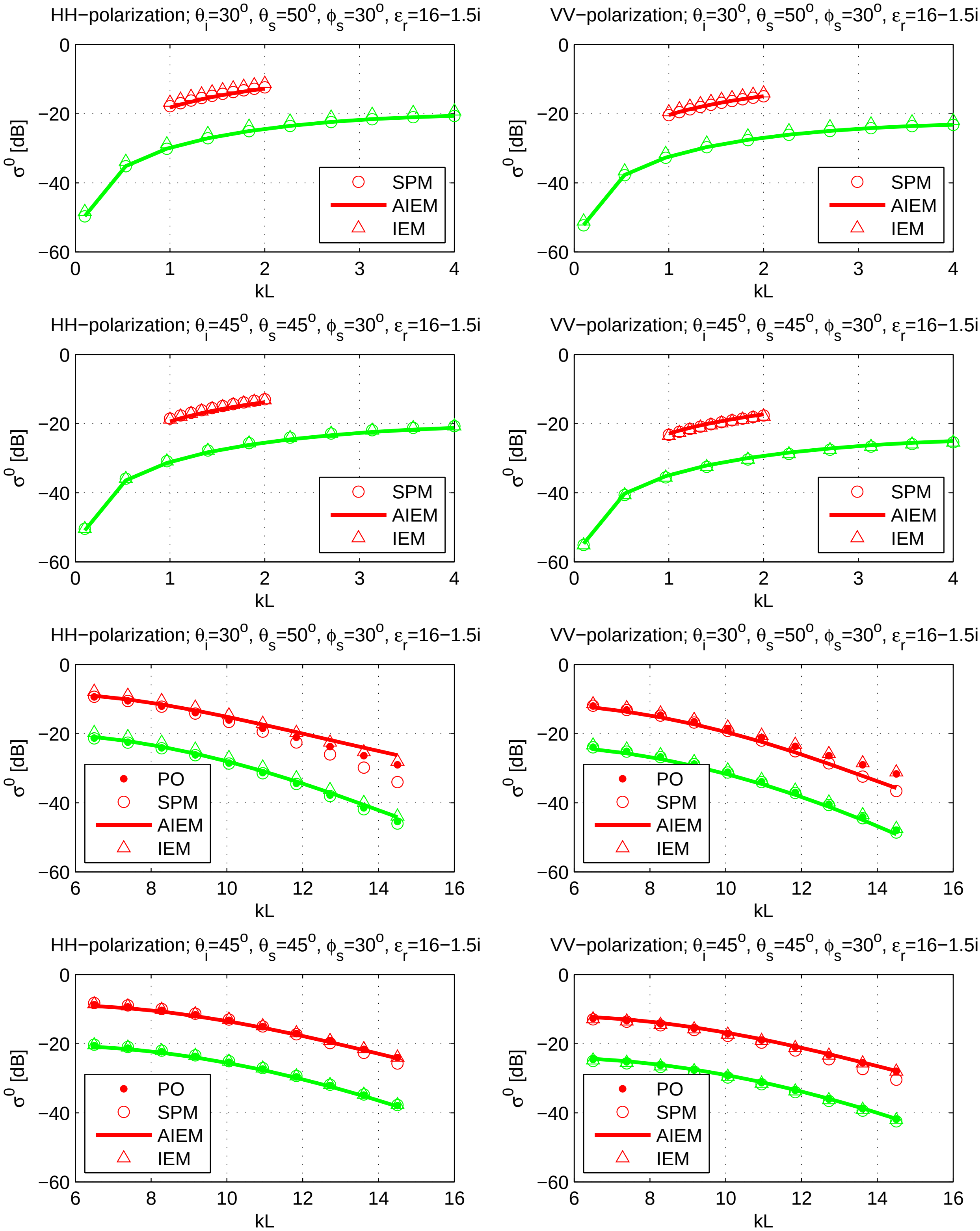

Fig. 9.7: In the SPM validity region, the bistatic scattering coefficient shows the same trends as for forward and backward scattering. This is an expected reaction since scattering in this region occurs mostly in the incoherent way, quite isotropically. Even in the joint PO/SPM region scattering occurs in an intuitive way that reminds very much of scattering in PO-region from Figure 9.6. All methods seem to agree well in this region. $k\sigma$ was set to 0.05 (green) and 0.2 (red), see Figure 9.1b.

9.2 Constant Correlation Length

The next test was performed with exactly the same angle setups as before but now, $k\sigma$ was swept over a wide range of values and kL was kept constant. The values for kL and $k\sigma$ were chosen according to Figure 9.8. Colors of the marks in Figure 9.8a correspond to colors in Figures 9.9-9.10 and colors of the marks in Figure 9.8b correspond to colors in Figure 9.11.

9.2.1 Forward and Backward Scattering

Kirchhoff Region

For forward and backward scattering, kL was set to 8.0, 11.0, and 14.0 while $k\sigma$ was swept from 0.1 to the upper limit for GO. Instead of testing the models separately for GO and PO, one test was made for both in a wider range of $k\sigma$ and both methods were plotted. The common region for PO and GO is called the Kirchhoff region.

In the region where any of the two Kirchhoff methods is valid, the scattering coefficient for forward scattering is observed to first rise to a maximum around $k\sigma \approx 1.0$ and then fall again, see the two first rows of images in Figure 9.9. The scattering is expected to be maximal in the forward direction for a flat surface, and it shows that there must exist a scattering term that has not been accounted for. This term is the coherent term that consists of a "spike" (delta function) in the specular direction. In backscattering, σ^0 first increases with $k\sigma$ and then starts to fall slowly. The value of $k\sigma$ corresponding to the maximum value of the backscattering coefficient becomes higher as kL rises and also, the slope of the curves after the maximum is higher for the lower angle setup with $\theta_i = 40°$. AIEM and IEM follow PO well for low $k\sigma$ and GO for high $k\sigma$. In forward scattering, IEM fails to follow GO after around $k\sigma = 2$ and it falls down to $-\infty$. Generally, backscattering coefficient is smaller than forward scattering coefficient, especially for low values of $k\sigma$. This is an expected result since small standard deviation of a surface makes is locally smooth and reflects most of the radiation specularly.

Small Perturbation Region

In Figure 9.10, the results are presented for the region where SPM is valid according to Ulaby et al. [4] with the correction presented in Thorsos [23]. kL is set to 0.5, 1.0, 1.5, and 2.5. Both forward and backscattering cases show the same trends — σ^0 increases with $k\sigma$. In forward scattering, an increasing kL makes σ^0 grow while for backscattering, the change of kL affects σ^0 in a more complicated way. Values of kL lying in the middle of the validity region seem to give the highest σ^0. For backscattering, AIEM gives an overestimation of σ^0 compared to SPM and IEM in the HH-mode (underestimation in VV-mode). SPM simulated values give higher backscatter coefficients for VV than HH, the opposite trend compared to the other scenarios.

9.2.2 Bistatic Scattering

Kirchhoff Region

In Figure 9.11, the results of simulations in the GO and PO regions are shown. High $k\sigma$-values give generally lower bistatic scattering coefficients for both modes while high kL gives higher σ^0. Therefore, highest scattering coefficient is due to gently undulating surfaces with relatively small standard deviation. There is a maximal value of the bistatic scattering coefficient that can be achieved. This value is both kL- and $k\sigma$-dependent. Both integral equation-based models follow the asymptotic models well except for very high $k\sigma$ where AIEM fails to trace GO and IEM and falls off towards $-\infty$. PO does not work well for high $k\sigma$, which is to be expected in view of its validity region.

Small Perturbation Region

Finally, in the SPM-region, one can see the typical behavior that occurs for small correlation lengths and small standard deviation values — no big difference between bistatic scattering and the scattering in the plane of incidence can be seen.

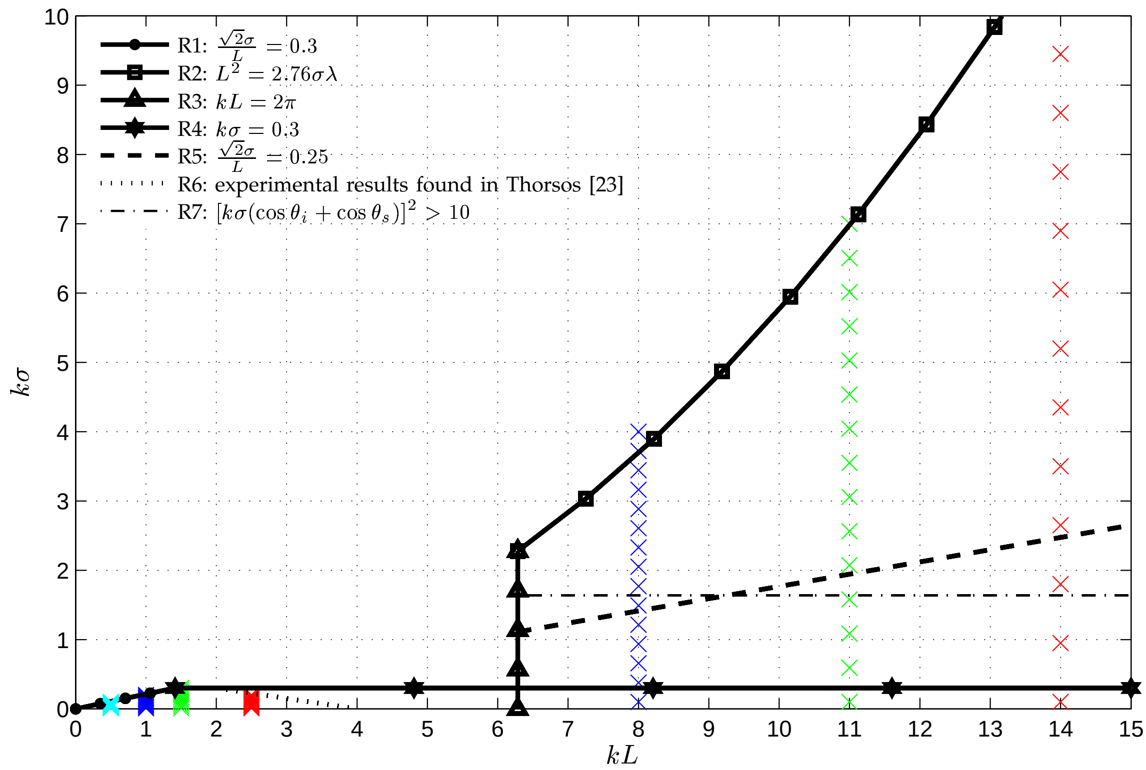

(a) Forward and backward scattering

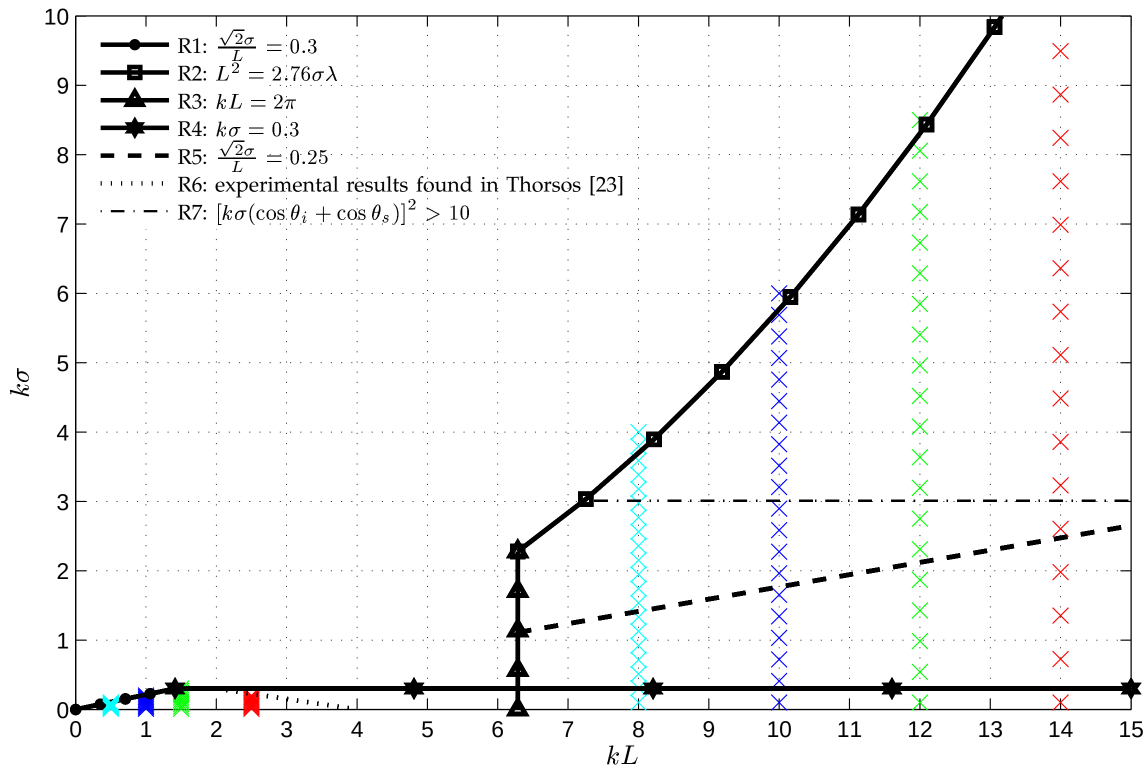

(b) Bistatic scattering

Fig. 9.8: (a) For forward and backward scattering, the chosen kL and $k\sigma$ values are shown with cross-marks in the figure and the colors correspond to the colors in Figures 9.9-9.10. The line corresponding to rule R7 is put in its highest possible position for the angle combinations used in the study described in Section 9.2.1. (b) For bistatic scattering, the same routines regarding the cross-marks applies as for forward and backward scattering but it refers to Figure 9.11 instead and the results are described in Section 9.2.2.

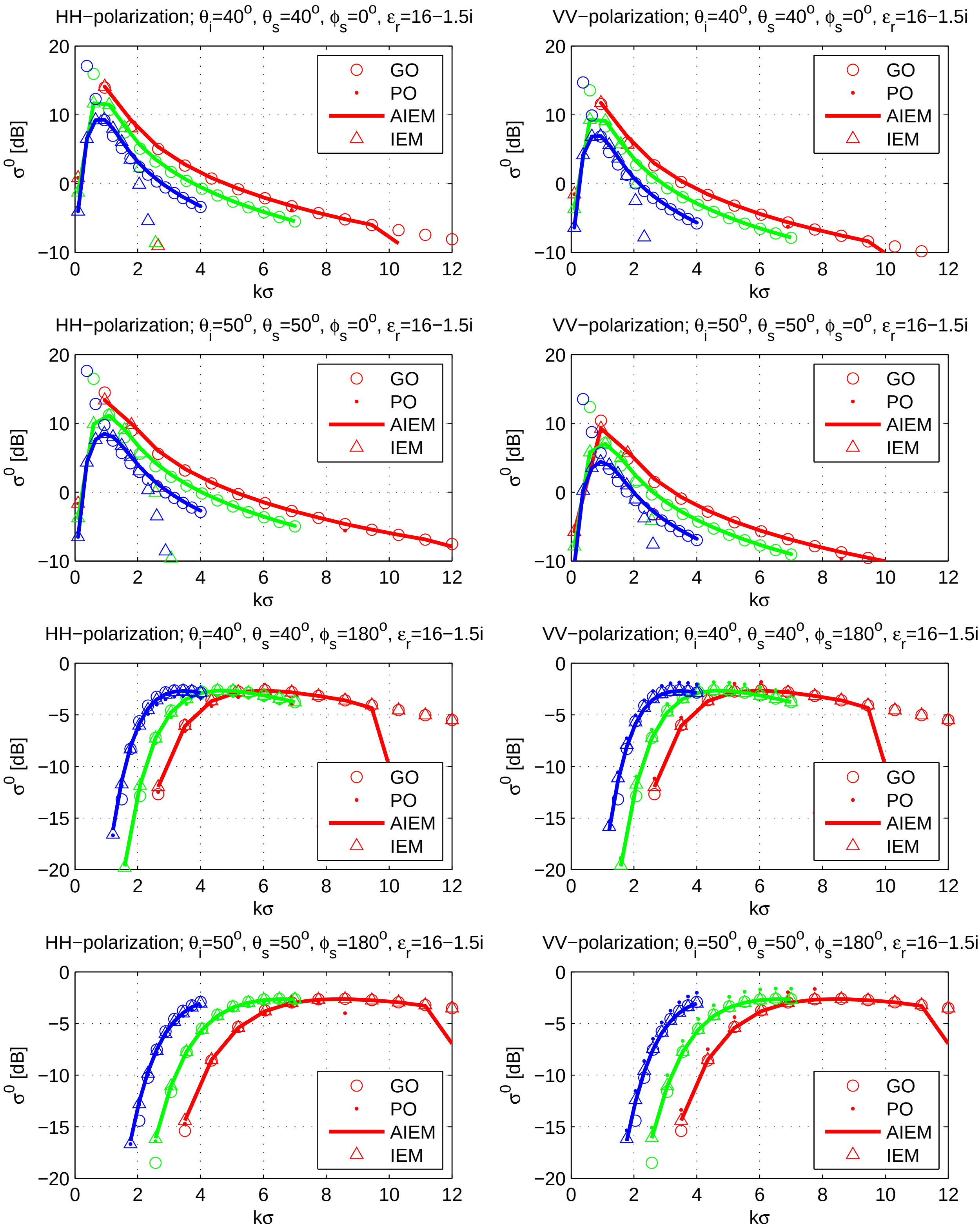

Fig. 9.9: In the Kirchhoff region, a very interesting observation can be made. The coefficient for forward scattering seems to be maximized when $k\sigma \approx 1.0$ in forward scattering which proves that the coherent term is not included in the models (otherwise scattering would be maximal in the specular direction). In backward scattering, there is also a maximum, but that value is much more strongly affected by the scattering angles and correlation lengths. The values for kL that are used are: 8.0 (blue), 11.0 (green), and 14 (red), see Figure 9.8a. PO shows some inconsistent results for high $k\sigma$ which is to be expected since it is not valid there.

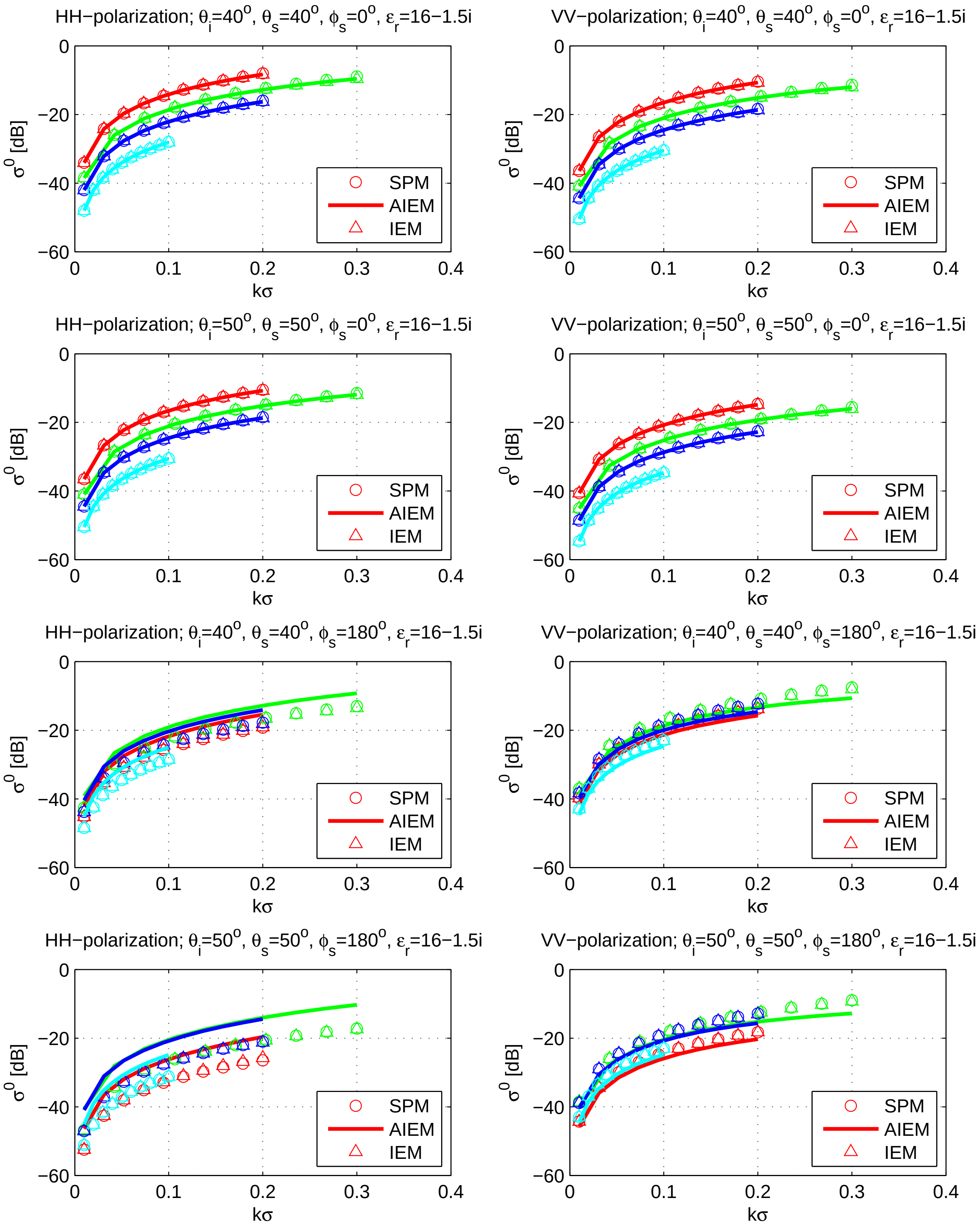

Fig. 9.10: In the SPM-region, the scattering coefficients seem to increase both in forward and backward scattering as $k\sigma$ increases. The trends look quite alike those observed earlier and shown in Figure 9.7 and in Figure 9.4. In the figure above, the used values of kL are: 0.5 (cyan), 1.0 (blue), 1.5 (green), and 2.5 (red), see Figure 9.8a. The agreement of AIEM with IEM and SPM is not really good for backscattering. As one can see, SPM and IEM give higher value of VV compared to HH. This is a result that cannot be found in the other scenarios.

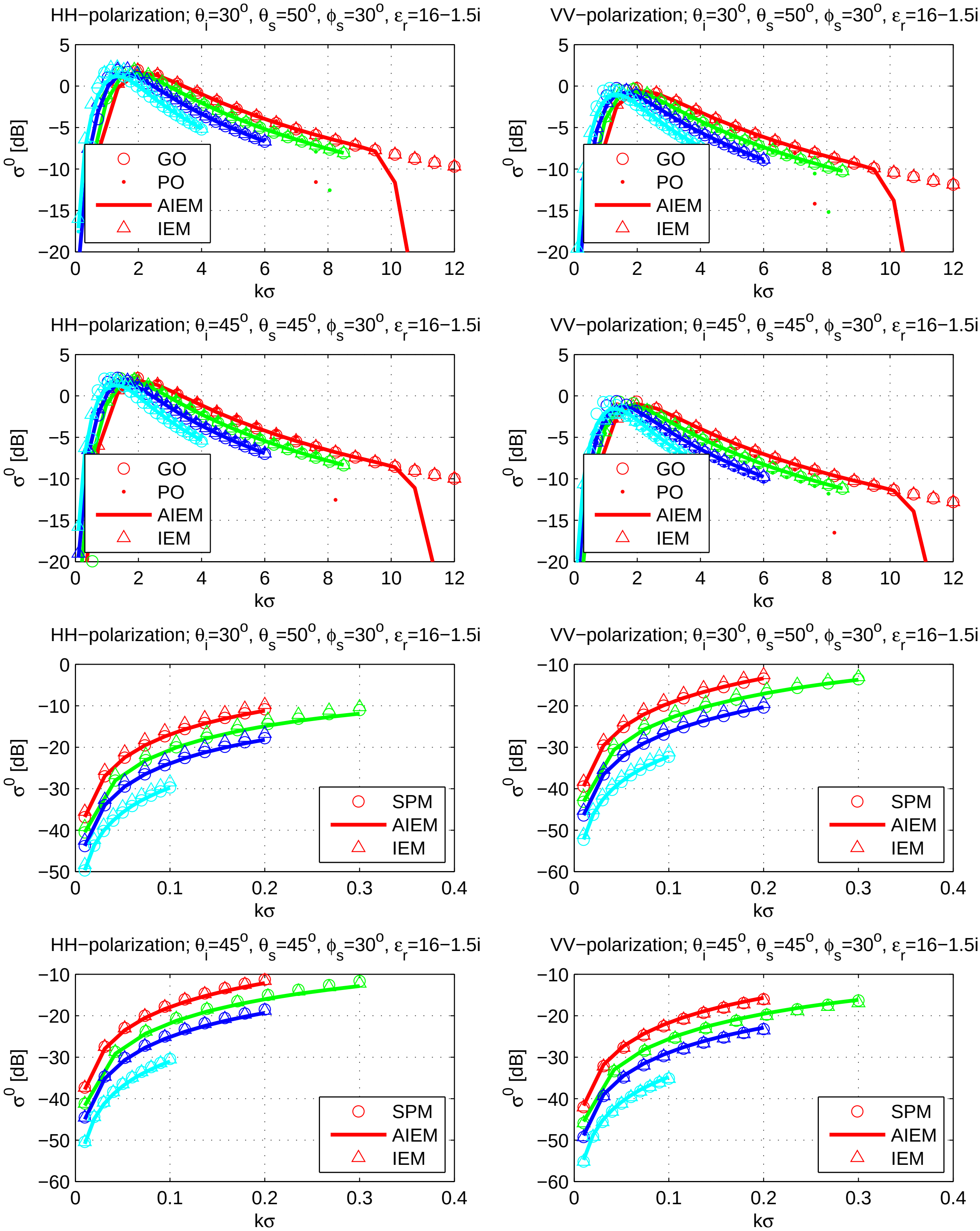

Fig. 9.11: The same result as for forward and backward scattering are observed here for bistatic scattering in the Kirchhoff region (top two rows) — namely the fact that σ^0 is maximized for a slightly rough surface. For bistatic scattering, this is not as surprising because one would expect a slightly rough surface to give more bistatic scattering than a smooth surface. For SPM (bottom two rows), the results are almost the same as for backward and forward scattering and the observation that scattering is almost isotropic in the SPM-region is confirmed. Figure 9.8b shows the values of kL used in KM-region: 8.0 (cyan), 10.0 (blue), 12.0 (green), and 14.0 (red) and in SPM-region: 0.5 (cyan), 1.0 (blue), 1.5 (green), and 2.5 (red). PO shows some inconsistent results for high $k\sigma$ in the top two rows which is to be expected since it is not valid there.

10 DISCUSSION AND CONCLUSIONS

This project consisted of three steps: 1) theoretical study of the different models, 2) model implementation, validation, and application, and 3) analysis and evaluation of the results. During the first step, different ways of simulating radar scattering were examined thoroughly. The choice of SPM, PO, and GO as references is natural for reasons that are both computational and historical (easier expressions that have been used for a long time). There are really few models that try to bridge the gap between SPM and GO/PO. Most of the current work in that field is centered around IEM and that is why Integral Equation Model was used. Since this method has evolved a lot since it first was presented in 1992, both the earliest and the latest version (AIEM) were chosen in order to show potential differences between them. Finally, IIEM was used in some parts of the project because an implemented version of it was provided by Gustafsson [37], which was treated as a reference during validation. Also, during this step, a study of texts that describe some applications of the electromagnetic models in connection with empirical data was made in order to get an idea of the procedures needed for a trustworthy examination.

The essential part of this project is the second step, during which the chosen models were first implemented, then verified, and finally applied in some studies. More about those steps can be found in the paragraphs that follow.

10.1 Model Implementation

During model implementation, a lot had to be taken into consideration. Even the simplest expressions for single scattering (presented in Appendix C) are rather complicated and careful implementation of each coefficient was needed. Even careful insertion of the coefficients and expressions into Matlab® could not prevent some problems that occurred when AIEM was being implemented according to Wu et al. [14]. The main author of that article was contacted by e-mail and it was confirmed that some misprints occurred in the article. Fortran code for AIEM was provided as well. After that, AIEM started to work well. Moreover, expressions for PO gave some troubles as well. PO is presented in both Ulaby et al. [4] and Ulaby et al. [6] but the implementation of these expressions was problematic (due to possible misprints and/or the human factor). Instead, scattering coefficients found in de Roo [26] were used and worked well.

Another concern that occurs for numerical evaluations of the scattering coefficients are the infinite sums and integrals found in the expressions. Since only single scattering was implemented, there were no integrals present and thus only infinite sums needed some attention. The sums can normally be cut at some point since they are convergent. The choice of that point is important, but, using modern computers, the speed of computation of the sums is so high, that hundreds of terms can be taken without any major loss of computation speed. In practice, the sums were cut when the relative change was low enough. A consequence of not including multiple scattering in the models was that the simulated scattered, cross-polarized fields became gravely underestimated (a big part of depolarization comes from multiple scattering) and were thus omitted in the study.

Transition function was also implemented according to the Fortran file provided by Wu [38]. The transition function also contained an infinite sum that had to be cut at some point. It was discovered, that this sum converged more slowly and more terms had to be taken into consideration. However, since the relative change was used as a criterion for the sum to be cut, this was only an issue if a fixed number of sum terms were used. The inclusion of the shadowing function into the models was not problematic since the function has a really simple form.

10.2 Model Verification

After the models have been implemented, they needed to be tested. Since no numerical values were accessible for comparison, the verification was done against figures presented in articles and books. The most valuable article from that point of view was Wu et al. [14] since it contained many figures for different angle setups, dielectric contants, and models used. In the article, AIEM, IIEM, and IEM were used together with SPM, GO, and a method referred to as KM (which probably was the same as PO, although this was not mentioned in the article). Additionally, some of the implemented models were compared to the results found in Ulaby et al. [4], Fung et al. [11], and Wu and Chen [13] but those results are not presented in this text. As mentioned earlier, the disagreement in the position of the dips of σ^0 was essentially the only encountered and unexplained problem.

In some cases, it was uncertain which model version was used and how. For the figures in Wu et al. [14], it was not mentioned whether shadowing function was used or not. The results presented here were produced without using the shadowing function except in IIEM. Also, unless specified otherwise, transition function was used for

AIEM.

It is possible that there are some minor mistakes in the models implemented by the author, but generally, the results of the model verification showed very good results. The only issue was the azimuthal disagreement in dip position and a slight disagreement of AIEM with SPM in the region where kL and $k\sigma$ are small.

10.3 Model Application

The results of the study of the scattering coefficient against surface parameters $k\sigma$ and kL show some interesting results. First and foremost, the results agree with the intuitive conclusions for both very smooth and very rough surfaces. For example, in GO-region, longer correlation lengths give higher scattering coefficients in forward scattering but also lower backscatter coefficients (as expected for specular reflection). Also, higher incidence angle (closer to grazing) gives less backscatter but more forward scatter. σ^0_{HH} is also higher than σ^0_{VV} since the first one is not affected by the Brewster angle.

What was less expected was the discovery of the maxima of scattering coefficients found for forward scattering in the region where Kirchhoff approximation is valid. The results indicate that for a certain value of kL and $k\sigma$, the scattering coefficient is maximal. Ideally, one could think that σ^0 in forward scattering should be greatest when $k\sigma$ is close to zero and kL is high, and the bistatic and backward scattering coefficient would be quite low everywhere. However, it was discovered that the scattering coefficient for bistatic and forward scattering in KM-region is maximized if there is some vertical roughness in the surface. The same happens with backscattering coefficient but it is less distinguished. For forward scattering, this means that the implemented models are not valid in the region of very small $k\sigma$ because the coherent term is not included.

During the examination of the root-mean-square deviation of the modeled scattering coefficients most of the results regarding validity regions were confirmed. It was also noted, that the RMSE graphs should be used together with the validity region figures. RMSE graphs do not say anything about model validity against the true values, but only about the agreement of the different models against each other.

When studying bistatic scattering for different angles θ_s and ϕ_s, a discovery was made that VV-polarization is much less affected by the angular setup than HH-polarization mode. Once again, the difference between the two modes can be a result of the different degree of interaction with the surface around the Brewster angle for both modes. It was observed that for VV most scattering occurs in the normal direction, even for surfaces valid for Kirchhoff approximation.

10.4 Future work

Due to time limitations of this project and space limitations of this report, some issues and ideas that have come up during work had to be skipped. The possible future development of this project may include:

- a thorough study of the origin of the difference in dip position of the dips in the examination of the azimuthal behavior,
- an implementation of multiple scattering for IEM and AIEM according to Fung and Chen [34] and Wu and Chen [13],
- a cross-polarization study for different angle and surface setups, preferably after multiple scattering has been implemented,
- an investigation of the difference in scattering coefficients when shadowing and transition function are used and not used [20],
- an investigation of scattering from surfaces with dielectric and roughness properties that are based on real values in connection with some experimental data [39, 40],
- a study of the model behavior for other than Gaussian correlation functions [41],
- a more complete study of the validity of the methods, preferably with a comparison with method of moments simulations and maybe some other, less common methods like Small Slope Approximation [42] among others (as in Chen and Fung [29] for example),
- some simulations of scattering in regions far from the validity regions of the asymptotic models (or in the intermediate region).

ACKNOWLEDGEMENTS

First, I would like to thank my examiner Prof. Lars Ulander, and my supervisors Gustaf Sandberg and Dr. Leif Eriksson for their constant help and supervision during the project. Also, I would like to thank them for the course in Radar Systems and Applications that has been of great help for me during the project.

I would also like to thank professor Tzong-Dar Wu (Department of Electrical Engineering, National Central University, Taiwan) for his help with the implementation of AIEM. Due to some misprints in Wu et al. [14], the first implementation of AIEM did take a lot more time than expected and gave poor results. After a contact via e-mail with Prof. Wu, a file with Fortran code for AIEM was provided to me and the implementation was much more successful.

Additionally, I would like to thank Mr. Magnus Gustafsson (who is with FOI, Swedish Defence Research Agency, Linköping, Sweden) for his Matlab® code for IIEM that has been of great use for me.

Finally, I would like to thank my family, my friends, and all other people who supported me during this project.

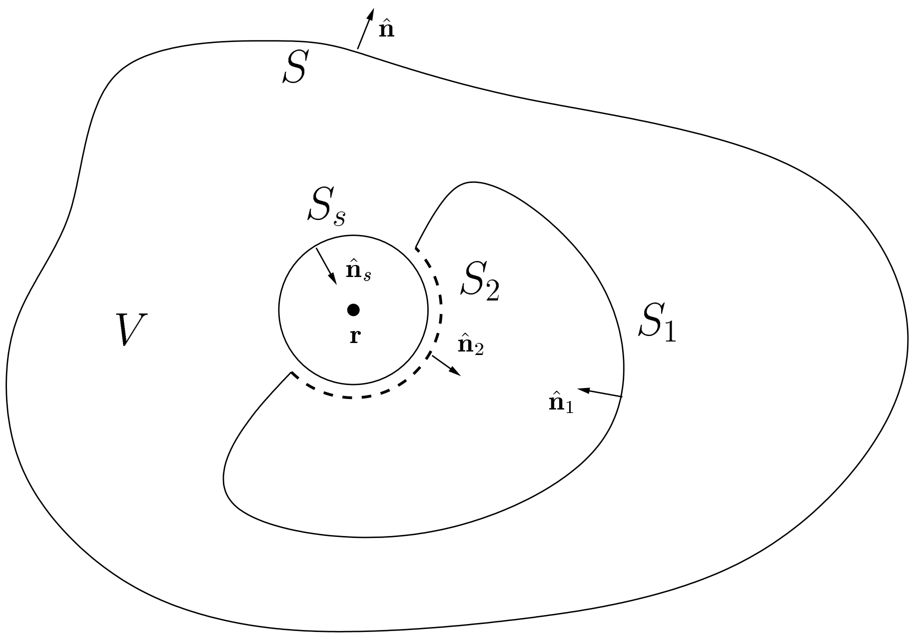

Fig. A.1: The nomenclature used for the derivation of the electric and magnetic field integral equations.

APPENDIX A
INTEGRAL REPRESENTATION FOR ELECTROMAGNETIC FIELDS

A.1 Maxwell's Equations

The four Maxwell's equations are [10, 28, 43]:

$$\begin{aligned}
\nabla \times \mathbf{E} &= -j\omega\mu\mathbf{H} - \mathbf{K}, && \text{(A1)}\\
\nabla \times \mathbf{H} &= j\omega\varepsilon\mathbf{E} + \mathbf{J}, && \text{(A2)}\\
\nabla \cdot \mathbf{E} &= \rho/\varepsilon, && \text{(A3)}\\
\nabla \cdot \mathbf{H} &= m/\mu. && \text{(A4)}
\end{aligned}$$

They are completed by the charge conservation relationships:

$$\begin{aligned}
\nabla \cdot \mathbf{J} &= -j\omega\rho, && \text{(A5)}\\
\nabla \cdot \mathbf{K} &= -j\omega m, && \text{(A6)}
\end{aligned}$$

where ε and μ are dielectric constants for the relevant medium, and ω is the angular frequency of the wave. $\mathbf{J}$ and $\mathbf{K}$ are the electric and magnetic magnetic current densities, and ρ and m are charge densities (magnetic monopoles are assumed).

A.2 Vector Wave Equations

By a cross multiplication of ∇ from the left with equations (A1) and (A2) and by using equations (A1)-(A4) for substitutions, the following two vector wave equations are found:

$$\begin{aligned}
\nabla \times \nabla \times \mathbf{E} - k^2\mathbf{E} &= -j\omega\mu\mathbf{J} - \nabla \times \mathbf{K}, && \text{(A7)}\\
\nabla \times \nabla \times \mathbf{H} - k^2\mathbf{H} &= -j\omega\varepsilon\mathbf{K} + \nabla \times \mathbf{J}, && \text{(A8)}
\end{aligned}$$

where $k^2 = \omega^2\varepsilon\mu$.

A.3 Electric Field Integral Equation

In order to solve (A7) and (A8) Green's Vector Theorem need to be used [4, 10]:

$$\int_V (\mathbf{Q} \cdot \nabla \times \nabla \times \mathbf{P} - \mathbf{P} \cdot \nabla \times \nabla \times \mathbf{Q})\, \mathrm{d}v = \int_\Sigma (\mathbf{P} \times \nabla \times \mathbf{Q} - \mathbf{Q} \times \nabla \times \mathbf{P}) \cdot \mathbf{ds}, \tag{A9}$$

where $\mathbf{P}$ and $\mathbf{Q}$ are arbitrary vector functions of position with continuous first and second derivatives in the volume V and on its boundary Σ. After setting $\mathbf{P} = \mathbf{E}$, choosing $\mathbf{G}$ to be

$$\mathbf{G} = \hat{\mathbf{a}}\chi(\mathbf{r}, \mathbf{r}') = \hat{\mathbf{a}}\frac{\mathrm{e}^{-j\mathbf{k}|\mathbf{r}-\mathbf{r}'|}}{|\mathbf{r}-\mathbf{r}'|}, \tag{A10}$$

where $\hat{\mathbf{a}}$ is an arbitrary orientation unit vector, and $\mathbf{r}$ and $\mathbf{r}'$ are observation and source position vectors respectively, and using (A7), the equation (A9) turns into:

$$\begin{aligned} &\int_V [j\omega\mu\mathbf{J}\chi(\mathbf{r},\mathbf{r}') + \mathbf{K}\times\nabla\chi(\mathbf{r},\mathbf{r}') - (\rho/\varepsilon)\nabla\chi(\mathbf{r},\mathbf{r}')]\,\mathrm{d}v = \\ = &\int_\Sigma [j\omega\mu(\hat{\mathbf{n}}\times\mathbf{H})\chi(\mathbf{r},\mathbf{r}') - (\hat{\mathbf{n}}\times\mathbf{E})\times\nabla\chi(\mathbf{r},\mathbf{r}') - (\hat{\mathbf{n}}\cdot\mathbf{E})\nabla\chi(\mathbf{r},\mathbf{r}')]\,\mathrm{d}s, \end{aligned} \tag{A11}$$

where $\hat{\mathbf{n}}$ is a unit normal for Σ.

Since the Green's function

$$\chi(\mathbf{r}, \mathbf{r}') = \frac{\mathrm{e}^{-j\mathbf{k}|\mathbf{r}-\mathbf{r}'|}}{|\mathbf{r}-\mathbf{r}'|}$$

is singular when $\mathbf{r} = \mathbf{r}'$, an infinitesimal sphere should be circumscribed about $\mathbf{r}$ as indicated in Figure A.1. The integral over Σ becomes a sum of integrals over different parts of Σ: the outer boundary S, the inner boundary S', and the sphere boundary S_s. S' is divided into S_1, which is the part of the inner boundary that is not affected by the sphere, and S_2, a part of the inner boundary that goes around the sphere. Formally, this can be expressed by:

$$\int_\Sigma = \int_S + \int_{S_1} + \int_{S_2} + \int_{S_s} \tag{A12}$$

and, for each surface the corresponding normal vector is $\hat{\mathbf{n}}$, $\hat{\mathbf{n}}_1$, $\hat{\mathbf{n}}_2$, and $\hat{\mathbf{n}}_s$ respectively.

Only the integrals over S_2 and S_s are affected by the limit $r = |\mathbf{r}-\mathbf{r}'| \to 0$. This part is called I and it becomes:

$$\begin{aligned} I &= \lim_{r\to 0} \int_{S_2+S_s} [j\omega\mu(\hat{\mathbf{n}}\times\mathbf{H})\chi(\mathbf{r},\mathbf{r}') - (\hat{\mathbf{n}}\times\mathbf{E})\times\nabla\chi(\mathbf{r},\mathbf{r}') - (\hat{\mathbf{n}}\cdot\mathbf{E})\nabla\chi(\mathbf{r},\mathbf{r}')]\cdot\mathbf{ds} = \\ &= \lim_{r\to 0}\left[-\mathbf{E}\left(\int_{S_2}\frac{\hat{\mathbf{n}}_2\cdot\hat{\mathbf{n}}_2}{r^2}\,\mathrm{d}s + \int_{S_s}\frac{\hat{\mathbf{n}}_s\cdot\hat{\mathbf{n}}_s}{r^2}\,\mathrm{d}s\right)\right]. \end{aligned} \tag{A13}$$

Since $\hat{\mathbf{r}} = -\hat{\mathbf{n}}_2$ and $\hat{\mathbf{r}} = \hat{\mathbf{n}}_s$, and the solid angle is defined by

$$\mathrm{d}\Omega = \frac{\hat{\mathbf{n}}\cdot\hat{\mathbf{r}}}{r^2}\mathrm{d}s,$$

the integrands in the right hand side of (A13) can be written as

$$\mathrm{d}\Omega_2 = -\frac{\hat{\mathbf{n}}_2\cdot\hat{\mathbf{n}}_2}{r^2}\mathrm{d}s, \tag{A14}$$

$$\mathrm{d}\Omega_s = \frac{\hat{\mathbf{n}}_s\cdot\hat{\mathbf{n}}_s}{r^2}\mathrm{d}s. \tag{A15}$$

so that I becomes

$$I = \lim_{r\to 0}\left[-\mathbf{E}\left(\int_{S_2}\frac{\hat{\mathbf{n}}_2\cdot\hat{\mathbf{n}}_2}{r^2}\,\mathrm{d}s + \int_{S_s}\frac{\hat{\mathbf{n}}_s\cdot\hat{\mathbf{n}}_s}{r^2}\,\mathrm{d}s\right)\right] = \lim_{r\to 0}\left[-\mathbf{E}\left(\int_{S_s}\mathrm{d}\Omega_s - \int_{S_2}\mathrm{d}\Omega_2\right)\right]. \tag{A16}$$

The limit of the first integral on the right hand side of (A16) is equal to 4π while the second limit is equal to 2π if $\mathbf{r}$ lies on a smooth part of Σ. If it lies in V but not on Σ, then the integral is 0. If it lies on a part of Σ that is not smooth, some further investigations have to be done.

From (A16), $\mathbf{E}$ can be extracted and, together with (A11) and (A12) it gives:

$$\begin{aligned}\mathbf{E}(\mathbf{r}) \;=\; & -\frac{T}{4\pi}\int\limits_V [j\omega\mu\mathbf{J}\chi(\mathbf{r},\mathbf{r}') + \mathbf{K}\times\nabla\chi(\mathbf{r},\mathbf{r}') - (\rho/\varepsilon)\nabla\chi(\mathbf{r},\mathbf{r}')]\,\mathrm{d}v \,+ \\ & +\frac{T}{4\pi}\int\limits_{S+S_1} [j\omega\mu(\hat{\mathbf{n}}\times\mathbf{H})\chi(\mathbf{r},\mathbf{r}') - (\hat{\mathbf{n}}\times\mathbf{E})\times\nabla\chi(\mathbf{r},\mathbf{r}') - (\hat{\mathbf{n}}\cdot\mathbf{E})\nabla\chi(\mathbf{r},\mathbf{r}')]\,\mathrm{d}s, \end{aligned} \tag{A17}$$

where

$$T = \begin{cases} 2 & \text{if } \mathbf{r} \text{ is on a smooth portion of } \Sigma, \\ 1 & \text{if } \mathbf{r} \text{ is not on } \Sigma. \end{cases}$$

If S is grown to infinity, $\int_S(\bullet)\mathrm{d}s$ can be called $\mathbf{E}^i$ as it represents sources outside S, or, as it will be called from now on, the incident electric field $\mathbf{E}^i$. If there are no sources inside V, then (A17) reduces to:

$$\mathbf{E}(\mathbf{r}) = T\left\{\mathbf{E}^i(\mathbf{r}) - \frac{1}{4\pi}\int\limits_S [j\omega\mu(\hat{\mathbf{n}}\times\mathbf{H})\chi(\mathbf{r},\mathbf{r}') - (\hat{\mathbf{n}}\times\mathbf{E})\times\nabla\chi(\mathbf{r},\mathbf{r}') - (\hat{\mathbf{n}}\cdot\mathbf{E})\nabla\chi(\mathbf{r},\mathbf{r}')]\,\mathrm{d}s\right\}. \tag{A18}$$

where S now simply represents the boundary between V and V^{C}. This equation is often referred to as the *electric field integral equation* (EFIE).

A.4 Magnetic Field Integral Equation

An expression for $\mathbf{H}$ can be found using the same procedures as in Section A.3 above:

$$\mathbf{H}(\mathbf{r}) = T\left\{\mathbf{H}^i(\mathbf{r}) + \frac{1}{4\pi}\int\limits_S [j\omega\mu(\hat{\mathbf{n}}\times\mathbf{H})\chi(\mathbf{r},\mathbf{r}') - (\hat{\mathbf{n}}\times\mathbf{H})\times\nabla\chi(\mathbf{r},\mathbf{r}') - (\hat{\mathbf{n}}\cdot\mathbf{H})\nabla\chi(\mathbf{r},\mathbf{r}')]\,\mathrm{d}s\right\}. \tag{A19}$$

Often, it is referred to as the *magnetic field integral equation* (MFIE). A more detailed derivation of (A18) and (A19) can be found in Poggio and Miller [10].

APPENDIX B
STRATTON-CHU INTEGRAL AND THE FAR FIELD APPROXIMATION

The so-called *Stratton-Chu integral* [44] relates the tangential surface fields to the fields far away from the boundary. The expression for the Green's function χ in (A18) and (A19) is now replaced by its explicit expression:

$$\chi = \frac{\exp\left(-jk|\mathbf{r}-\mathbf{r}'|\right)}{|\mathbf{r}-\mathbf{r}'|}. \tag{B1}$$

The far field assumption gives the following simplification in the denominator of (B1):

$$|\mathbf{r}-\mathbf{r}'| \approx |\mathbf{r}| = r, \tag{B2}$$

and in the exponential (phase) expression:

$$|\mathbf{r}-\mathbf{r}'| \approx r - \mathbf{r}\cdot\mathbf{r}', \tag{B3}$$

see Ulaby et al. [4, App. 12J.5]). The expressions for χ and $\nabla\chi$ become:

$$\chi = \frac{\exp\left(-jkr + jk\mathbf{r}\cdot\mathbf{r}'\right)}{r}, \tag{B4}$$

$$\nabla\chi = \frac{jk\mathbf{r}}{r}\exp\left(-jkr + jk\mathbf{r}\cdot\mathbf{r}'\right). \tag{B5}$$

In the far field, the surface S has to be treated as an open surface and thus the integral in (A18) needs an extra term corresponding to the line integral on the boundary [4, p. 1022]. This gives an expression for the scattered field only:

$$\mathbf{E}^s(\mathbf{r}) = \underbrace{-\frac{1}{4\pi}\int\left[j\omega\mu(\hat{\mathbf{n}}\times\mathbf{H})\chi - (\hat{\mathbf{n}}\times\mathbf{E})\times\nabla\chi - \nabla\chi(\hat{\mathbf{n}}\cdot\mathbf{E})\right]\mathrm{d}s}_{\text{EFIE, (A18)}} + \underbrace{\frac{j}{4\pi\omega\varepsilon}\oint\nabla\chi\mathbf{H}\cdot\mathrm{d}\mathbf{l}}_{\text{integral on } \partial S}, \tag{B6}$$

which after the insertion of (B4) and (B5) gives:

$$\mathbf{E}^s(\mathbf{r}) = \frac{j\mathrm{e}^{-jkr}}{4\pi r}\int\left[(\hat{\mathbf{n}}\times\mathbf{E})\times\mathbf{k} - \omega\mu(\hat{\mathbf{n}}\times\mathbf{H}) + \mathbf{k}(\hat{\mathbf{n}}\cdot\mathbf{E})\right]\mathrm{e}^{j\mathbf{k}\cdot\mathbf{r}'}\,\mathrm{d}s - \frac{\mathrm{e}^{-jkr}}{4\pi r\omega\varepsilon}\mathbf{k}\oint\mathrm{e}^{j\mathbf{k}\cdot\mathbf{r}'}\mathbf{H}\cdot\mathrm{d}\mathbf{l}, \tag{B7}$$

where $\mathbf{k} = k\hat{\mathbf{r}}$. The last term can be re-written using Stoke's theorem, which gives:

$$\begin{aligned}
\oint\mathrm{e}^{j\mathbf{k}\cdot\mathbf{r}'}\mathbf{H}\cdot\mathrm{d}\mathbf{l} &= \int\nabla\times\left(\mathbf{H}\mathrm{e}^{j\mathbf{k}\cdot\mathbf{r}'}\right)\cdot\mathrm{d}\mathbf{s} = \\
&= \int\left[\left(\nabla\mathrm{e}^{j\mathbf{k}\cdot\mathbf{r}'}\right)\times\mathbf{H} + \mathrm{e}^{j\mathbf{k}\cdot\mathbf{r}'}\nabla\times\mathbf{H}\right]\cdot\mathrm{d}\mathbf{s} = \\
&= \int\left(j\mathbf{k}\times\mathbf{H} + j\omega\varepsilon\mathbf{E}\right)\mathrm{e}^{j\mathbf{k}\cdot\mathbf{r}'}\cdot\mathrm{d}\mathbf{s}
\end{aligned} \tag{B8}$$

and with (B7), the expression for $\mathbf{E}^s$, that is the far field expression for the scattered electric field becomes:

$$\mathbf{E}^s = -\frac{jk\mathrm{e}^{-jkr}}{4\pi r}\hat{\mathbf{r}}\times\int\left[(\hat{\mathbf{n}}\times\mathbf{E}) - \hat{\mathbf{r}}\times(\hat{\mathbf{n}}\times\mathbf{H})\eta\right]\mathrm{e}^{j\mathbf{k}\cdot\mathbf{r}'}\,\mathrm{d}s, \tag{B9}$$

which is the Stratton-Chu integral.

Appendix C
Explicit Expressions for GO, PO, SPM, IEM, and AIEM Models

C.1 Common Expressions

Some expressions occur in more than one models and are thus presented here.

First, the Kirchhoff fields used in GO, IEM and AIEM are:

$$\begin{aligned} f_{hh} &= \frac{2R_{\|}}{\cos\theta_i + \cos\theta_s}\left[\sin\theta_i \sin\theta_s - (1+\cos\theta_i\cos\theta_s)\cos\Delta\phi\right], && \text{(C1)} \\ f_{vv} &= -\frac{2R_{\perp}}{\cos\theta_i + \cos\theta_s}\left[\sin\theta_i \sin\theta_s - (1+\cos\theta_i\cos\theta_s)\cos\Delta\phi\right], && \text{(C2)} \\ f_{hv} &= 2R\sin\Delta\phi, && \text{(C3)} \\ f_{vh} &= -2R\sin\Delta\phi, && \text{(C4)} \end{aligned}$$

where

$$\begin{aligned} R_{\perp} &= \frac{\eta_2\cos\theta_i - \eta_1\cos\theta_t}{\eta_2\cos\theta_i + \eta_1\cos\theta_t}, && \text{(C5)} \\ R_{\|} &= \frac{\eta_1\cos\theta_i - \eta_2\cos\theta_t}{\eta_1\cos\theta_i + \eta_2\cos\theta_t}, && \text{(C6)} \\ R &= \frac{1}{2}(R_{\|} - R_{\perp}). && \text{(C7)} \end{aligned}$$

C.2 Geometrical Optics

The single scattering expression for the Geometrical Optics model can be found in Fung [22, chap. 5.5] and it is:

$$\sigma_{pq}^{GO} = \frac{k^2|f_{pq}|^2}{2\sigma^2(k_{sz}-k_{iz})^2\varrho''(0)} \exp\left[-\frac{(k_{sx}-k_{ix})^2+(k_{sy}-k_{iy})^2}{2\sigma^2(k_{sz}+k_{iz})^2\varrho''(0)}\right], \tag{C8}$$

where $\rho''(0)$ is the second derivative of the correlation function in the origin.

C.3 Physical Optics

The single scattering expression for a slightly improved version of the Physical Optics model that includes the first order term and the most important part second order term, as described in de Roo [26] is:

$$\sigma_{pq}^{PO} = I_0\left(a_{00pq} - \left(\frac{a_{limn}}{\sin\theta_i}\cdot\frac{q_{li}}{q_z} + \frac{a_{limn}}{\sin\theta_i}\cdot\frac{q_{li}}{q_z}\right)\right)\cdot\left(a_{00pq} - \left(\frac{a_{limn}}{\sin\theta_i}\cdot\frac{q_{li}}{q_z} + \frac{a_{limn}}{\sin\theta_i}\cdot\frac{q_{li}}{q_z}\right)\right)^{\star} \tag{C9}$$

where

$$I_0 = \begin{cases} \frac{(kL)^2}{4}\mathrm{e}^{-(q_z\sigma)^2}\sum_{i=1}^{\infty}\frac{(q_z\sigma)^{2i}}{i!i}\exp\left[-\frac{(q_tL)^2}{4i}\right] & \text{(Gaussian correlation function)} \\ \frac{(kL)^2}{2}\mathrm{e}^{-(q_z\sigma)^2}\sum_{i=1}^{\infty}\frac{(q_z\sigma)^{2i}}{(i-1)!(i^2+(q_tL)^2)^{3/2}} & \text{(exponential correlation function)} \end{cases}$$

and

$$
\begin{aligned}
a_{00hh} &= -R_{\perp}(\cos\theta_i + \cos\theta_s)\cos\Delta\phi && \text{(C10)}\\
a_{00vv} &= -R_{\|}(\cos\theta_i + \cos\theta_s)\cos\Delta\phi && \text{(C11)}\\
a_{00hv} &= R_{\|}(1+\cos\theta_i\cos\theta_s)\sin\Delta\phi && \text{(C12)}\\
a_{00vh} &= -R_{\perp}(1+\cos\theta_i\cos\theta_s)\sin\Delta\phi && \text{(C13)}
\end{aligned}
$$

$$
\begin{aligned}
a_{10hh} &= (R_{\perp}(\sin\theta_s - \sin\theta_i\cos\Delta\phi) - R'_{\perp}(\cos\theta_i + \cos\theta_s)\cos\Delta\phi)\sin\theta_i && \text{(C14)}\\
a_{10vv} &= (R_{\|}(\sin\theta_s - \sin\theta_i\cos\Delta\phi) - R'_{\|}(\cos\theta_i + \cos\theta_s)\cos\Delta\phi)\sin\theta_i && \text{(C15)}\\
a_{10hv} &= (R_{\|}\sin^2\theta_i\cos\theta_s + R'_{\|}\sin\theta_i(1+\cos\theta_i\cos\theta_s))\sin\Delta\phi && \text{(C16)}\\
a_{10vh} &= -(R_{\perp}\sin^2\theta_i\cos\theta_s + R'_{\perp}\sin\theta_i(1+\cos\theta_i\cos\theta_s))\sin\Delta\phi && \text{(C17)}
\end{aligned}
$$

$$
\begin{aligned}
a_{01hh} &= (R_{\|}(1+\cos\theta_i\cos\theta_s)\sin\Delta\phi + R'_{\perp}\cos\theta_i(\cos\theta_i + \cos\theta_s)\sin\Delta\phi && \text{(C18)}\\
a_{01vv} &= (R_{\perp}(1+\cos\theta_i\cos\theta_s)\sin\Delta\phi + R'_{\|}\cos\theta_i(\cos\theta_i + \cos\theta_s)\sin\Delta\phi && \text{(C19)}\\
a_{01hv} &= -R_{\perp}\cos\theta_i(\sin\theta_i\sin\theta_s - (1+\cos\theta_i\cos\theta_s)\cos\Delta\phi) + R_{\|}(\cos\theta_i + \cos\theta_s)\cos\Delta\phi && \text{(C20)}\\
a_{01vh} &= R_{\|}\cos\theta_i(\sin\theta_i\sin\theta_s - (1+\cos\theta_i\cos\theta_s)\cos\Delta\phi) - R_{\perp}(\cos\theta_i + \cos\theta_s)\cos\Delta\phi && \text{(C21)}\\
& && \text{(C22)}
\end{aligned}
$$

with

$$
\begin{aligned}
R'_{\perp} &= \left[\eta_2\sin\theta_i(1-R_{\perp}) - \eta_1\frac{k_1\cos\theta_i}{k_2\cos\theta_t}\sin\theta_t(1+R_{\perp})\right]\cdot[\eta_2\cos\theta_i + \eta_1\cos\theta_t]^{-1} && \text{(C23)}\\
R'_{\|} &= \left[\eta_1\sin\theta_i(1-R_{\|}) - \eta_2\frac{k_1\cos\theta_i}{k_2\cos\theta_t}\sin\theta_t(1+R_{\|})\right]\cdot[\eta_1\cos\theta_i + \eta_2\cos\theta_t]^{-1} && \text{(C24)}\\
& && \text{(C25)}
\end{aligned}
$$

being the first order terms of the reflection coefficients.

C.4 Small Perturbation Model

The first order Small Perturbation Model used in this work was presented in Ulaby et al. [4] and the same version is used here. The scattering coefficient is:

$$\sigma_{pq}^{SPM} = 8|k^2\sigma\cos\theta_i\cos\theta_s\alpha_{pq}|^2\cdot W(k_{ix} + k\sin\theta_i, k_{iy}), \tag{C26}$$

where

$$
\begin{aligned}
\alpha_{hh} &= \left\{[q_{st}q_{it}\cos\Delta\phi - \mu_r\sin\theta_i\sin\theta_s](\mu_r - 1) - \mu_r^2(\epsilon_r - 1)\cos\Delta\phi\right\}\cdot\\
&\quad\cdot\left[\left(\mu_r\cos\theta_s + \sqrt{\mu_r\epsilon_r - \sin^2\theta_s}\right)(\mu_r\cos\theta_i + q_{it})\right]^{-1} && \text{(C27)}\\
\alpha_{vv} &= \left\{[q_{st}q_{it}\cos\Delta\phi - \epsilon_r\sin\theta_i\sin\theta_s](\epsilon_r - 1) - \epsilon_r^2(\mu_r - 1)\cos\Delta\phi\right\}\cdot\\
&\quad\cdot\left[\left(\epsilon_r\cos\theta_s + \sqrt{\mu_r\epsilon_r - \sin^2\theta_s}\right)(\epsilon_r\cos\theta_i + q_{it})\right]^{-1} && \text{(C28)}\\
\alpha_{hv} &= \sin\Delta\phi[\mu_r(\epsilon_r - 1)q_{it} - \epsilon_r(\mu_r - 1)q_{st}]\cdot[(q_{st} + \mu_r\cos\theta_s)(\epsilon_r\cos\theta_i + q_{it})]^{-1} && \text{(C29)}\\
\alpha_{vh} &= \sin\Delta\phi[\epsilon_r(\mu_r - 1)q_{it} - \mu_r(\epsilon_r - 1)q_{st}]\cdot[(q_{st} + \epsilon_r\cos\theta_s)(\mu_r\cos\theta_i + q_{it})]^{-1} && \text{(C30)}
\end{aligned}
$$

and

$$
\begin{aligned}
q_{st} &= \sqrt{\mu_r\epsilon_r - \sin^2\theta_s}, && \text{(C31)}\\
q_{it} &= \sqrt{\mu_r\epsilon_r - \sin^2\theta_i}. && \text{(C32)}
\end{aligned}
$$

C.5 Integral Equation Model

The version of Integral Equation Model used in this work has been thoroughly described in Fung [22] and in Section 6 and needs no further presentation. The scattering coefficient for single scattering is:

$$\sigma_{pq}^{IEM} = \frac{k^2}{2}\exp\left[-\sigma^2(k_{iz}^2+k_{sz}^2)\right]\sum_{n=1}^{\infty}\left[\sigma^{2n}\left|I_{pq}^n\right|\frac{W^{(n)}(k_{sx}-k_{ix},k_{sy}-k_{iy})}{n!}\right] \tag{C33}$$

where

$$I_{pq}^n = (k_{sz}+k_{iz})^n f_{pq}\exp\left(-\sigma^2 k_{iz}k_{sz}\right) + \frac{(k_{sz})^n\mathcal{F}_{pq}(-k_{ix},-k_{iy}) + (k_{iz})^n\mathcal{F}_{pq}(-k_{sx},-k_{sy})}{2} \tag{C34}$$

where $\mathcal{F}_{pq}(k_x,k_y)$ is a simplified version of the complementary field coefficients shown in the next section. The coefficients above are:

$$\begin{aligned}
\mathcal{F}_{hh}(-k_{ix},-k_{iy}) &= [(1-R_\perp)\cos\theta_i-(1+R_\perp)q_{it}/\mu_r]\,[(1+R_\perp)\cos\Delta\phi+(1-R_\perp)\mu_rC_1]+\\
&\quad -\left[(1-R_\perp)^2-(1-R_\perp)(1+R_\perp)\cos\theta_i/q_{it}\right]C_2, &\text{(C35)}\\
\mathcal{F}_{vv}(-k_{ix},-k_{iy}) &= -\left[(1-R_\parallel)\cos\theta_i-(1+R_\parallel)q_{it}/\epsilon_r\right]\left[(1+R_\parallel)\cos\Delta\phi+(1-R_\parallel)\epsilon_rC_1\right]+\\
&\quad +\left[(1-R_\parallel)^2-(1-R_\parallel)(1+R_\parallel)\cos\theta_i/q_{it}\right]C_2, &\text{(C36)}\\
\mathcal{F}_{hv}(-k_{ix},-k_{iy}) &= [(1-R)\cos\theta_i-(1+R)q_{it}/\epsilon_r]\,[(1+R)/\cos\theta_s+(1-R)\epsilon_r/q_{it}]\sin\Delta\phi+\\
&\quad +\left[(1-R)^2-(1-R)(1+R)\cos\theta_i/q_{it}\right]\sin^2\theta_i\sin\Delta\phi, &\text{(C37)}\\
\mathcal{F}_{vh}(-k_{ix},-k_{iy}) &= [(1+R)\cos\theta_i-(1-R)q_{it}/\mu_r]\,[(1-R)/\cos\theta_s+(1+R)\mu_r/q_{it}]\sin\Delta\phi+\\
&\quad +\left[(1+R)^2-(1+R)(1-R)\cos\theta_i/q_{it}\right]\sin^2\theta_i\sin\Delta\phi, &\text{(C38)}
\end{aligned}$$

$$\begin{aligned}
\mathcal{F}_{hh}(-k_{sx},-k_{sy}) &= [(1-R_\perp)\cos\theta_s-(1+R_\perp)q_{st}/\mu_r]\,[(1+R_\perp)\cos\Delta\phi+(1-R_\perp)\mu_rD_1]+\\
&\quad -\left[(1-R_\perp)^2-(1-R_\perp)(1+R_\perp)\cos\theta_s/q_{st}\right]D_2, &\text{(C39)}\\
\mathcal{F}_{vv}(-k_{sx},-k_{sy}) &= -\left[(1-R_\parallel)\cos\theta_s-(1+R_\parallel)q_{st}/\epsilon_r\right]\left[(1+R_\parallel)\cos\Delta\phi+(1-R_\parallel)\epsilon_rD_1\right]+\\
&\quad +\left[(1-R_\parallel)^2-(1-R_\parallel)(1+R_\parallel)\cos\theta_s/q_{st}\right]D_2, &\text{(C40)}\\
\mathcal{F}_{hv}(-k_{sx},-k_{sy}) &= -[(1+R)\cos\theta_s-(1-R)q_{st}/\mu_r]\,[(1-R)/\cos\theta_i+(1+R)\mu_r/q_{st}]\sin\Delta\phi+\\
&\quad -\left[(1+R)^2-(1+R)(1-R)\cos\theta_s/q_{st}\right]\sin^2\theta_s\sin\Delta\phi, &\text{(C41)}\\
\mathcal{F}_{vh}(-k_{sx},-k_{sy}) &= -[(1-R)\cos\theta_s-(1+R)q_{st}/\epsilon_r]\,[(1+R)/\cos\theta_i+(1-R)\epsilon_r/q_{it}]\sin\Delta\phi+\\
&\quad -\left[(1-R)^2-(1-R)(1+R)\cos\theta_s/q_{st}\right]\sin^2\theta_s\sin\Delta\phi, &\text{(C42)}
\end{aligned}$$

where

$$\begin{aligned}
C_1 &= (\cos\Delta\phi-\sin\theta_i\sin\theta_s)/(q_{it}\cos\theta_s), &\text{(C43)}\\
C_2 &= \sin\theta_i(\sin\theta_s-\sin\theta_i\cos\Delta\phi)/\cos\theta_s, &\text{(C44)}\\
D_2 &= (\cos\Delta\phi-\sin\theta_i\sin\theta_s)/(q_{st}\cos\theta_i), &\text{(C45)}\\
D_2 &= \sin\theta_s(\sin\theta_i-\sin\theta_s\cos\Delta\phi)/\cos\theta_i. &\text{(C46)}
\end{aligned}$$

and q_{it} and q_{st} are the same as defined in Appendix C.4.

C.6 Improved Integral Equation Model

The Improved Integral Equation Model that was used for verification against Wu et al. [14] was provided by Magnus Gustafsson [37] and will not be presented here. It was not used in other studies in this report.

C.7 Advanced Integral Equation Model

For the Advanced Integral Equation Model, the single scattering expression is [12, 13]:

$$\sigma_{pq}^{AIEM} = \frac{k^2}{2}\exp\left[-\sigma^2(k_{iz}^2+k_{sz}^2)\right]\sum_{n=1}^{\infty}\left[\sigma^{2n}\left|I_{pq}^n\right|\frac{W^{(n)}(k_{sx}-k_{ix},k_{sy}-k_{iy})}{n!}\right] \tag{C47}$$

where

$$
\begin{aligned}
I_{pq}^{n} = (k_{sz}+k_{iz})^{n} f_{pq} \exp\left(-\sigma^{2} k_{iz} k_{sz}\right) + \frac{1}{4}\Big\{ & \mathcal{F}_{pq}^{+}(-k_{ix},-k_{iy}) \cdot (k_{sz}-k_{iz})^{n} \exp\left[-\sigma^{2}\left(k_{iz}^{2}-k_{iz}k_{sz}+k_{iz}^{2}\right)\right] + \\
& + \mathcal{F}_{pq}^{-}(-k_{ix},-k_{iy}) \cdot (k_{sz}+k_{iz})^{n} \exp\left[-\sigma^{2}\left(k_{iz}^{2}+k_{iz}k_{sz}+k_{iz}^{2}\right)\right] + \\
& + \mathcal{F}_{pq}^{+}(-k_{sx},-k_{sy}) \cdot (k_{iz}+k_{sz})^{n} \exp\left[-\sigma^{2}\left(k_{sz}^{2}-k_{sz}k_{sz}+k_{iz}^{2}\right)\right] + \\
& + \mathcal{F}_{pq}^{-}(-k_{sx},-k_{sy}) \cdot (k_{iz}-k_{sz})^{n} \exp\left[-\sigma^{2}\left(k_{sz}^{2}+k_{sz}k_{sz}+k_{iz}^{2}\right)\right] + \\
& + \mathcal{G}_{pq}^{+}(-k_{ix},-k_{iy}) \cdot (k_{sz}-q_{iz})^{n} \exp\left[-\sigma^{2}\left(q_{iz}^{2}+q_{iz}k_{sz}+k_{iz}^{2}\right)\right] + \\
& + \mathcal{G}_{pq}^{-}(-k_{ix},-k_{iy}) \cdot (k_{sz}+q_{iz})^{n} \exp\left[-\sigma^{2}\left(q_{iz}^{2}-q_{iz}k_{sz}+k_{iz}^{2}\right)\right] + \\
& + \mathcal{G}_{pq}^{+}(-k_{sx},-k_{sy}) \cdot (k_{iz}+q_{sz})^{n} \exp\left[-\sigma^{2}\left(q_{sz}^{2}+q_{sz}k_{sz}+k_{iz}^{2}\right)\right] + \\
& + \mathcal{G}_{pq}^{-}(-k_{sx},-k_{sy}) \cdot (k_{iz}-q_{sz})^{n} \exp\left[-\sigma^{2}\left(q_{sz}^{2}-q_{sz}k_{sz}+k_{iz}^{2}\right)\right]\Big\}
\end{aligned}
\tag{C48}
$$

with $q_{sz} = \sqrt{k_2^2 - k_{sx}^2 - k_{sy}^2}$ and $q_{iz} = \sqrt{k_2^2 - k_{ix}^2 - k_{iy}^2}$. The function $W^{(n)}(k_x, k_y)$ is the Fourier transform of the nth power of the correlation function.

The explicit expressions for $\mathcal{F}$ and $\mathcal{G}$ are here presented. Using $q_{\alpha m} = \sqrt{k_m^2 - k_{\alpha x}^2 - k_{\alpha y}^2}$ ($m = 1, 2$ depending on medium, and $\alpha = i, s$ for incident/scattered radiation), the upward and downward reradiation coefficients found in (C48) are:

$$
\mathcal{F}_{pq}^{+}(k_x, k_y) = \mathcal{F}_{pq}(k_x, k_y, q_1, q_1), \tag{C49}
$$
$$
\mathcal{F}_{pq}^{-}(k_x, k_y) = \mathcal{F}_{pq}(k_x, k_y, -q_1, q_1) \tag{C50}
$$

for medium 1 and

$$
\mathcal{G}_{pq}^{+}(k_x, k_y) = \mathcal{G}_{pq}(k_x, k_y, q_2, q_2), \tag{C51}
$$
$$
\mathcal{G}_{pq}^{-}(k_x, k_y) = \mathcal{G}_{pq}(k_x, k_y, -q_2, q_2) \tag{C52}
$$

for medium 2.

The functions $\mathcal{F}_{pq}(k_x, k_y, k_z, q)$ and $\mathcal{G}_{pq}(k_x, k_y, k_z, q)$ specified in (C54)-(C60) are used to determine the coefficients (C49)-(C52). Note, that parameters k_x, k_y, and k_z are actually only used in C and B coefficients found in (C65)-(C76). q is a parameter with the same magnitude as k_z but its sign remains fixed upon the change of reradiation direction. It is only used in expressions (C54)-(C60):

$$
\begin{aligned}
\mathcal{F}_{hh}(k_x, k_y, k_z, q) &= \frac{1-R_h}{q}\left[(1+R_h)C_1 - (1-R_h)C_2 - (1+R_h)C_3\right] + \\
&\quad - \frac{1+R_h}{q}\left[(1-R_h)C_4 + (1+R_h)C_5 + (1-R_h)C_6\right], && \text{(C53)} \\
\mathcal{F}_{vv}(k_x, k_y, k_z, q) &= -\frac{1-R_v}{q}\left[(1+R_v)C_1 - (1-R_v)C_2 - (1+R_v)C_3\right] + \\
&\quad + \frac{1+R_v}{q}\left[(1-R_v)C_4 + (1+R_v)C_5 + (1-R_v)C_6\right], && \text{(C54)} \\
\mathcal{F}_{hv}(k_x, k_y, k_z, q) &= \frac{1-R}{q}\left[(1+R)B_1 - (1-R)B_2 - (1+R)B_3\right] + \\
&\quad + \frac{1+R}{q}\left[(1-R)B_4 + (1+R_h)B_5 + (1-R_h)B_6\right], && \text{(C55)} \\
\mathcal{F}_{vh}(k_x, k_y, k_z, q) &= \frac{1+R}{q}\left[(1+R)B_4 + (1-R)B_5 + (1+R)B_6\right] + \\
&\quad + \frac{1-R}{q}\left[(1-R)B_1 - (1+R_h)B_2 - (1-R_h)B_3\right], && \text{(C56)}
\end{aligned}
$$

$$\mathcal{G}_{hh}(k_x,k_y,k_z,q) = -\frac{1+R_h}{q}[(1+R_h)C_1\varepsilon_r-(1-R_h)C_2-(1+R_h)C_3]+ \frac{1-R_h}{q}[(1-R_h)C_4+(1+R_h)C_5+(1-R_h)C_6/\varepsilon_r], \tag{C57}$$

$$\mathcal{G}_{vv}(k_x,k_y,k_z,q) = \frac{1+R_v}{q}[(1+R_v)C_1-(1-R_v)C_2-(1+R_v)C_3/\varepsilon_r]+ -\frac{1-R_v}{q}[(1-R_v)C_4\varepsilon_r+(1+R_v)C_5+(1-R_v)C_6], \tag{C58}$$

$$\mathcal{G}_{hv}(k_x,k_y,k_z,q) = -\frac{1+R}{q}[(1+R)B_1-(1-R)B_2-(1+R)B_3/\varepsilon_r]+ -\frac{1-R}{q}[(1-R)B_4\varepsilon_r+(1+R)B_5+(1-R)B_6], \tag{C59}$$

$$\mathcal{G}_{vh}(k_x,k_y,k_z,q) = -\frac{1+R}{q}[(1+R)B_4+(1-R)B_5+(1+R)B_6/\varepsilon_r]+ -\frac{1-R}{q}[(1-R)B_1\varepsilon_r-(1+R)B_2-(1-R)B_3]. \tag{C60}$$

Without making any approximations, the angle ϕ_i can be set to 0. Using the slopes

$$z_x = -\frac{k_{sx}+k_x}{k_{iz}-k_z}, \tag{C61}$$

$$z_y = -\frac{k_{sy}+k_y}{k_{iz}-k_z}, \tag{C62}$$

$$z'_x = \frac{k_{ix}+k_x}{k_{iz}+k_z}, \tag{C63}$$

$$z'_y = \frac{k_{ix}+k_y}{k_{iz}+k_z}, \tag{C64}$$

the C coefficients for the co-polarized $\mathcal{F}$ coefficients are as follows:

$$C_1 = C_1(k_x,k_y,k_z) = \cos\phi_s(1+z_xz'_x)+\sin\phi_s z_yz'_x, \tag{C65}$$

$$C_2 = C_2(k_x,k_y,k_z) = \cos\phi_s(k_x\cos\theta_i+k_xz_x\cos\theta_i+k_zz'_x\sin\theta_i+k_xz_xz'_x\sin\theta_i+k_yz'_y\cos\theta_i-k_yz_xz'_y\sin\theta_i)+ +\sin\phi_s(k_xz_y\cos\theta_i+k_xz_yz'_x\sin\theta_i+k_zz'_y\sin\theta_i-k_xz'_y\cos\theta_i+k_yz_yz'_y\sin\theta_i), \tag{C66}$$

$$C_3 = C_3(k_x,k_y,k_z) = -\cos\phi_s(k_x\sin\theta_i-k_zz_x\sin\theta_i-k_xz'_x\cos\theta_i+k_zz_xz'_x\cos\theta_i)+ -\sin\phi_s(k_y\sin\theta_i-k_yz'_x\cos\theta_i-k_zz_y\sin\theta_i+k_zz_yz'_x\cos\theta_i), \tag{C67}$$

$$C_4 = C_4(k_x,k_y,k_z) = \cos\theta_s\sin\phi_s(z'_y\sin\theta_i-z_xz'_y\cos\theta_i)+ +\cos\theta_s\cos\phi_s(\cos\theta_i+z'_x\sin\theta_i+z_yz'_y\cos\theta_i)+ -\sin\theta_s(z_x\cos\theta_i+z_xz'_x\sin\theta_i-z_yz'_y\sin\theta_i), \tag{C68}$$

$$C_5 = C_5(k_x,k_y,k_z) = \cos\theta_s\sin\phi_s(k_yz_x-k_yz'_x)+ -\cos\theta_s\cos\phi_s(k_z+k_xz_x+k_yz_y)+ +\sin\theta_s(k_zz_x+k_xz_xz'_x+k_yz_yz'_x), \tag{C69}$$

$$C_6 = C_6(k_x,k_y,k_z) = \cos\theta_s\sin\phi_s(k_xz'_x-k_zz_xz'_y)+ -\cos\theta_s\cos\phi_s(k_yz'_y-k_zz_yz'_y)+ +\sin\theta_s(k_yz_xz'_y-k_xz_yz'_y), \tag{C70}$$

while the corresponding B coefficients for the cross-polarized field coefficients are:

$$B_1 = B_1(k_x, k_y, k_z) = \cos\theta_s \sin\phi_s(1 + z_x z_x') - z_y \sin\theta_s - z_y z_x' \cos\theta_s \cos\phi_s, \tag{C71}$$

$$\begin{aligned} B_2 = B_2(k_x, k_y, k_z) = {} & \cos\theta_s \sin\phi_s(k_z \cos\theta_i + k_x z_x \cos\theta_i + k_z z_x' \sin\theta_i + k_x z_x z_x' \sin\theta_i + k_y z_y' \cos\theta_i + k_y z_x z_y' \sin\theta_i) + \\ & - \sin\theta_s(k_z z_y \cos\theta_i + k_z z_y z_x' \sin\theta_i - k_z z_x z_y' \sin\theta_i - k_x z_x z_y' \cos\theta_i + k_y z_y z_y' \cos\theta_i) + \\ & - \cos\phi_s \cos\theta_s(k_x z_y \cos\theta_i + k_x z_y z_x' \sin\theta_i + k_z z_y' \sin\theta_i - k_x z_y' \cos\theta_i + k_y z_y z_y' \sin\theta_i), \end{aligned} \tag{C72}$$

$$\begin{aligned} B_3 = B_3(k_x, k_y, k_z) = {} & - \cos\theta_s \sin\phi_s(k_x \sin\theta_i - k_z z_x \sin\theta_i - k_x z_x' \cos\theta_i + k_z z_x z_x' \cos\theta_i) + \\ & + \cos\phi_s \cos\theta_s(k_y \sin\theta_i - k_y z_x' \cos\theta_i - k_z z_y \sin\theta_i + k_z z_y z_x' \cos\theta_i) + \\ & - \sin\theta_s(k_y z_x \sin\theta_i - k_x z_x z_x p \cos\theta_i - k_x z_y \sin\theta_i + k_x z_y z_x' \cos\theta_i), \end{aligned} \tag{C73}$$

$$\begin{aligned} B_4 = B_4(k_x, k_y, k_z) = {} & \cos\phi_s(z_y' \sin\theta_i - z_x z_y' \cos\theta_i) + \\ & - \sin\phi_s(\cos\theta_i + z_x' \sin\theta_i + z_y z_y' \cos\theta_i), \end{aligned} \tag{C74}$$

$$\begin{aligned} B_5 = B_5(k_x, k_y, k_z) = {} & \cos\phi_s(k_y z_x - k_y z_x') + \\ & + \sin\phi_s(k_z + k_x z_x' + k_y z_y), \end{aligned} \tag{C75}$$

$$\begin{aligned} B_6 = B_6(k_x, k_y, k_z) = {} & \cos\phi_s(k_x z_y' - k_z z_x z_y') + \\ & + \sin\phi_s(k_y z_y' - q z_y z_y'). \end{aligned} \tag{C76}$$

APPENDIX D
ADDITIONAL FUNCTIONS

D.1 Transition Function

The transition function [13, 20, 34] is a function that interpolates values for $R_\parallel$ and $R_\perp$ and replaces the choice between incident/specular angle for Fresnel coefficient calculation that is described in Section 6.3. Transition function has been used together with AIEM model in some cases but will not be described more thoroughly here. Only the explicit expression for that function will be presented while a description can be found in Wu et al. [20].

The Fresnel coefficient for a polarization p that is either vertical ($_\parallel$) or horizontal ($_\perp$) is:

$$R_p(T) = R_p(\theta_{incident}) + [R_p(\theta_{specular}) - R_p(\theta_{incident})] \left(1 - \frac{S_p}{S_p^0}\right) \tag{D1}$$

where

$$S_p = \frac{1}{4} \cdot \frac{\sum_{n=1}^{\infty} \left[\frac{(k\sigma\cos\theta_i)^{2n}}{n!} \left| \widetilde{F}_p \right|^2 W^{(n)}(k_{sx} - k_{ix}, k_{sy} - k_{iy}) \right]}{\sum_{n=1}^{\infty} \left[\frac{(k\sigma\cos\theta_i)^{2n}}{n!} \left| 2^{n+1} \frac{R_p(0)}{\cos\theta_i} \mathrm{e}^{-(k\sigma\cos\theta_i)^2} + \frac{\widetilde{F}_p}{2} \right|^2 W^{(n)}(k_{sx} - k_{ix}, k_{sy} - k_{iy}) \right]}, \tag{D2}$$

$$S_p^0 = \frac{\alpha_1}{\alpha_1 + \alpha_2 + \alpha_3}, \tag{D3}$$

and

$$\alpha_1 = \frac{1}{4}\left[\cos\theta_s \mathcal{F}_{pq}(-k_{ix}, -k_{iy}) + \cos\theta_i \mathcal{F}_{pq}(-k_{sx}, -k_{sy})\right], \tag{D4}$$

$$\alpha_2 = (\cos\theta_s + \cos\theta_i)\mathrm{Re}\left\{f_{pq} * \left[\cos\theta_s \mathcal{F}_{pq}(-k_{ix}, -k_{iy}) + \cos\theta_i \mathcal{F}_{pq}(-k_{sx}, -k_{sy})\right]\right\}, \tag{D5}$$

$$\alpha_3 = (\cos\theta_s + \cos\theta_i)|f_{pq}|^2. \tag{D6}$$

The two $\widetilde{F}_p$ are:

$$\widetilde{F}_h = 8R_v(0)\sin^2\theta_i \left(\frac{\cos\theta_i + \sqrt{\epsilon_r - \sin^2\theta_i}}{\cos\theta_i \sqrt{\epsilon_r - \sin^2\theta_i}} \right), \tag{D7}$$

$$\widetilde{F}_v = -8R_h(0)\sin^2\theta_i \left(\frac{\cos\theta_i + \sqrt{\epsilon_r - \sin^2\theta_i}}{\cos\theta_i \sqrt{\epsilon_r - \sin^2\theta_i}} \right). \tag{D8}$$

D.2 Shadowing Function

One fact that usually has to be included in the computation of the scattering coefficients is the shadowing function. This function lowers the radar cross section of a resolution cell due to shadowing at high incident angles θ_i (low grazing angles). Shadowing has been studied by Smith [36] and Sancer [35] among others and is also described in Ulaby et al. [4] and Fung [22]. The function is simply multiplied with the scattering coefficient:

$$\sigma^0_{SH} = \sigma^0 \cdot S_{in} \cdot S_{out}, \tag{D9}$$

where σ^0 is the scattering coefficient without shadowing, S_{in} is the shadowing factor for incident radiation, and S_{out} is the shadowing factor for the scattered radiation.

Smith [36] describes two possible functions:

$$\begin{aligned} S_1(\theta_i, \sigma_s) &= [1 + f(\theta_i, \sigma_s)]^{-1}, && \text{(D10)} \\ S_2(\theta_i, \sigma_s) &= \left[1 - \frac{1}{2}\text{erfc}\left(\frac{\cot\theta_i}{\sigma_s\sqrt{2}}\right)\right] S_1(\theta_i, \sigma_s), && \text{(D11)} \\ & && \text{(D12)} \end{aligned}$$

where the first one represents the probability of "clear view" and the second one is more suitable for Kirchhoff terms and it is "the conditional probability that a point will not lie in the shadow given that its local slope is perpendicular to the incident beam", citing Fung [22, p. 191]. The function

$$f(\theta_i, \sigma_s) = \frac{1}{2}\left[\sqrt{\frac{2}{\pi}} \cdot \frac{\sigma_s}{\cot\theta_i}\exp\left(-\frac{\cot\theta_i^2}{2\sigma_s^2}\right) - \text{erfc}\left(\frac{\cot\theta_i}{\sigma_s\sqrt{2}}\right)\right], \tag{D13}$$

where σ_s is the root-mean-square slope, contains the so-called complementary error function:

$$\text{erfc}(x) = 1 - \text{erf}(x) = 1 - \frac{2}{\sqrt{\pi}}\int_0^x \mathrm{e}^{-t^2}\,\mathrm{d}t. \tag{D14}$$

REFERENCES

[1] P. Beckmann and A. Spizzichino. *The Scattering of Electromagnetic Waves from Rough Surfaces*. Artech House, 1987.

[2] J. A. Ogilvy. *Theory of Wave Scattering from Random Rough Surfaces*. Adam Hilger, 1991.

[3] L. Tsang, J. A. Kong, and R. T. Shin. *Theory of Microwave Remote Sensing*. John Wiley & Sons, 1985.

[4] F. T. Ulaby, R. K. Moore, and A. K. Fung. *Microwave Remote Sensing, Active and Passive, Volume II: Radar Remote Sensing and Surface Scattering and Emission Theory*, volume II. Addison-Wesley, 1982.

[5] F. T. Ulaby, R. K. Moore, and A. K. Fung. *Microwave Remote Sensing, Active and Passive, Volume III: From Theory to Applications*, volume III. Addison-Wesley, 1988.

[6] F. T. Ulaby, C. Elachi, Y. Kuga, K. C. McDonald, K. Sarabandi, T. B. A. Senior, J. J. van Zyl, M. W. Whitt, and H. A. Zebker. *Radar Polarimetry for Geoscience Applications*. Artech House, 1990.

[7] A. G. Voronovich. *Wave Scattering from Rough Surfaces*. Springer Series on Wave Phenomena. Springer, 2nd edition, 1999.

[8] A. K. Fung and G. W. Pan. A Scattering Model for Perfectly Conducting Random Surfaces. I – Model Development. II – Range of Validity. *International Journal of Remote Sensing*, 8:1579–1605, November 1987.

[9] A. K. Fung, Z. Li, and K.-S. Chen. Backscattering from a Randomly Rough Dielectric Surface. *IEEE Transactions on Geoscience and Remote Sensing*, 30(2):356–369, March 1992.

[10] A. J. Poggio and E. K. Miller. *Computer Techniques for Electromagnetics*, volume 7, chapter 4. Integral Equation Solutions of Three-Dimensional Scattering Problems, pages 159–261. Pergamon Press, 1973.

[11] A. K. Fung, W. Y. Liu, K.-S. Chen, and M.-K. Tsay. An Improved IEM Model for Bistatic Scattering from Rough Surfaces. *Journal of Electromagnetic Waves and Applications*, 16(5):689–702, 2002.

[12] K.-S. Chen, T.-D. Wu, L. Tsang, Q. Li, J. Shi, and A. K. Fung. Emission of Rough Surfaces Calculated by the Integral Equation Method with Comparison to Three-Dimensional Moment Method Simulations. *IEEE Transactions on Geoscience and Remote Sensing*, 41(1):90–100, January 2003.

[13] T.-D. Wu and K.-S. Chen. A Reappraisal of the Validity of the IEM Model for Backscattering from Rough Surfaces. *IEEE Transactions on Geoscience and Remote Sensing*, 42(4):742–753, April 2004.

[14] T.-D. Wu, K.-S. Chen, J. Shi, H.-W. Lee, and A. K. Fung. A Study of an AIEM Model for Bistatic Scattering from Randomly Rough Surfaces. *IEEE Transactions on Geoscience and Remote Sensing*, 46(9):2584–2598, September 2008.

[15] S. Kingsley and S. Quegan. *Understanding Radar Systems*. McGraw-Hill, 1992.

[16] R. J. Sullivan. *Radar Foundations for Imaging and Advanced Concepts*. Scitech Publishing, 2004.

[17] I. H. Woodhouse. *Introduction to Microwave Remote Sensing*. Taylor & Francis, 2006.

[18] M. I. Skolnik, editor. *Radar Handbook*. McGraw-Hill, 2nd edition, 1990.

[19] AIAA. Radar Frequency Bands. American Institute of Aeronautics and Astronautics homepage: http://www.aewa.org/Library/rf_bands.html, 1995. [Online; accessed 27-July-2009].

[20] T.-D. Wu, K.-S. Chen, J. Shi, and A. K. Fung. A Transition Model for the Reflection Coefficient in Surface Scattering. *IEEE Transactions on Geoscience and Remote Sensing*, 39(9):2040–2050, September 2001.

[21] A. Ishimaru. *Wave Propagation and Scattering in Random Media*. IEEE Press, 1997.

[22] A. K. Fung. *Microwave Scattering and Emission Models and Their Applications*. Artech House, 1994.

[23] E. I. Thorsos. The Validity of the Kirchhoff Approximation for Rough Surface Scattering Using a Gaussian Roughness Spectrum. *The Journal of the Acoustical Society of America*, 83(1):78–92, January 1988.

[24] F. Koudogbo, P. F. Combes, and H. J. Mametsa. Numerical and Experimental Validations of IEM for Bistatic Scattering from Natural and Manmade Rough Surfaces. *Progress in Electromagnetics Research*, 46:203–244, 2004.

[25] W. G. Rees. *Physical Principles of Remote Sensing*. Cambridge University Press, 2nd edition, 2001.

[26] R. D. de Roo. *Theory and Measurement of Bistatic Scattering of X-band Microwaves from Rough Dielectric Surfaces*.

PhD thesis, University of Michigan, 1996.

[27] R. D. de Roo and F. T. Ulaby. Bistatic Specular Scattering from Rough Dielectric Surfaces. *IEEE Transactions on Antennas and Propagation*, 42(2):220–231, February 1994.

[28] J. D. Kraus and K. R. Carver. *Electromagnetics*. McGraw-Hill, 2nd edition, 1973.

[29] K.-S. Chen and A. K. Fung. A Comparison of Backscattering Models for Rough Surfaces. *IEEE Transactions on Geoscience and Remote Sensing*, 33(1):195–200, January 1995.

[30] K.-S. Chen, T.-D. Wu, M.-K. Tsay, and A. K. Fung. A Note on the Multiple Scattering in an IEM Model. *IEEE Transactions on Geoscience and Remote Sensing*, 38(1):249–256, January 2000.

[31] C.-Y. Hsieh and A. K. Fung. Application of an Extended IEM to Multiple Surface Scattering and Backscatter Enhancement. *Journal of Electromagnetic Waves and Applications*, 13(1):121–135, 1999.

[32] C.-Y. Hsieh, A. K. Fung, G. Nesti, A. J. Sieber, and P. Coppo. A Futher Study of the IEM Surface Model. *IEEE Transactions on Geoscience and Remote Sensing*, 35(4):901–909, July 1997.

[33] J. L. Álvarez-Pérez. An Extension of the IEM/IEMM Surface Scattering Model. *Waves in Random Media*, 11(3): 307–329, March 2001.

[34] A. K. Fung and K.-S. Chen. An Update on the IEM Surface Backscattering Model. *IEEE Geoscience and Remote Sensing Letters*, 1(2):75–77, April 2004.

[35] M. I. Sancer. Shadow-Corrected Electromagnetic Scattering from a Randomly Rough Surface. *IEEE Transactions on Antennas and Propagation*, AP-17(5):577–585, September 1969.

[36] B. G. Smith. Geometrical Shadowing of a Random Rough Surface. *IEEE Transactions on Antennas and Propagation*, AP-15(5):668–671, September 1967.

[37] M. Gustafsson. Matlab® code for IIEM. FOI (Totalförsvarets Forskningsinstitut), December 2004.

[38] T.-D. Wu. Fortran code for AIEM. National Central University, Taiwan, August 2005.

[39] Y. Oh, K. Sarabandi, and F. T. Ulaby. An Empirical Model and an Inversion Technique for Radar Scattering from Bare Soil Surfaces. *IEEE Transactions on Geoscience and Remote Sensing*, pages 370–381, March 1992.

[40] G. Macelloni, G. Nesti, P. Pampaloni, S. Sigismondi, D. Tarchi, and S. Lolli. Experimental Validation of Surface Scattering and Emission Models. *IEEE Transactions on Geoscience and Remote Sensing*, 38(1):459–469, January 2000.

[41] Q. Li, J. Shi, and K.-S. Chen. A Generalized Power Law Spectrum and its Applications to the Backscattering of Soil Surfaces Based on the Integral Equation Model. *IEEE Transactions on Geoscience and Remote Sensing*, 40 (2):271–280, February 2002.

[42] A. G. Voronovich. Small Slope Approximation for Electromagnetic Waves Scattering at a rRough Interface of Two Dielectric Half-spaces. *Waves in Random Media*, 4(3):337–367, July 1994.

[43] D. K. Cheng. *Fundamentals of Engineering Electromagnetics*. Addison-Wesley, 1993.

[44] J. A. Stratton. *Electromagnetic Thory*. McGraw-Hill, 1941.